COAGULATION IN CONTINUOUS PARTICLE SIZE DISTRIBUTIONS; THEORY AND EXPERIMENTAL VERIFICATION

by

James Robert Hunt

W. M. Keck Laboratory of Environmental Engineering Science
Division of Engineering and Applied Science
CALIFORNIA INSTITUTE OF TECHNOLOGY
Pasadena, California 91125

Report No. AC-5-80 May 1980

COAGULATION IN CONTINUOUS PARTICLE SIZE DISTRIBUTIONS; THEORY AND EXPERIMENTAL VERIFICATION

by

James Robert Hunt

Thesis Advisor:

James J. Morgan
Professor of
Environmental Engineering Science

Supported by Grants from

U. S. Public Health Service
U. S. Environmental Protection Agency
Union Oil Company
Jessie Smith Noyes Foundation, Inc.
NOAA Office of Sea Grant

Keck Laboratories of Environmental Engineering Science
Division of Engineering and Applied Science
California Institute of Technology
Pasadena, California 91125

Report No. AC-5-80 May 1980

ACKNOWLEDGMENTS

I wish to thank my advisor, James Morgan, for his support and patience during my graduate studies. He sets an excellent example of a researcher and a teacher.

The following professors kindly served on my examination committees: R. C. Flagan, S. K. Friedlander, G. R. Gavalas, E. J. List, and P. G. Saffman.

Discussions with Michael Barcelona, Howard Liljestrand, and James Young provided considerable help in the laboratory.

Caltech is fortunate in having such a helpful and dedicated staff. The Environmental Engineering Librarian, Rayma Harrison, and her assistant, Gunilla Hastrup, were always cheerful, even with late afternoon questions. The secretarial staff, Elaine Granger, Joan Mathews, Bonnie Kimble, and Adelaide Massengale, provided considerable support in getting things accomplished. Joan Mathews skillfully typed the thesis and always maintained the highest quality. Technical help was freely supplied by Dave Byrum, Elton Daly, Richard Eastvedt, and Joe Fontana.

Furthermore, I must thank Dana Hunt for her occasional naps which allowed a substantial amount of the writing and editing of this thesis. When Dana's naps became shorter and more time was needed on campus, Marjorie Hunt, my mother, kindly helped out. My spouse, Kristine Hunt, provided financial, editorial, and moral support as needed.

The following organizations were generous in their support to Caltech and this research: U. S. Public Health Service,

U. S. Environmental Protection Agency, Union Oil Company, Jessie Smith Noyes Foundation, Inc., and NOAA Office of Sea Grant.

ABSTRACT

Previous theories for particle coagulation are not readily applicable to the continuous particle size distributions encountered in natural waters. By extending concepts developed in the analysis of aerosol dynamics, predictions of continuous particle size distributions were obtained dimensionally for size intervals dominated by Brownian, shear, differential sedimentation coagulation and gravitational settling. A dynamic steady state size distribution was assumed to exist, maintained by a constant flux of particle volume through the distribution. Predictions have been successfully compared with the shapes of particle size distributions measured in oceanic waters.

An experimental program was designed to test the predictions with cleaned clay and silica minerals in artificial seawater. A series of batch experiments was conducted at fluid shear rates of 1/2 to 32 sec^{-1} in a rotating cylinder apparatus. During the experiments, total suspended volumes were determined from suspension optical absorbance, and particle size distributions were measured with a Coulter Counter-multichannel analyzer system. The volume flux through the distribution was estimated from the rate of suspended particle volume removal, which was second order in suspended volume and depended on the fluid shear rate.

The Brownian and shear coagulation predictions were verified for the kaolinite, illite, and montmorillonite clays. The three clays were significantly different in the regions of Brownian and shear coagulation dominance and in the volume removal rates at low fluid shear rates. At higher shear rates the volume removal rates declined

because of aggregate breakup by fluid shear in the rotating cylinder apparatus. Differences in the clay coagulation and breakup characteristics were explained by variations in clay aggregate porosities. Experiments with silica did not agree with predictions because the silica particles were not destabilized in seawater. Predictions for differential sedimentation coagulation and gravitational settling could not be tested because of larger aggregate breakup by the Coulter Counter.

The theoretical predictions have direct application to particle coagulation in oceanic waters and possible application to more complex systems, such as estuarine waters and water and wastewater treatment operations.

TABLE OF CONTENTS

TABLE OF CONTENTS (Continued)

LIST OF FIGURES

LIST OF FIGURES (Continued)

LIST OF FIGURES (Continued)

LIST OF FIGURES (Continued)

LIST OF TABLES

NOTATIONS

A_b	Dimensionless constant for Brownian coagulation.
A_{ds}	Dimensionless constant for differential sedimentation coagulation.
A_s	Dimensionless constant for gravitational settling.
A_{sh}	Dimensionless constant for shear coagulation.
b	Second order volume removal rate constant (ppm^{-1}/sec) and log base of sizing system in Appendix B.
d_p	Particle diameter [ℓ].
E	Particle volume flux through the size distribution [$\ell^3 L^{-3} t^{-1}$].
g	Gravitational acceleration.
G	Shear rate [$L^3 \ell^{-3} t^{-1}$].
G'(r)	Shear rate at radial distance r in rotating cylinder apparatus.
k	Boltzmann constant.
K_b	Brownian coagulation parameter, $K_b = kT/\mu$ [$L^3 t^{-1}$].
K_{ds}	Differential sedimentation coagulation parameter, $K_{ds} = g(\rho_p - \rho_f)/\nu\rho_f$ [$L^3 \ell^{-4} t^{-1}$].
[ℓ]	Particle length unit.
[L]	Fluid length unit.
$n(d_p)$	Particle size distribution, distributed on particle diameter [$L^{-3} \ell^{-1}$].
n(v)	Particle size distribution, distributed on particle volume [$L^{-3} \ell^{-3}$].
n_i	Discrete particle size distribution, number of particles of volume v_i.
N	Total number of particles in Chapter 2 (#/mL) and outer cylinder rotation rate in Chapter 3 and Appendix C (rev./min.).

NOTATIONS (Continued)

N_o	Number of particles at t = 0 (#/mL).
R	Resistance across orifice (Ω).
R_1	Inner cylinder radius.
R_2	Outer cylinder radius.
S	Gravitational settling parameter $[L\ell^{-2}t^{-1}]$.
[t]	Time unit.
T	Absolute temperature.
v	Particle volume $[\ell^3]$.
V	Total suspended volume $[\ell^3 L^{-3}]$.
V	voltage.
$\frac{dV}{d(\log d_p)}$	Volume distribution, $\frac{dV}{d(\log d_p)} = \frac{2.3\pi}{6} d_p^4 n(d_p)$.
$\frac{d\bar{V}}{d(\log \delta)}$	Normalized volume distribution, $\frac{d\bar{V}}{d(\log \delta)} = \frac{dV}{d(\log d_p)} \left(\frac{G}{E}\right)^{1/2}$.
α, α'	Dimensionless parameters representing particle and fluid properties defined in Equations (D.8) and (D.13).
β_b	Collision function for Brownian coagulation $[L^3t^{-1}]$.
β_{ds}	Collision function for differential sedimentation coagulation $[L^3t^{-1}]$.
β_{sh}	Collision function for shear coagulation $[L^3t^{-1}]$.
δ	Normalized particle diameter, $\delta = d_p(G/K_b)^{1/3}$.
ε	Rate of turbulent energy dissipation.
η	Coagulation collision efficiency for monodisperse particles.
μ	Dynamic viscosity.
ν	Kinematic viscosity.
ρ_f	Fluid density.
ρ_p	Particle density.

CHAPTER 1

MODELING THE FATE OF PARTICLES DISCHARGED INTO OCEANIC WATERS

Pollution from suspended particles is one of many consequences of the intensive utilization of the land and the coastal zone. Sources of added pollutant particles include: 1) residual disposal from urban areas, such as treated sewage, sewage sludge, and land surface washoff, 2) dredge spoil disposal from shipping canals and harbors, and more recently, 3) deep ocean mining of metals from the sea floor which could substantially increase the amount of particles suspended in the deep oceanic waters. The particles, themselves, are pollutants in that suspended matter decreases light penetration (Peterson, 1974), which is esthetically displeasing and can decrease the rate of photosynthesis. The degradable organic matter in sewage particles can deplete bottom waters of dissolved oxygen if sedimentation rates are too high. Particles are also of concern because toxic metals and persistent organic compounds are predominately transported within the particle or adsorbed at the surface (see, for example Turekian, 1977; Pavlou and Dexter, 1979). Thus, the fate of particles and associated chemical pollutants must be known to plan for residual disposal in oceanic waters.

This chapter reviews some studies of the fate of particles in oceanic waters and presents a justification for further work on particle coagulation in seawater. The following chapters review particle sedimentation and coagulation mechanisms, develop predictions

of coagulating and settling particle size distributions, and experimentally test the validity of these predictions.

1.1 Previous Approaches

There have been a number of studies examining the fate of suspended particles in rivers and sewage effluents discharged into coastal waters. Some of these studies are reviewed to outline the methods of analysis and to indicate problems that prevent a complete understanding. The three categories considered are particle settling models, bottom sediment models, and coagulation models. The main concern in the study of particle fate in oceanic waters has been the rate of particle accumulation in the bottom sediments. Rapid accumulation concentrates organic matter and toxic chemicals which are harmful to the natural biological community.

Geographically, the southern California coastal waters have received the most intense quantitative studies on the fate of sewage particles. Southern California is a highly urbanized and arid region having a sewage collection system separate from the flood control system. The sewage collection system is regionalized, and partially treated wastewaters are discharged into the ocean at four major outfalls, typically releasing the effluent at a water depth of 60 meters through long diffusers. The Southern California Coastal Water Research Project (1978) has compiled information on the wastewater discharges and pollutant loadings. For these reasons discharged wastewaters are the principal sources of metals, organics, and particulate matter to the coastal waters of southern California, and thus an area suited for a

quantitative analysis of pollutant transport.

There are many other areas situated on estuaries and coastal zones which use the local waters for waste disposal. These areas are more complex because of tidal flows, many point sources of wastes, contributions of suspended matter from rivers, and wastes resulting from dredging and barge disposal operations. A major example is the New York Bight, which is undergoing extensive study (Gross, 1976). The New York Bight receives wastes from the rivers draining into it, from sewage effluents of the New York metropolitan area where treatment varies from none to secondary, and from construction, chemical, and sewage sludge wastes barged to various sites for disposal. The area has a wide continental shelf with poorly known circulation patterns and there exists a complex coupling of the wind generated turbulence and the resuspension and movement of bottom sediments. While waste disposal in southern California is difficult to analyze, the complexity is greater in other areas where the various waste sources and transport processes are difficult to quantify.

1.1.1 Particle Settling Models

From knowledge of an effluent particle settling velocity distribution and ocean currents near the discharge area, sediment accumulation rates can be predicted. Particle settling velocity distributions are measured in quiescent settling columns using solutions comparable to seawater in terms of ionic composition and temperature. Then, based on an assumed current pattern, turbulent diffusivity, and initial waste field configuration, particle

trajectories are calculated, giving sediment accumulation rates.

In the design of the Hyperion sludge outfall for the City of Los Angeles, Brooks (1956) estimated bottom sedimentation rates for the digested sludge particles based on laboratory measurements of sewage sludge settling in seawater. Brooks assumed the currents to be constant in magnitude with equal frequencies in all directions.

Recent studies of particle settling from sewage plumes were begun following the field sampling efforts of Galloway (1972) which revealed substantial trace metal accumulation in the sediments down-current from the Los Angeles County Sanitation Districts' White's Point outfall. Hendricks and Young (1974) used Brooks' settling velocity data for Hyperion sludge and water currents measured in the White's Point area to predict sediment and metal accumulation rates. A steady state model for metal mobilization from the sediments was assumed and model parameters were obtained by fitting the model to the data.

Morel *et al.* (1975) have discussed particulate transport of metals to the sediments near the White's Point outfall. The authors mentioned the importance of particle coagulation in determining the deposition of particles and associated metals. Faisst (1976) demonstrated the importance of particle interactions in the laboratory measurement of sludge settling velocity distributions. With three different dilutions of anaerobically digested sewage sludge with seawater, Faisst observed greater settling velocities at larger sludge concentrations. Observations were qualitatively explained by the greater opportunity for

particle coagulation at the higher sludge concentrations. The settling velocity distributions were used by Faisst to evaluate the impact of sewage sludge disposal into the submarine basins off southern California.

1.1.2 Sediment Analysis Models

An alternative approach to understanding the fate of particles in the marine environment has been to analyze the sediments near the point of discharge for tracers of known origin. Given a waste input with a mass flux of tracer known over time, measurements of tracer mass retained in the sediments allows calculation of the per cent of discharged tracer found on the bottom.

Galloway (1972, 1979) performed the first study of trace metal accumulation in sediments down current from a marine outfall. For the White's Point outfall Galloway calculated the percentage of metals in the sewage effluent which accumulated in the sediments. Assumptions about the metal mass flux from the sewage outfall over its history were necessary. Another study of sewage particle accumulation in bottom sediments was conducted by Myers (1974). Myers used the difference in composition of carbon isotopes for land and marine organic matter as a tracer for sewage organic carbon in the sediments around White's Point. Other isotopic tracers have been used by Sweeney *et al.* (in press) to delimit sewage-impacted sediments.

The accumulation on continental shelves of fine grained particles discharged by rivers has been discussed by Drake (1976). Analysis of coastal sediments indicated significant accumulation of river borne

particles which could not have reached the sediments at their single particle settling velocities. Drake mentioned biological and physico-chemical processes which could aggregate the particles into faster settling larger particles, but there was no quantitative evaluation of the various aggregation mechanisms.

Direct measurements of sedimentation rates have been attempted with sediment traps placed near the sediment water interface. Mitchell (1976) placed sediment traps in Santa Monica Bay around the City of Los Angeles sludge outfall. The estimated total solid fallout in the outfall vicinity was over six times the amount of solids discharged from the outfall. The excessive sedimentation rate was probably due to collection of resuspended bottom sediment. McIntyre *et al.* (1976) have briefly mentioned the problems of cylindrical sediment traps, which overestimate settling rates because of changes in the water flow caused by the cylinder. McIntyre suggested that a standard sediment trap be developed and tested to allow collection of accurate sedimentation rate data. A thesis by Gardner (1977) discussed sediment trap design and collection efficiencies for laboratory experiments using flumes. Sediment traps tested in the laboratory were deployed in the ocean, but collection efficiencies were not independently verified under field conditions.

Recently Honjo (1978) has sampled settling particulate matter 214 meters off the bottom in the Sargasso Sea where the water is 5581 meters deep. Chemical analysis of the collected particles indicated that resuspended bottom sediment was also collected, hindering interpretation of the data.

1.1.3 Particle Coagulation Models

A number of studies have examined the coagulation of river borne particles and colloids in estuaries where high ionic strength lowers the electrostatic repulsion between particles and allows aggregation to occur (see Chapter 2). Krone (1963, 1972, 1976) has conducted laboratory and field investigations on the rheology of cohesive (coagulated) sediments. The shoaling of sediments in estuaries was found to be dependent on particle aggregation and breakup, turbulent intensity, tidal currents, and bottom scour. Krone's analysis has provided an explanation for the shoaling of sediments in estuaries, but does not predict particle aggregation and settling rates.

A laboratory investigation of clay coagulation and comparison with the clay distribution in estuary sediments were reported by Edzwald *et al.* (1974). Kaolinite was found to coagulate at a lower salinity than illite, and the sediments of one estuary reflected the trend with kaolinite concentrations greater in the upper reaches of the estuarine sediments, while illite accumulated in the sediments of the lower estuary.

Coagulation of colloidal matter in river water on mixing with seawater has been examined by Sholkovitz (1978). Laboratory experiments measured the total mass and chemical composition of particles formed when filtered river water was mixed with varying amounts of filtered seawater. At salinities greater than 17 parts per thousand (half the salinity of seawater) significant amounts of iron, manganese, aluminum, copper, nickel, and high molecular weight humic acids were removed by filtration. This technique measures only filterable

particle formation and cannot assess particle sedimentation in an estuary.

1.2 The Need for an Alternative Approach to Quantifying Particle Fate in Seawater

As has been discussed, various approaches have been used to model and measure the fate of particles and associated chemicals when discharged into seawater. The problems of these methods are reviewed and the direction of this research is outlined.

1.2.1 Problems with Previous Approaches

The use of sedimentation models, bottom sediment analysis, and coagulation models has not provided an adequate description of the fate of particles discharged into seawater.

There are a number of problems in the application of quiescent sedimentation experiments to conditions in the ocean. In the discharge of particles from a river, sewage outfall, dredge, or barge, the fluid motion is turbulent. Turbulence at low levels can promote particle coagulation while at higher levels it can cause aggregate breakup. After discharge the particle concentration is continuously being diluted, lowering the opportunity for particle collisions. The mechanisms of turbulence coagulation, breakup, and dilution are not represented in quiescent sedimentation experiments in seawater at fixed dilutions as commonly performed in laboratories.

In the analysis of bottom sediments for tracers of known origin, considerable uncertainty exists on both the mass of suspended matter or chemical tracers discharged over time, and the transport processes

occurring in the sediments. The procedure of Galloway (1972, 1979) and Myers (1974) used the reported wastewater flows from the time the outfall was put into operation and assumed the concentrations of metals and organic carbon were constant over this time period to arrive at mass fluxes. Tracer mobilization and transport processes in the sediments complicate the analysis and limit the usefulness of this method. Tracer mobilization has been measured over short time periods by Galloway and Myers and further discussed by Morel *et al.* (1975). Since the Los Angeles County outfalls have been in operation for over 30 years, quantitative predictions are not possible for the mobilization of metals and the degradation of organics from the sewage-impacted sediments.

A further complication of sediment tracer analysis in coastal sediments is the stochastic transport of bottom sediments by waves and currents. Greene (1976) observed the rapid disappearance of clay particles in the sediments near White's Point in southern California. The lack of detailed velocity measurements near the bottom sediments and of an understanding of cohesive sediment transport, as reviewed by Krone (1976), hinders quantifying the importance of this process. Mobilization from sediments and sediment transport away from the point of discharge can substantially reduce the amount of sediment and tracers present and lead to an underestimation of the amount of material initially reaching the sediments from the outfall. As was pointed out, sediment traps have not been developed which accurately measure the rate of particle fallout.

For sediment analysis and sedimentation rate measurements the information obtained is only applicable to the existing discharge site

and particle concentration. It is difficult to generalize the results to changes in waste characteristics or to other locations.

The experimental evidence of Krone (1963, 1972, 1976), Edzwald *et al.* (1974), Faisst (1976), and Sholkovitz (1978) has demonstrated the importance of particle coagulation in coastal waters receiving suspended and colloidal particles. Existing theories have not been available to predict the particle size distribution and settling velocity distribution for a coagulating particle suspension.

1.2.2 Present Approach

As has been pointed out, particle coagulation is an important mechanism which has not been coupled with settling and dispersion modeling efforts. The main hindrance to incorporating particle coagulation has been the absence of a verified theory of particle coagulation in particle suspensions with a continuous size distribution, such as are found in rivers, sewage effluents, and resuspended bottom sediments. This research presents theoretical predictions of coagulating and settling particle size distributions and the results of experiments designed to test the predictions. Predictions are for continuous particle size distributions which are applicable to natural aquatic systems.

In Chapter 2 theoretical approaches to coagulation are reviewed and results obtained for coagulating and settling aerosols are extended to obtain predictions for coagulating and settling hydrosols in a continuous distribution of particle sizes. Chapter 3 describes the experimental system designed to test the theoretical predictions and

Chapter 4 presents the experimental results and a discussion on the agreement between theory and experimental data. A summary of the thesis results is contained in Chapter 5.

CHAPTER 2

PARTICLE DYNAMICS FOR SEDIMENTATION AND COAGULATION

Sedimentation and coagulation cause the removal or loss of a particle of a given size from a volume of fluid. Sedimentation removes particles from the volume of fluid, while coagulation transports many smaller particles into fewer, larger particles within the fluid volume. This chapter reviews the basic sedimentation and coagulation mechanisms, and theories for hydrosol and aerosol dynamics. Because adequate theories were not available for continuous particle size distributions undergoing settling and coagulation, predictions of particle size distributions are derived after considerable simplification. Predictions are tested experimentally in the following chapters.

In natural and polluted waters there exists a continuous distribution of particle sizes. The most appropriate function for describing the dynamics of a continuous size distribution is the particle size distribution, $n(d_p)$, defined in the expression

$$dN = n(d_p)d(d_p) \tag{2.1}$$

where dN is the number of particles per fluid volume with diameters in the range d_p to $d_p + d(d_p)$. The particle size distribution has units of number per milliliter per micrometer, expressed as $[L^{-3}\ell^{-1}]$, where [L] represents a fluid length and [ℓ] as a particle length unit. In the dimensional analysis given in Section 2.4, independent dimensional homogeneity is required in fluid length and particle length. The same results can be obtained if particle mass is used instead of particle length (see Appendix E), but particle length is more convenient mechanistically and experimentally.

2.1 Sedimentation

The sedimentation flux of particles is the Stokes' settling velocity of a spherical particle of diameter d_p times the number of particles in the size interval d_p to $d_p + d(d_p)$

$$\text{sedimentation flux} = \frac{g}{18\nu}\left(\frac{\rho_p - \rho_f}{\rho_f}\right) d_p^2\, n(d_p)d(d_p) \qquad [L^{-2}t^{-1}] \qquad (2.2)$$

where g is the gravitational acceleration, ν, the kinematic viscosity, and ρ_p and ρ_f, the particle and fluid densities. The dimensional unit of time is indicated by [t]. If only settling were dominant in a particle suspension, the differential equation describing the particle size distribution would be

$$\frac{\partial n(d_p,z,t)}{\partial t} = -\frac{g}{18\nu}\left(\frac{\rho_p - \rho_f}{\rho_f}\right) d_p^2\, \frac{\partial n(d_p,z,t)}{\partial z} \qquad (2.3)$$

where z is positive downward.

2.2 Coagulation Mechanisms

Coagulation is the collision and sticking of two particles. The collision rate of particles of sizes d_i and d_j is given by their respective numbers and a collision function, $\beta(d_i,d_j)$, representing the geometry of the collision mechanism

$$\text{collision rate} = \beta(d_i,d_j)\; n(d_i)d(d_i)\; n(d_j)d(d_j) \qquad [L^{-3}t^{-1}] \qquad (2.4)$$

the collision function, β, has dimensions of fluid volume per time,

$[L^3t^{-1}]$. With the collision rate defined, an equation can be written for the change in particle size distribution over time. This equation can be more easily written in terms of particle volume, $v = \frac{\pi}{6} d_p^3$, instead of diameter because particle volume is conserved after collision while equivalent spherical diameter is not

$$\frac{\partial n(v)}{\partial t} = \frac{1}{2}\int_0^v \beta(\bar{v}, v-\bar{v}) n(\bar{v}) n(v-\bar{v}) d\bar{v} - \int_0^\infty \beta(v,\bar{v}) n(v) n(\bar{v}) \; d\bar{v} \; . \tag{2.5}$$

An alternate form of the equation is for a discrete particle size distribution, n_h, which is the number of particles of volume v_h

$$\frac{\partial n_h}{\partial t} = \frac{1}{2} \sum_{i+j=h} \beta(v_i, v_j) n_i n_j - n_h \sum_{i=1}^{\infty} \beta(v_i, v_h) n_i \; . \tag{2.6}$$

The first term on the right-hand side of both equations represents the rate of formation of particles of volume v and v_h respectively, while the second term is the rate of removal of particles of volume v and v_h through coagulation with particles of all sizes. Expressions for three common collision functions are reviewed below.

2.2.1 Brownian Coagulation

All particles are in motion due to their Brownian or thermal motion. An analytical expression for the Brownian collision function was obtained by Smoluchowski (see Friedlander, 1977) assuming the particles were noninteracting up to the time of collision. The collision function is

$$\beta_b(d_i,d_j) = \frac{2kT}{3\mu} \frac{(d_i+d_j)^2}{d_i d_j} \tag{2.7}$$

where k is the Boltzmann constant, T, absolute temperature, and μ, the fluid viscosity. Corrections to this collision function for electrostatic, van der Waals, and hydrodynamic forces between particles are available (Spielman, 1970; Honig *et al.*, 1971).

2.2.2 Shear Coagulation

If a fluid is being sheared in either laminar or turbulent flow, particles traveling with the fluid will collide. Again, Smoluchowski was the first to present an analysis of the collision mechanism assuming no particle or hydrodynamic forces (Friedlander, 1977). The collision function for shear coagulation is

$$\beta_{sh}(d_i,d_j) = \frac{G}{6} (d_i + d_j)^3 \tag{2.8}$$

where G is the shear rate. In laminar flow the shear rate is the fluid velocity gradient, while for turbulent flow, the shear rate is related to the rate of turbulent energy dissipation, ε,

$$G \sim \left(\frac{\varepsilon}{\nu}\right)^{1/2} . \tag{2.9}$$

Corrections to the collision function for electrostatic, van der Waals, and hydrodynamic forces are available for particles of equal size (van de Ven and Mason, 1977; Zeichner and Schowalter, 1977). For collisions between spheres of unequal size, predictions are not available. The experimental data of Manley and Mason (1955) indicated that hydrodynamic forces greatly limited particle collisions.

2.2.3 Differential Sedimentation Coagulation

For particles with a density not equal to the fluid density, gravitational settling will cause larger particles to collide with slower settling particles. The collision function for this mechanism is the collision cross section times the difference in particle settling velocities, assuming constant particle density and Stokes' flow

$$\beta_{ds}(d_i,d_j) = \frac{\pi g}{72\nu}\left(\frac{\rho_p-\rho_f}{\rho_f}\right)(d_i+d_j)^2\left|d_i^2-d_j^2\right| \quad . \tag{2.10}$$

Hydrodynamic forces are known to limit the effectiveness of this mechanism for water droplets in the air (Mason, 1971) but corrections are not available for particles suspended in water.

2.3 Previous Solutions for Coagulating and Settling Particles

Various techniques are available for solving forms of the general coagulation equation, Equation (2.5) or (2.6) with or without particle settling. Two general approaches are solutions for particles uniform in size, that is, monodisperse, and solutions for continuous particle size distributions, polydisperse.

2.3.1 Monodisperse Systems

The complexity of coagulation can be greatly simplified if all the particles are the same size and settling is ignored. Equation (2.6) can be reduced to a simple expression in terms of the total number of particles, N, of initial size d_p

$$\frac{dN}{dt} = -\frac{1}{2}\beta(d_p,d_p)N^2 \quad . \tag{2.11}$$

Collision functions for Brownian and shear coagulation are considered below, but for differential sedimentation coagulation no particle collisions are expected because $\beta_{ds}(d_p,d_p) = 0$.

For Brownian coagulation, the collision function of Equation (2.7) reduces to

$$\beta_b(d_p,d_p) = \frac{8kT}{3\mu} \tag{2.12}$$

which, when substituted into Equation (2.11) has the solution

$$N(t) = \frac{N_o}{1+\frac{4kT}{3\mu}N_o t} \tag{2.13}$$

where N_o is the number of particles at $t = 0$. This solution is valid only for times less than the half time of the reaction, $t < 3\mu/4kTN_o$. This prediction for monodisperse particles undergoing Brownian coagulation has been experimentally verified by Swift and Friedlander (1964), but the observed rate constant was a factor less than the theoretical value. This factor has been explained by the influence of van der Waals and hydrodynamic forces (Lichtenbelt *et al.*, 1974).

For shear coagulation, the collision function of Equation (2.8) with $d_i=d_j=d_p$ substituted into Equation (2.11) gives

$$\frac{dN}{dt} = -\frac{2}{3}G\,d_p^{\,3}N^2 \quad . \tag{2.14}$$

Noting that coagulation without settling preserves total particle volume, $V = \frac{\pi}{6} d_p^3 N$, and making the substitution gives

$$\frac{dN}{dt} = -\frac{4}{\pi} VGN \tag{2.15}$$

which after integration becomes

$$N(t) = N_o e^{-\frac{4}{\pi} VGt} . \tag{2.16}$$

This solution like the monodisperse Brownian solution is valid for only the initial coagulation period, $t < \pi/4VG$. The first order rate expression has been experimentally verified by Swift and Friedlander (1964) in laminar flow and by Birkner and Morgan (1968) for turbulent flow. The observed first order rate constant was less than theoretically predicted, but the difference has been explained by the interaction of van der Waals and hydrodynamic forces (van de Ven and Mason, 1977; Zeichner and Schowalter, 1977).

The above experiments of Swift and Friedlander, Birkner and Morgan, and Lichtenbelt *et al.* were conducted in high ionic strength solutions to compress the diffuse layer of counter ions surrounding the charged particles and to eliminate the importance of electrostatic forces between particles. Considerable literature has been based on the theory developed by Derjaguin and Landau, and Verwey and Overbeek (DLVO) to predict the influence of ionic strength on coagulation rates. Recent experimental data reviewed by Overbeek (1977) have not been in agreement with theoretical predictions. Inclusion of particle coagulation in the secondary minimum of the diffuse layer potential has not resolved the

discrepancy between theory and experiments (Marmur, 1979; Prieve and Ruckenstein, 1980). Application of DLVO theory to predict colloid stability and coagulation rates at low ionic strengths should be approached with caution.

The assumptions necessary for obtaining Equations (2.13) and (2.16) do not hold for polydisperse distributions encountered in practice, and the monodisperse analysis for Brownian or shear coagulation cannot be applied quantitatively to natural aquatic environments.

2.3.2 Polydisperse Systems

One of the major problems in the monodisperse solutions is the limitation that $d_i=d_j=d_p$ in the collision functions. Over time, aggregates form and collide with primary particles and with other aggregates which are not included in the derivation. There have been two approaches in the hydrosol and aerosol literature for obtaining solutions for coagulation in continuous size distributions. One approach is a solution of Equation (2.5) or (2.6), the continuous and discrete versions with and without sedimentation. The other approach has been an asymptotic solution for later times by a self-preserving transformation of Equation (2.5). Both approaches suffer from a lack of information on the validity of the collision functions for the various coagulation mechanisms when particles of different sizes collide.

2.3.2.1 Direct Analytical and Numerical Solutions

Various analytical and numerical solutions have been obtained for coagulation in a polydisperse system. The simplest solution is to assume the collision function is independent of particle

size so that Equation (2.6), the discrete coagulation equation, becomes a system of coupled first order differential equations which has an analytical solution derived by Smoluchowski (see Hidy, 1965). Hidy (1965) compared the analytical result with a numerical solution of the discrete equation including the diameter dependence of the Brownian collision function. The analytical and numerical results were in close agreement. For shear coagulation Saffman and Turner (1956) compared the analytical solution neglecting the size dependence in the collision function with a numerical result which included the size dependence. They found the analytical result severely underestimated the number of large aggregates compared to numerical integration of the more accurate, diameter-dependent collision function.

Various attempts at solving the discrete equation for shear coagulation of hydrosols have been troubled by limited computer capacity and lack of a verified model for large particle breakup. Fair and Gemmell (1964) and Harris *et al.* (1966) considered aggregates containing up to 100 primary particles, an effective diameter range of only 4.6. Fair and Gemmell modeled coagulation in a batch reactor while Harris *et al.* examined a series of continuous flow reactors.

More recently, numerical solutions of the continuous coagulation equation have been presented which avoid the problem of a small size range in the discrete solutions. Two recent examples are Gelbard (1979) for aerosol dynamics and Lawler *et al.* (in press) for hydrosol dynamics. These authors considered coagulation over a broad range of particle sizes for homogeneous suspensions without settling, causing particles to accumulate in the largest size interval. Lawler *et al.* included

sedimentation in their model of a sedimentation tank. Experimental data were not available to verify the predictions of these models.

2.3.2.2 Self-Preserving Transformation Solutions

Partial solutions to the continuous coagulation equation have been obtained by self-preserving transformations. Friedlander (1960a,b) showed that the continuous Brownian coagulation equation with gravitational settling could be reduced from a partial integro-differential equation to an ordinary integro-differential equation by a similarity transformation. The continuous shear coagulation equation also had a self-preserving transformation and Swift and Friedlander (1964) showed experimentally that the size distribution of coagulating hydrosols approached a self-preserving distribution after sufficient time. Hidy (1965) has indicated the cumulative size distribution used by Swift and Friedlander for data presentation is not as sensitive to variations as other distributions. Wang and Friedlander (1967) demonstrated that a self-preserving transformation exists for simultaneous Brownian and shear coagulation only if the shear rate over time was proportional to the total number of particles.

While the concept of a self-preserving transformation has had considerable utility in aerosol coagulation studies, the application to hydrosols is limited. For aerosols Brownian coagulation is usually the dominant collision mechanism while for hydrosols, Brownian and shear coagulation are known to be important and possibly coagulation by differential sedimentation. Thus, for hydrosols all coagulation mechanisms must be considered and the restriction of a time varying

shear rate to obtain a self-preserving transformation is not a general result with wide application. Also, quantitative application of the self-preserving transformation requires knowledge of the unknown corrections to the shear and differential sedimentation collision functions for hydrodynamic and van der Waals forces.

2.3.3 Summary

This section has discussed the approaches used by various investigators to predict the behavior of coagulating hydrosols and aerosols. The methods for monodisperse distributions are only applicable for short time periods and for uniform particles made in the laboratory. Various numerical solutions to the general coagulation equation have been obtained but they have not been experimentally verified and the results lack generality. Partial solutions obtained by self-preserving transformations have only restricted applicability to hydrosol coagulation studies. An alternative approach is discussed in the next section which attempts to correct some of these limitations but requires considerable simplification.

2.4 Prediction of Particle Size Distributions from Coagulation and Sedimentation Mechanisms

To consider particle coagulation and settling in a continuous particle size distribution, a theoretical approach different from the methods discussed previously is needed. In this section, predictions are obtained for a coagulating and settling particle size distribution after a number of simplifications which allow solutions by dimensional analysis. The analysis is a modification of that used by Friedlander (1960a,b) to obtain aerosol size distributions.

2.4.1 Simplification

The first simplification is to assume only one coagulation or sedimentation mechanism is dominant in a subrange of particle size. Figure 2.1 is a comparison of the collision functions for collision of an arbitrary particle with a particle of 1 μm diameter. Values of the collision functions were obtained directly from Equations (2.7), (2.8) and (2.10) for low fluid turbulence and low density particles. Because the collision functions plotted do not include the previously mentioned particle surface and fluid forces, this plot only approximates the dominance of a coagulation mechanism over a particle size interval. For particles less than 1 μm, Brownian motion is the dominant collision mechanism, while particles from 1 to about 100 μm collide due to fluid shearing for the conditions assumed in this plot. Collisions of a 1 μm particle with particles greater than 100 μm are by differential sedimentation coagulation. Replotting Figure 2.1 for collisions with other than a 1 μm particle would shift the curves but still retain the ordering of the dominant mechanisms: Brownian, shear, and differential sedimentation with increasing size of colliding particle.

Particle removal by gravitational settling cannot be compared with the collision functions in Figure 2.1, but it is reasonable to assume that the largest particles would be removed from the fluid volume by settling.

Three further assumptions are necessary in the analysis. First, particles are assumed to have a low stability, independent of particle size. Destabilization can be achieved by compression of the electrical

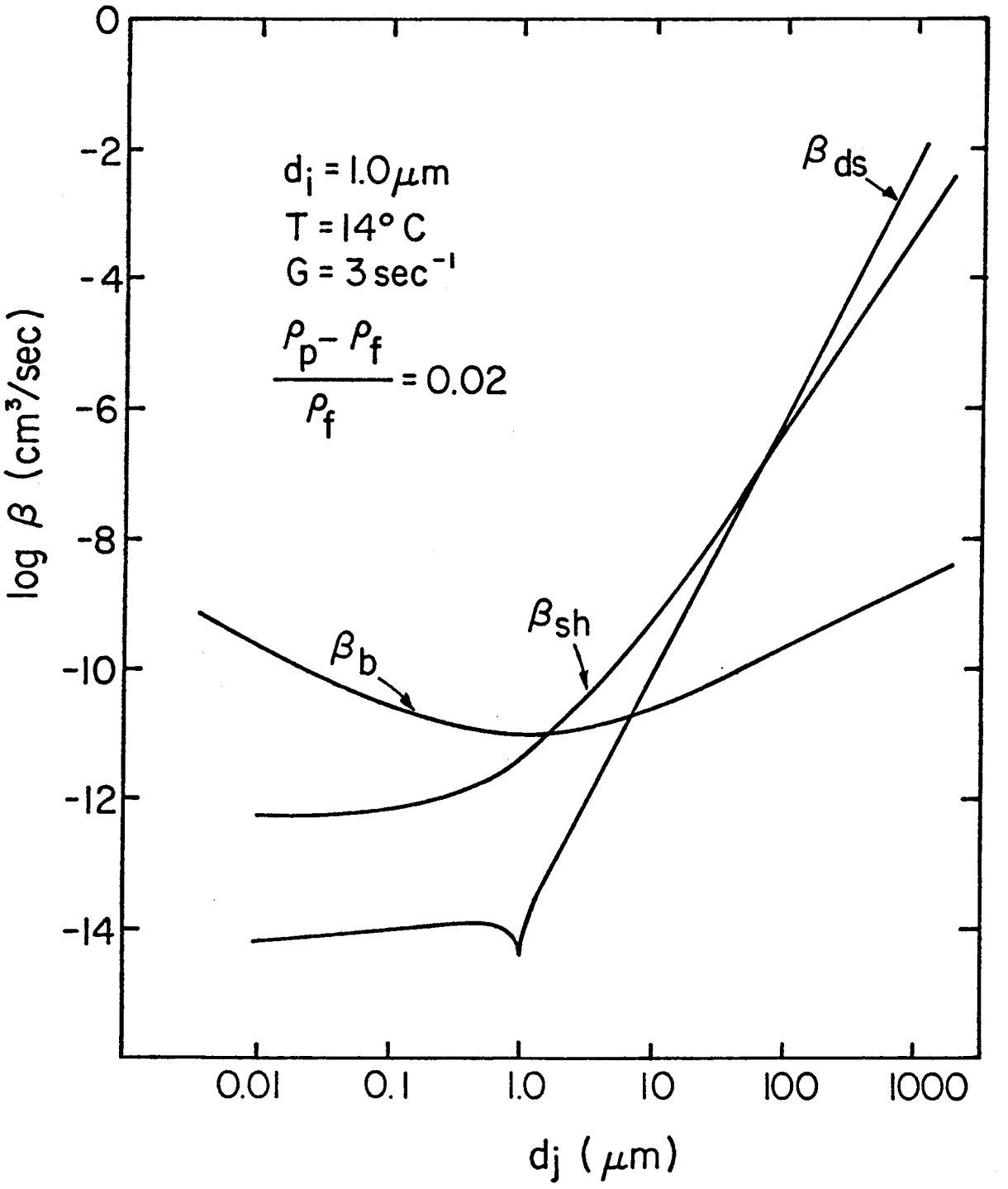

Figure 2.1 Comparison of collision functions for Brownian (b), shear (sh), and differential sedimentation (ds) coagulation.

double layer in a high ionic strength solution or by surface charge neutralization through specific chemical interaction with oppositely charged atoms or molecules. Second, the particle size distribution is in a dynamic steady state. For each small interval of particle size, the rate of particle volume transferred into the size interval by coagulation is balanced by either the volume coagulated from the interval or the particle volume lost from the fluid volume by sedimentation. This steady state assumption implies the existence of a constant flux of particle volume through the distribution which is equal to the rate of formation of small particles and to the rate of large particle removal by sedimentation. The flux of particle volume is denoted by E with units of particle volume per fluid volume per time $[\ell^3 L^{-3} t^{-1}]$.

The third assumption requires that the particle size distribution is a function of six variables: 1) particle diameter, 2) the flux of particle volume through the distribution, parameters representing 3) Brownian, 4) shear, and 5) differential sedimentation coagulation, and 6) a gravitational settling parameter. Parameters for the sedimentation and coagulation mechanisms are obtained from fluid and particle constants appearing in Equations (2.2), (2.7), (2.8) and (2.10). The resulting parameters and the units obtained from the mechanism equations are

Brownian	$K_b = \frac{kT}{\mu}$	$[L^3 t^{-1}]$
shear	G	$[L^3 \ell^{-3} t^{-1}]$
differential sedimentation	$K_{ds} = \frac{g}{\nu}\left(\frac{\rho_p - \rho_f}{\rho_f}\right)$	$[L^3 \ell^{-4} t^{-1}]$

settling $$S = \frac{g}{\nu}\left(\frac{\rho_p - \rho_f}{\rho_f}\right) \qquad [L\ell^{-2}t^{-1}] \quad .$$

The parameters for differential sedimentation coagulation and settling have the same grouping of constants but different units because differential sedimentation is second order in the particle size distribution from Equation (2.4), while gravitational settling is first order in the size distribution as seen in Equation (2.2). All parameters were chosen to be independent of particle size, assuming further that particle density is independent of particle size.

2.4.2 Predictions

Based on the above assumptions, the particle size distribution has the following functional form

$$n = n(d_p, E, K_b, G, K_{ds}, S) \quad . \tag{2.17}$$

The assumption of steady state has removed the time dependence.

Predictions of the particle size distribution are obtained by considering subranges of particle size where only one coagulation mechanism or gravitational settling is dominant. For the smallest particle sizes Brownian coagulation is dominant and the functional relationship is

$$n = n(d_p, E, K_b) \tag{2.18}$$

which contains four variables (n, d_p, E, K_b) and three dimensions (L, ℓ, and t). Dimensional analysis is used to group the variables into a unique, nondimensional expression

$$A_b = n(d_p)\ d_p^{5/2}\left(\frac{K_b}{E}\right)^{1/2} \tag{2.19}$$

where A_b is a dimensionless constant. Solving for the particle size distribution gives

Brownian $$n(d_p) = A_b\left(\frac{E}{K_b}\right)^{1/2} d_p^{-2.5} \tag{2.20}$$

Using the same technique for regions dominated by shear, differential sedimentation, and settling, the predicted size distributions are

shear $$n(d_p) = A_{sh}\left(\frac{E}{G}\right)^{1/2} d_p^{-4} \tag{2.21}$$

differential sedimentation $$n(d_p) = A_{ds}\left(\frac{E}{K_{ds}}\right)^{1/2} d_p^{-4.5} \tag{2.22}$$

settling $$n(d_p) = A_s\left(\frac{E}{S}\right)^{3/4} d_p^{-4.75} \tag{2.23}$$

Equations (2.20) and (2.23) were derived earlier by Friedlander (1960a,b) for aerosols. The method of dimensional analysis arrives at predictions which contain dimensionless coefficients A_b, A_{sh}, A_{ds}, and A_s which must be determined experimentally.

Tests of the theoretical predictions can best be done by transforming the size distributions into volume distributions

$$\frac{dV}{d(\log d_p)} = \frac{2.3\pi}{6} d_p^4\ n(d_p) \tag{2.24}$$

where 2.3 is ℓn 10.

The predicted volume distributions are

Brownian $$\frac{dV}{d(\log d_p)} = \frac{2.3\pi}{6} A_b \left(\frac{E}{K_b}\right)^{1/2} d_p^{1.5} \quad (2.25)$$

shear $$\frac{dV}{d(\log d_p)} = \frac{2.3\pi}{6} A_{sh} \left(\frac{E}{G}\right)^{1/2} \quad (2.26)$$

differential sedimentation $$\frac{dV}{d(\log d_p)} = \frac{2.3\pi}{6} A_{ds} \left(\frac{E}{K_{ds}}\right)^{1/2} d_p^{-0.5} \quad (2.27)$$

settling $$\frac{dV}{d(\log d_p)} = \frac{2.3\pi}{6} A_s \left(\frac{E}{S}\right)^{3/4} d_p^{-0.75} \; . \quad (2.28)$$

Hunt (in press) has successfully compared observed oceanic size distributions with the predictions. The predictions also appear to account for maximums in particle concentration observed in oceanic thermoclines which result from decreased fluid turbulence in the stable fluid of the thermocline.

2.4.3 Normalization

For comparison of predicted particle size distributions with observations, and for simplification of data presentation, normalization is used. Particle diameters are normalized by the characteristic diameter at which particles have Brownian collisions and shear induced collisions at the same rate. From the dimensions of the Brownian parameter, K_b, $[L^3t^{-1}]$ and the shear parameter, G, $[L^3\ell^{-3}t^{-1}]$ a characteristic particle length of $(K_b/G)^{1/3}$ is obtained. An alternate approach is to equate the collision functions for Brownian and shear coagulation from Equations (2.7) and (2.8) assuming $d_i = d_j = d_p$ and solving for d_p. An expression $d_p = (2K_b/G)^{1/3}$ is obtained similar to the above result.

A dimensionless particle diameter, δ, is defined as

$$\delta = d_p \left(\frac{G}{K_b}\right)^{1/3} \tag{2.29}$$

which will normalize data such that Brownian coagulation is expected to be dominant for $\delta \ll 1$ and shear coagulation is expected to be dominant for $\delta \gg 1$. Using the predicted shear coagulation volume distribution from Equation (2.26) and normalizing the right-hand side defines a normalized volume distribution, $d\bar{V}/d(\log \delta)$, on the left-hand side

$$\frac{d\bar{V}}{d(\log \delta)} \equiv \frac{dV}{d(\log d_p)} \left(\frac{G}{E}\right)^{1/2} = \frac{2.3\pi}{6} A_{sh} \, . \tag{2.30}$$

The predictions for coagulation and settling normalized volume distributions are

Brownian
$$\frac{d\bar{V}}{d(\log \delta)} = \frac{2.3\pi}{6} A_b \, \delta^{1.5} \tag{2.31}$$

shear
$$\frac{d\bar{V}}{d(\log \delta)} = \frac{2.3\pi}{6} A_{sh} \tag{2.32}$$

differential sedimentation
$$\frac{d\bar{V}}{d(\log \delta)} = \frac{2.3\pi}{6} A_{ds} \frac{G^{2/3}}{K_{ds}^{1/2} K_b^{1/6}} \delta^{-0.5} \tag{2.33}$$

settling
$$\frac{d\bar{V}}{d(\log \delta)} = \frac{2.3\pi}{6} A_s \left(\frac{E}{S^3}\right)^{1/4} \left(\frac{K_b}{G}\right)^{-19/12} \delta^{-0.75} \, . \tag{2.34}$$

Equations (2.33) and (2.34) are included only for completeness; another normalization procedure would be better suited for examining these predictions.

CHAPTER 3

EXPERIMENTAL METHODS

This chapter describes the experimental methods used for testing the validity of the predicted particle size distributions. The approach taken was to use an experimental apparatus which would allow determination of all parameters appearing in the predictions and evaluation of the dimensionless coefficients.

3.1 Artificial Seawater

For coagulation studies, a reproducible fluid of fixed ionic composition is essential. The artificial seawater prepared for the experiments was based on a recipe of Lyman and Fleming given in Riley and Skirrow (1965) and listed in Table 3.1. The compounds $NaC\ell$, $MgC\ell_2$, and Na_2SO_4 were weighed out as needed, while the remaining compounds were prepared in separate stock solutions at 100 times their concentration in seawater using distilled deionized water. For each liter of artificial seawater, the three salts were weighed out and dissolved in approximately 0.9 liter of distilled deionized water, then ten milliliters of each stock solution were added and mixed. Distilled deionized water was added to make one liter. Reagent grade chemicals were used throughout.

Suspended particles were removed from the artificial seawater by vacuum filtration through 0.22 μm Millipore filters (type GS). Filters were not washed before use, but the first 20 milliliters of filtrate were discarded. Typically, one filter of 45 cm diameter was used for

each liter of artificial seawater. The artificial seawater was stored in one liter Nalgene bottles and used in less than a week after preparation, as the solutions became contaminated after longer periods. The measured pH of one filtered artificial seawater solution was 7.8.

Table 3.1 Composition of artificial seawater modified from Riley and Skirrow (1965) using Lyman and Fleming recipe.[a]

Compound	Concentration (g/L)
$NaC\ell$	24.014[b]
$MgC\ell_2$	5.095
Na_2SO_4	4.007
$CaC\ell_2$	1.127
$KC\ell$	0.679
$NaHCO_3$	0.196
KBr	0.098
H_3BO_3	0.027
$SrC\ell_2$	0.025
NaF	0.003

3.2 Preparation of Solids

Choice and preparation of solids used in coagulation experiments were based on their previous use in coagulation studies, importance in the aquatic environment, and the ability to prepare the solids in a consistent and reproducible manner. With these considerations in mind,

---

[a] To convert formality to molarity a seawater density of 1.02286 g/cm^3 was assumed based on a salinity of 34.33 parts per thousand at 25°C.

[b] Actual $NaC\ell$ concentration used was 24.104 g/L.

three representative clays (kaolinite, illite, and montmorillonite) and a silica mineral were selected for experimental testing of the predicted coagulating size distribution. Appendix A discusses some preliminary experiments using dilute oil in water emulsions.

3.2.1 Clays

Clays make up a major component of the fine particles less than 2 μm in size suspended in rivers. Because the small clay particles have a high surface area for pollutant adsorption there is considerable interest in clay coagulation in seawater. Since clays are not pure or uniform in size and chemical composition, procedures of clay preparation and clay properties are important. The clays used in these experiments were obtained from Ward's Natural Science Establishment, Inc. and are representative of those clays analyzed by the American Petroleum Institute's (A.P.I.) Clay Mineral Standards Project (Kerr *et al.*, 1949-50). Clay washing and converting to the sodium form followed recommended procedures of van Olphen (1977).

3.2.1.1 Kaolinite

Kaolinites are 1:1 layer clays, nonexpandable in water and generally have low exchange capacities. The kaolinite used in the coagulation experiments was from Oneal Pit, Macon, Georgia, A.P.I. No. 4. For this clay, Kerr *et al.* (1949-50) estimated 8 to 12 per cent impurities and a base exchange capacity of 12.2 milli-equivalents per 100 grams of dried clay (meq/100g).

Kaolinite preparation involved grinding, washing out dissolved salts, converting clay surface to the sodium form, washing out excess

salt and exchanged ions, disruption by sonication followed by removal of larger particles by sedimentation. Clay chunks were broken by hand into one centimeter sized particles and dried overnight at 100°C, then ground for 24 hours in a Paul O. Abee, Inc. Roll Mill with porcelain balls. Ground clay was suspended in distilled deionized water and wet sieved to remove particles greater than 45 μm (No. 325 USA Standard Testing Sieve). Clay suspension was washed twice with distilled deionized water, and the liquid was removed by centrifugation. Clay pellet was resuspended in 0.22 μm filtered 2 M NaCℓ and left in contact for four days to exchange any cations on kaolinite surface for sodium ions. Seven washings with distilled deionized water were required to remove the excess ions, which continued to coagulate the clay suspension up to the fourth washing. The clay suspension was sonicated and allowed to settle quiescently to remove clay particles greater than 2 μm. Sodium kaolinite coagulation experiments were conducted nine months after clay preparation.

3.2.1.2 Illite

Illites are 2:1 layer clays, nonexpandable in water, with intermediate exchange capacities. The illite sample was from Fithian, Illinois, A.P.I. No. 35, having approximately 12 per cent impurities and a base exchange capacity of 25.0 meq/100g (Kerr *et al.*, 1949-50).

Sodium illite preparation was similar to kaolinite: drying for 43 hours, grinding for nine hours, four washings in distilled deionized water, soaked in filtered 2 M NaCℓ for three days, five washings with distilled deionized water, sonication, and quiescent settling to remove

2 μm particles. Illite experiments were completed within one month of preparation.

3.2.1.3 Montmorillonite

Montmorillonites are 2:1 layer clays, expandable in water, with high exchange capacities. The montmorillonite sample was from Otay, California, A.P.I. No. 24, with four per cent impurities and a base exchange capacity of 153.0 meq/100g (Kerr *et al.*, 1949-50).

As above, the clay was dried for 23 hours, ground for 13 hours, washed three times in distilled deionized water, soaked four days in 2 M NaCℓ, washed six times in distilled deionized water, sonicated, and quiescently settled to remove particles greater than 2 μm. Sodium montmorillonite experiments were completed within two months of preparation.

3.2.2 Silica

A finely divided crystalline silica called Min-U-Sil 5 (Pennsylvania Glass Sand Corp.) was the fourth mineral prepared for coagulation experiments. Min-U-Sil 5 has been used previously as a reproducible particle suspension in a number of coagulation experiments (O'Melia and Stumm, 1967; Hahn and Stumm, 1968; Kasper, 1971). Unlike previous coagulation experiments with Min-U-Sil, a cleaning procedure developed by Vuceta (1976) was followed to remove surface impurities. Organics were removed by heating the powder at 500°C for 24 hours and then refluxed in 4 N HNO_3 for 20 hours to remove inorganic impurities. Eight washings in distilled deionized water removed the acid. The silica was briefly resuspended in 4 N NH_4OH and given eight washings to remove the base. The silica suspension was sonicated and 2 μm

particles were removed by settling. Min-U-Sil 5 has a reported surface mean particle diameter of 1.1 μm and electron micrographs showed irregularly shaped particles (Kasper, 1971). Silica coagulation experiments were completed within one month of preparation.

3.3 Measurement of Particle Size and Calculation of Particle Size Distribution

Aggregates were counted and sized with a Model ZBI Coulter Counter interfaced with a Nuclear Data particle sizing amplifier and multichannel analyzer. The particle size sensing technique is based on changes in solution resistance caused by the passage of a particle through a small orifice. Imposing a constant current through the orifice will cause a voltage change proportional to the particle volume. The signal pulses from particles passing through the orifice are logarithmically amplified in the particle sizing amplifier and then the multichannel analyzer distributes and stores the pulses. Data in the multichannel analyzer are punched onto paper tape for later calculation of particle size distributions. Because the system differs from that used by Treweek (1975) and Faisst (1976) at this laboratory, a complete description of the calibration procedures and size distribution calculations is presented in Appendix B. One problem with this sizing technique is that larger aggregates break up before they enter the sensing zone of the orifice and thus, cannot be sized.

3.4 Experimental Control of Shear Rate

The fluid shear rate, G, is the only parameter appearing in the predicted coagulating size distributions that readily permits

experimental variation. For the Brownian coagulation parameter, the absolute temperature and fluid viscosity have small variations in the natural seawaters of interest. The differential sedimentation coagulation parameter and the settling parameter each contain, ρ_p, the aggregate density. The choice of a solid particle determines the individual solid particle density, but the aggregate density is not under experimental control.

Fluid shear can be obtained in laminar or turbulent flow, and shear coagulation kinetics of monodisperse particles in laminar and turbulent flow were found comparable (Swift and Friedlander, 1964; Birkner and Morgan, 1968). For experiments designed to test predictions, laminar shear in the gap between rotating cylinders is used because of a number of advantages over turbulent flow. First, the shear rate in the gap is defined by the rotation rate of the cylinder, and with a narrow gap there is little deviation from the mean value. Second, in the coagulation experiments laminar flow allows particles to settle out at their Stokes-settling velocity which is not possible in turbulent flow because of resuspension. Third, turbulence commonly generated in the laboratory for coagulation experiments is not homogeneous or isotropic (Birkner and Morgan, 1968; Argaman and Kaufman, 1968). Because of a distribution in shear rates experienced by aggregates, occasionally high shear rates found near paddles and baffles could cause disruption of aggregates, a topic not under consideration here. Finally, due to a lower limit of detection for Coulter Counters, to observe a Brownian-dominated regime requires low shear rates that are very difficult to obtain in turbulent flows. The smallest particles

detected by Coulter Counters are approximately 0.7 μm, and the particle diameter, in micrometers, that separates Brownian from shear-dominated coagulation is given by (see Section 2.4.3)

$$d_p = \left(\frac{2kT}{\mu G}\right)^{1/3} \simeq 2.1\ G^{-1/3} \quad . \tag{3.1}$$

For Brownian coagulation to be dominant at 0.7 μm requires turbulent shear rates less than 27 sec^{-1}, which are difficult to generate in the laboratory. One complication of laminar fluid shear is that a dynamic steady state size distribution will not exist. Instead, a quasi-dynamic steady state is obtained where size distributions measured over time are similar in shape but decreasing in magnitude.

The concentric rotating cylinder apparatus used in the experiments is sketched in Figure 3.1. A Bodine NSH-12 electric motor with Minarik Model SL14 speed controller provided a constant rotation rate. The rotation rate of the motor was reduced by two notched pulleys connected by a notched timing belt providing a 3.43 to 1 speed reduction. Further reduction in rotation rate by 60 to 1 was obtained with a Rampe speed reducer. With this arrangement outer cylinder rotation rates down to 3/4 revolutions per minute were obtained corresponding to G = 1/2 sec^{-1}. For shear rates greater than 8 sec^{-1} the two pulleys were reversed. Cylinders were constructed of Lucite, and surfaces in contact with liquid were coated with an epoxy paint (aquapon, Pittsburgh Paints). Support for cylinders and motor was machined from aluminum and anodized to prevent corrosion. During operation a lead brick with an approximate mass of 12 kilograms was placed on the base plate to damp out vibrations.

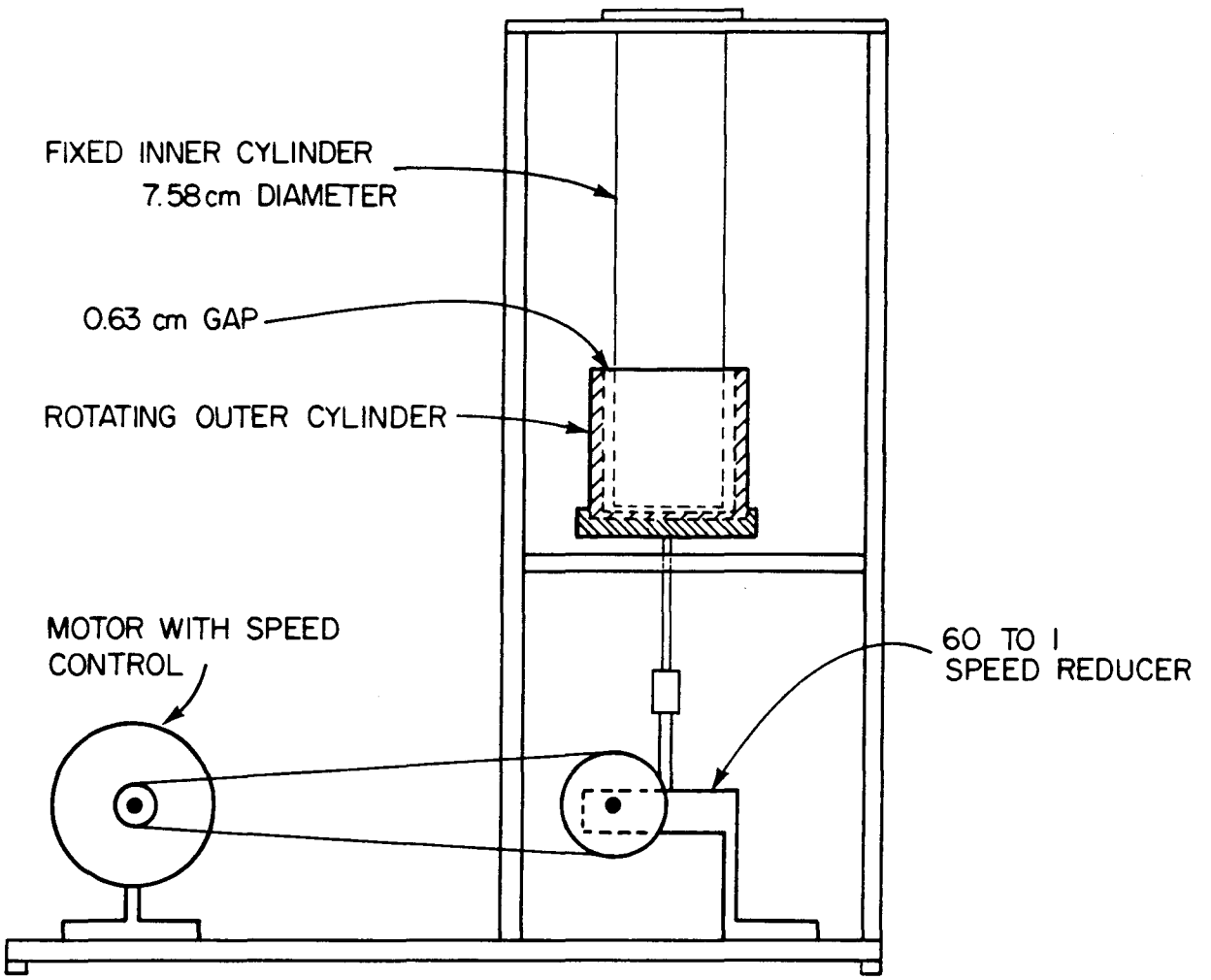

Figure 3.1 Rotating cylinder apparatus.

the laminar flow rotating cylinder apparatus can at best obtain a quasi-dynamic steady state in the particle size distribution, a method is needed to calculate the instantaneous volume flux during an experiment.

Calculation of changes in total suspended particle volume would be possible if a particle sizing instrument were available to measure the complete particle size distribution. Since the Coulter Counter and multichannel analyzer system used in this research cannot obtain a complete size distribution because of electronic noise limitations and aggregate disruption (see Appendix B), an alternative means for obtaining particle volume is needed. Suspended solids measurements are not possible for the low concentrations encountered and limited solution volume in the rotating cylinder apparatus.

Following a technique used by Bradley and Krone (1971), the particle volume in suspension was determined by light absorbance of the dispersed suspension. Absorbance was related to suspended particle volume by calibration with solutions of known suspended solids concentration in artificial seawater. The amount of suspended solids was obtained by 0.2 μm Nucleopore filtration and the total suspended volume was calculated using an assumed solid density. Absorbance measurements were made with a 1 cm or a 5 cm cell in a Beckman ACTA CIII Spectrophotometer at a wavelength that depended on the particular solid. Suspension absorbance is a measure of light scattered by particles. (Calibration curves are given in Chapter 4.)

The instantaneous volume flux through the distribution is related to the suspended volume by

$$E(t) \simeq - \frac{dV(t)}{dt} \quad . \tag{3.3}$$

The reason the equation is only approximate is discussed below. Because a large number of measurements of suspended volume are not possible during an experiment, the volume data were fitted to a function of time which could be differentiated. From the predicted coagulating and settling size distribution, an expression is derived in Appendix D for the total volume change with time

$$V(t) = \frac{1}{a+bt} \tag{3.4}$$

where a and b are constants and b is proportional to the shear rate, G. Substituting this expression into Equation (3.3) gives

$$E(t) \simeq bV^2(t) \ . \tag{3.5}$$

From plots of inverse volume with time, lines of slope b are obtained and used with the instantaneous volume to compute the instantaneous volume flux.

The reason Equations (3.3) and (3.5) are approximate is illustrated in Figure 3.2 showing volume distributions at time t_1 and at some later time t_2. Regions dominated by Brownian and shear coagulation and settling are indicated. The decrease in the diameter region of shear dominance and the increased region of settling dominance at t_2 is obtained dimensionally. The break between shear coagulation and settling can be a function of only three parameters, G, S, and E which combine to give a characteristic particle diameter $G^{2/3}S^{-1}E^{1/3}$. The dependence on G and S are as expected and as the volume flux decreases during an experiment, the region dominated by settling shifts to smaller diameters as indicated in Figure 3.2. The volume

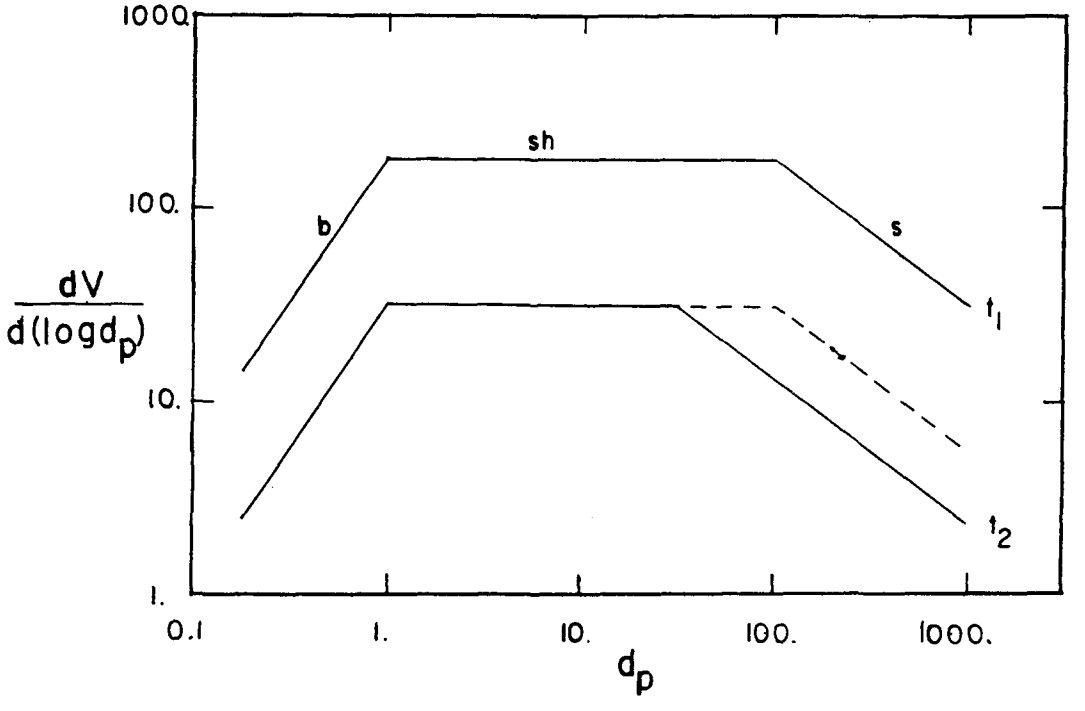

Figure 3.2 Predicted volume distributions at two times (t_1,t_2) during a batch experiment showing the shift in settling dominance (s) to lower particle diameters as the total suspended volume decreases.

lost from the distribution by coagulation and settling is the difference in areas under the curves at t_1 and t_2. This includes the area between the dashed line and the t_2 volume distribution which is volume lost by sedimentation due to decreased coagulation opportunity at lower particle concentrations. This "extra" area contributes to volume lost but does not represent particle volume that experienced Brownian and shear coagulation. Thus, the approximation of Equation (3.3) overestimates the volume flux for Brownian and shear coagulation.

CHAPTER 4

EXPERIMENTAL RESULTS AND DISCUSSION

This chapter presents the experimental data for four solids coagulating and settling in artifical seawater. The first section describes the kaolinite results followed by sections for illite, montmorillonite, and silica. Each section contains 1) the calibration curves relating total suspended volume to suspension absorbance, 2) a tabulation of total suspended volumes, instantaneous volume fluxes, and the removal rate constant during experiments at various shear rates, 3) plots of inverse total suspended volumes versus time, 4) plots of volume distributions and normalized volume distributions, 5) one plot of all normalized volume distributions for each solid at all shear rates, and 6) comparison of the results with the theoretical predictions of Chapter 2.

In the fifth section of this chapter, the experimental results are compared and explanations are offered for the differences in the volume distributions and removal rates observed between the four solids. In the last section these results are compared with previous studies of clay and silica coagulation kinetics reported in the literature.

4.1 Kaolinite Experiments

The sodium kaolinite experiments in artifical seawater verified the Brownian and shear coagulation predictions within the uncertainty of the experimental methods.

Figure 4.1 plots total suspended volume against absorbance for

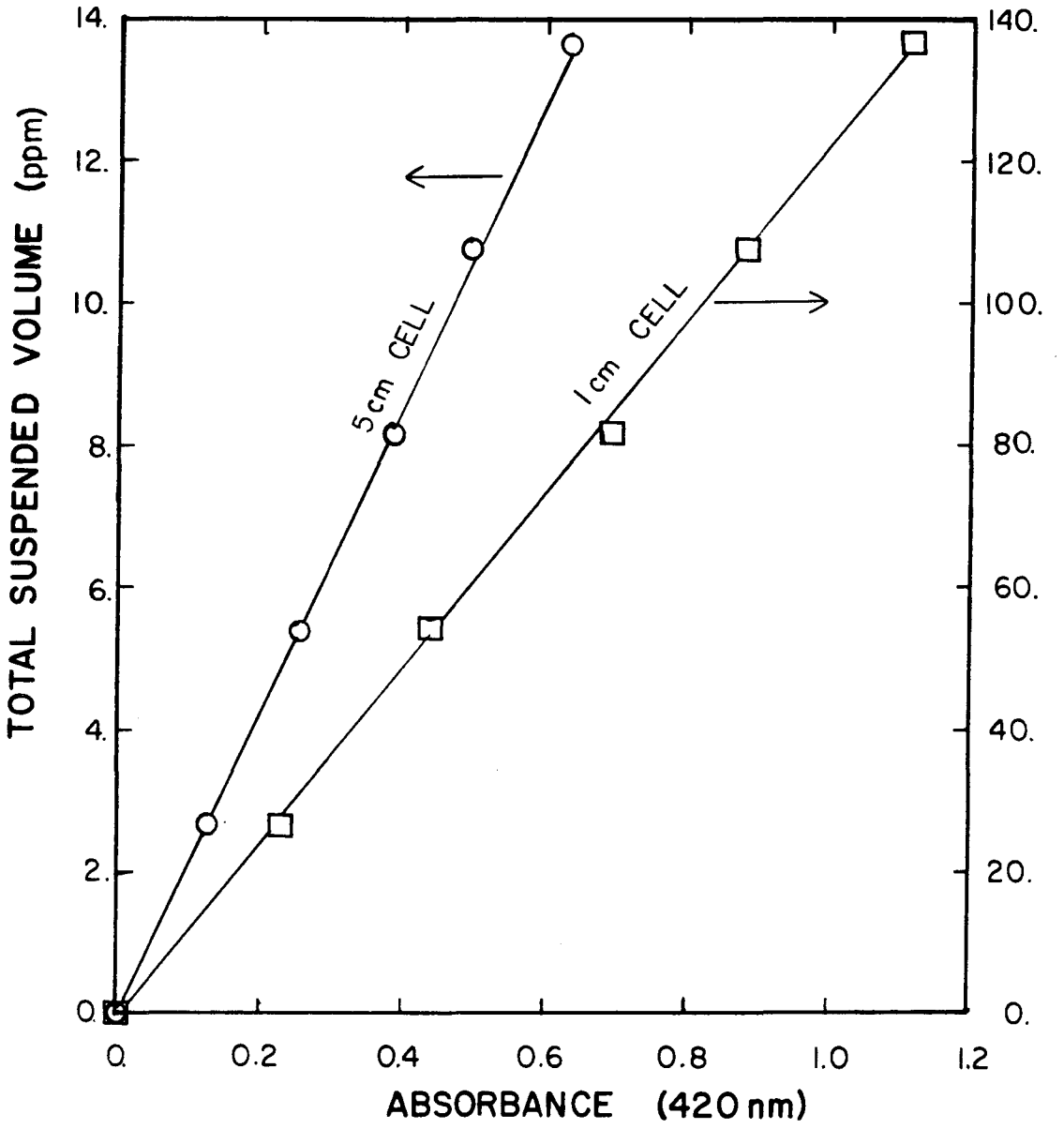

Figure 4.1 Relationship between absorbance and total suspended volume for kaolinite in artificial seawater.

kaolinite suspended in seawater. Total suspended solids measured by filtration was converted to total suspended volume by assuming a solid density of 2.5 g/cm^3. Absorbance was measured at 420 nanometers (nm) with 1 cm and 5 cm cells. Regression lines were linear out to an absorbance of 1.0, and the equations for estimating total suspended volume, V, in parts per million (ppm) from absorbance are

$$\text{1 cm cell} \quad V = -0.9 + 123.\ (\text{ABSORBANCE}) \quad r^2 = 0.9991 \qquad (4.1)$$

$$\text{5 cm cell} \quad V = -0.06 + 21.6\ (\text{ABSORBANCE}) \quad r^2 = 0.9996. \qquad (4.2)$$

Regressions included the origin because the absorbance of filtered artificial seawater was defined to be zero and filter weights were corrected for an artificial seawater blank.

Experiments were conducted at shear rates of 1,2,4,8,16, and 32 sec^{-1} with five or six samples withdrawn during each shear rate experiment for total volume and size distribution determination. At the start of each experiment the total suspended volume of kaolinite was 276 ppm. Measured total suspended volumes are given in Table 4.1 and plots of inverse total volumes versus time are given in Figure 4.2. Slopes from Figure 4.2, the removal rate constants (b), were used to calculate instantaneous volume fluxes, $E(t) = bV(t)^2$. Values of the removal rate constants and volume fluxes are included in Table 4.1.

The inverse volume plots versus time are usually linear as expected theoretically from Equation (3.4), and the rate of volume removal increased as the shear rate increased up to 16 sec^{-1}. Nonlinearities observed at $G = 2\ sec^{-1}$ were due to variations in the depth at which samples were withdrawn, as discussed in Section 4.2. At $G = 32\ sec^{-1}$ the

Table 4.1 Total suspended volume (V), volume flux (E), and volume removal rate constant (b) for kaolinite experiments at shear rates of 1,2,4,8,16, and 32 sec^{-1}.

$G = 1\ sec^{-1}$

Time (min)	V (ppm)	E (ppm/sec)
25	52.	51. $x10^{-3}$
40	28.	14.9 $x10^{-3}$
60	18.9	6.8 $x10^{-3}$
90	10.6	2.1 $x10^{-3}$
130	7.2	0.98 $x10^{-3}$

$b = 1.90\ x10^{-5}\ ppm^{-1}/sec$

$G = 2\ sec^{-1}$

Time (min)	V (ppm)	E (ppm/sec)
15	65.	97. $x10^{-3}$
25	34.	27. $x10^{-3}$
40	20.	11.6 $x10^{-3}$
60	10.6	3.9 $x10^{-3}$
90	6.3	1.39 $x10^{-3}$

$$b = \begin{cases} 2.3\ x10^{-5}\ ppm^{-1}/sec & < 40\ min. \\ 2.9\ x10^{-5}\ ppm^{-1}/sec & = 40\ min. \\ 3.5\ x10^{-5}\ ppm^{-1}/sec & > 40\ min. \end{cases}$$

$G = 4\ sec^{-1}$

Time (min)	V (ppm)	E (ppm/sec)
10	79.	275. $x10^{-3}$
25	23.	23. $x10^{-3}$
40	10.7	5.0 $x10^{-3}$
60	7.1	2.2 $x10^{-3}$
80	5.1	1.14 $x10^{-3}$
110	6.5	---

$b = 4.4\ x10^{-5}\ ppm^{-1}/sec$

$G = 8\ sec^{-1}$

Time (min)	V (ppm)	E (ppm/sec)
10	51.	135. $x10^{-3}$
20	21.	23. $x10^{-3}$
30	9.9	5.1 $x10^{-3}$
40	8.2	3.5 $x10^{-3}$
60	5.4	1.52 $x10^{-3}$

$b = 5.2\ x10^{-5}\ ppm^{-1}/sec$

Table 4.1 (continued)

$G = 16\ sec^{-1}$			$G = 32\ sec^{-1}$		
Time (min)	V (ppm)	E (ppm/sec)	Time (min)	V (ppm)	E (ppm/sec)
10	38.	117. $x10^{-3}$	10	57.	153. $x10^{-3}$
15	19.8	32. $x10^{-3}$	15	31.	45. $x10^{-3}$
20	13.3	14.3 $x10^{-3}$	20	23.	25. $x10^{-3}$
27	9.2	6.9 $x10^{-3}$	30	13.3	8.3 $x10^{-3}$
35	8.3	---	45	10.2	---
$b = 8.1\ x10^{-5}\ ppm^{-1}/sec$			$b = 4.7\ x10^{-5}\ ppm^{-1}/sec$		

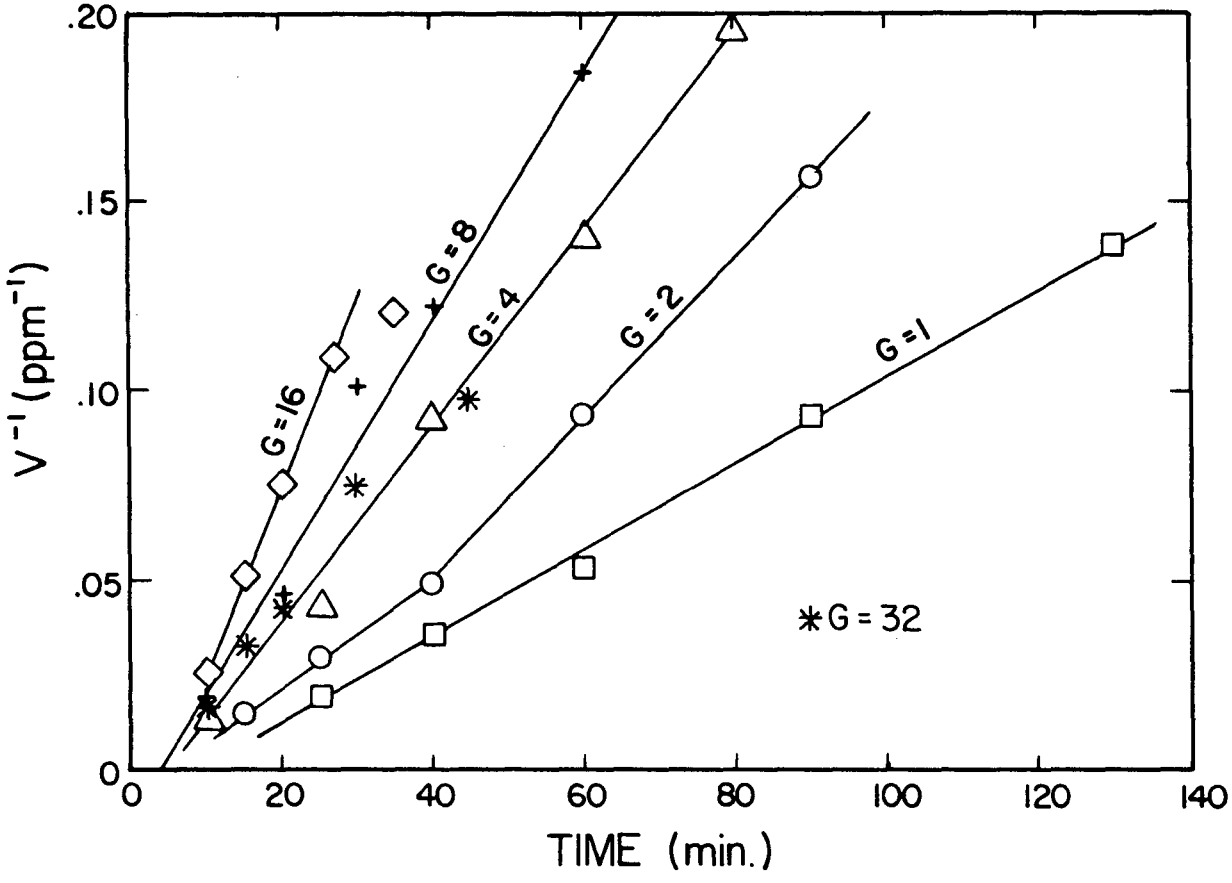

Figure 4.2 Inverse total suspended volumes during kaolinite experiments at shear rates of 1,2,4,8,16, and 32 sec^{-1}.

removal rate decreased because of a fluid instability with the rotating cylinder apparatus which hindered settling. The last samples collected for the G = 4, 16, and 32 sec^{-1} experiments were below the linear inverse volume plots of Figure 4.2 because of sampling problems caused by withdrawal of large volumes needed for absorbance measurements with the 5 cm cell.

Figures 4.3 through 4.8 present volume distributions and normalized volume distributions for the kaolinite experiments. All kaolinite volume distributions were measured with a 30 μm aperture, which caused the breakup during counting of aggregates greater than about 1.2 μm. Data collected with larger apertures were totally dominated by breakup during counting as indicated in Appendix B. For each shear rate the measured volume distributions did not change in shape over time, only magnitude, showing the maintenance of quasi-dynamic steady state or self-similar distributions. Volume distributions were normalized according to procedures discussed in Section 2.4.3 using the shear rate and the instantaneous volume fluxes listed in Table 4.1. The Brownian coagulation parameter, $K_b = kT/\mu$, had a constant value in experiments with all of the different solids of 4.384×10^{-12} cm^3/sec because experiments were conducted at room temperature (T = 296°K, $\mu = 0.933 \times 10^{-2}$ g/sec-cm). Following discussion of the results for each shear rate, the normalized volume distributions are replotted on one graph, excluding the larger diameters dominated by breakup during counting.

For the G = 1 sec^{-1} experimental results in Figure 4.3 the volume distributions with a vertical spread of a factor of 4 were reduced to less than a factor of 2 on normalization. A line of slope 3/2,

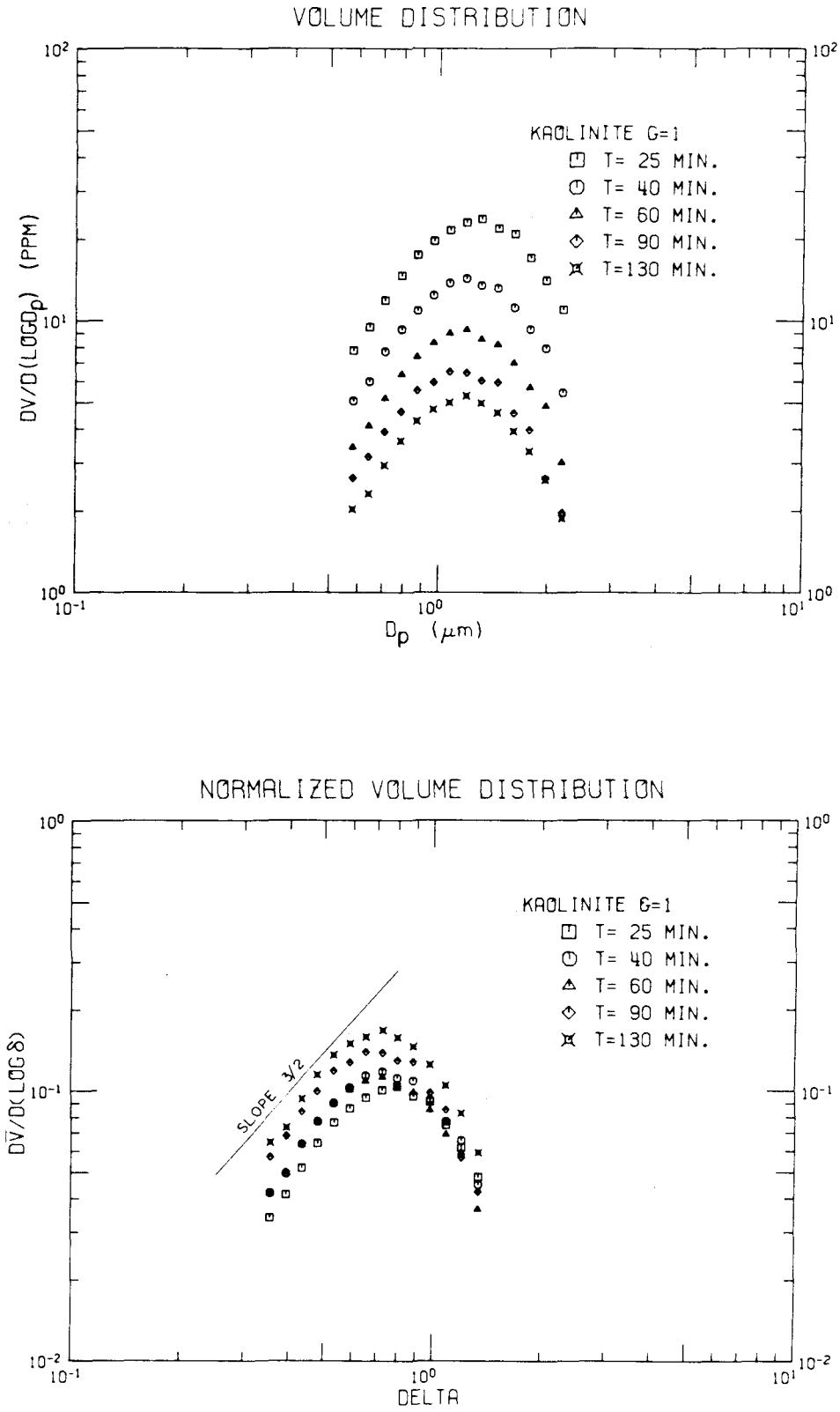

Figure 4.3 Volume distributions and normalized volume distributions for kaolinite at $G = 1\ sec^{-1}$.

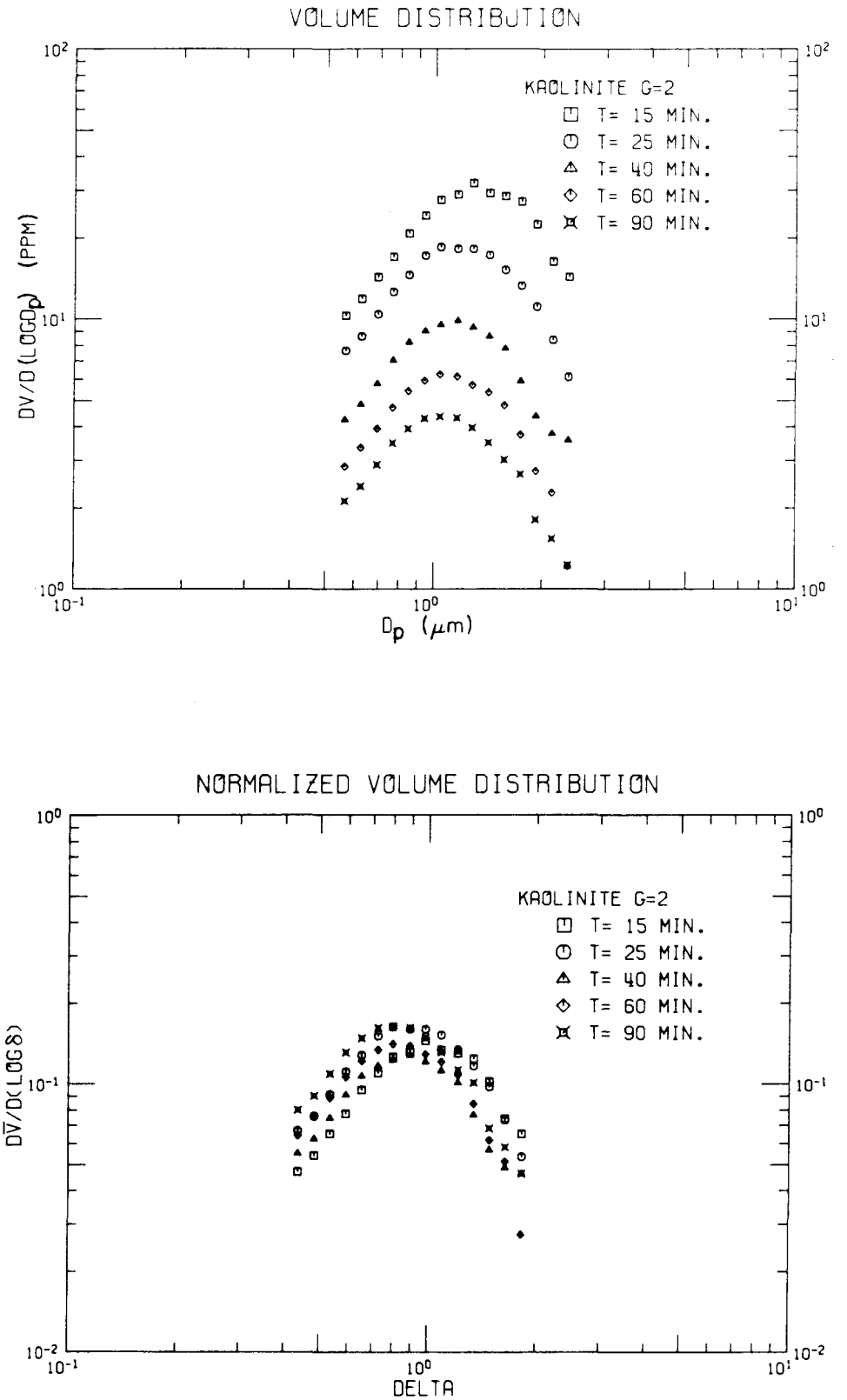

Figure 4.4 Volume distributions and normalized volume distributions for kaolinite at G = 2 sec^{-1}.

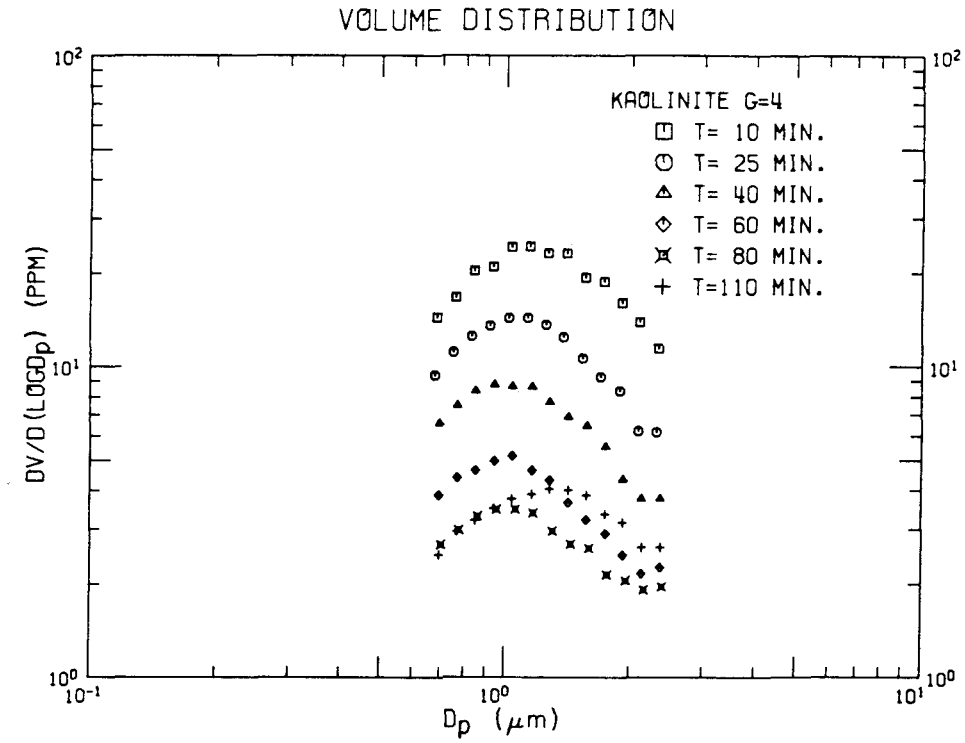

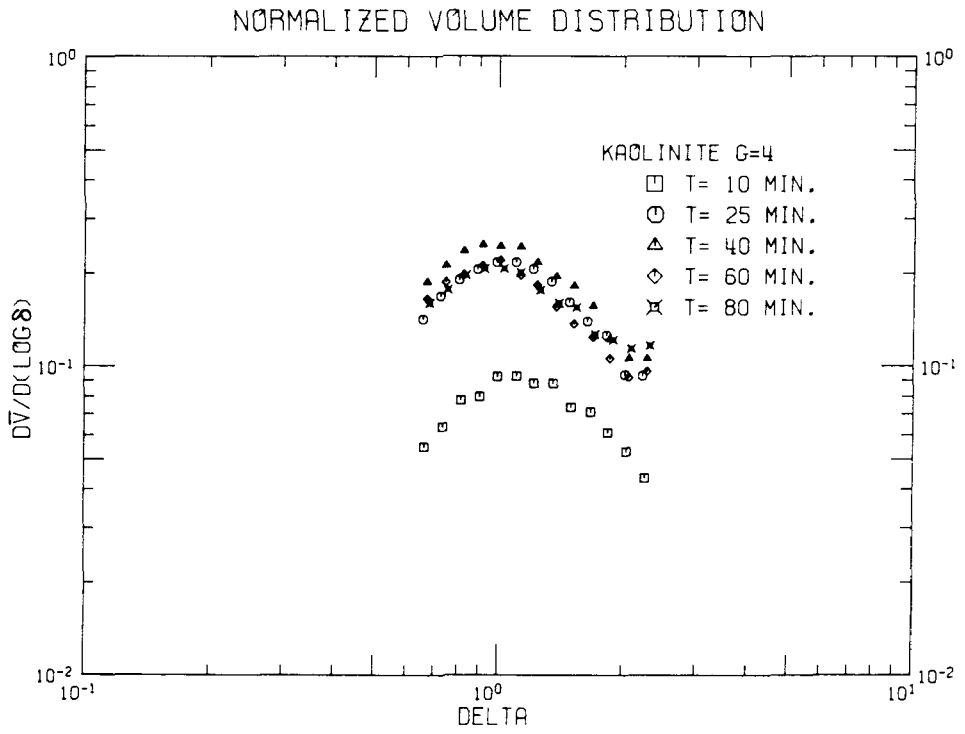

Figure 4.5 Volume distributions and normalized volume distributions for kaolinite at $G = 4\ sec^{-1}$.

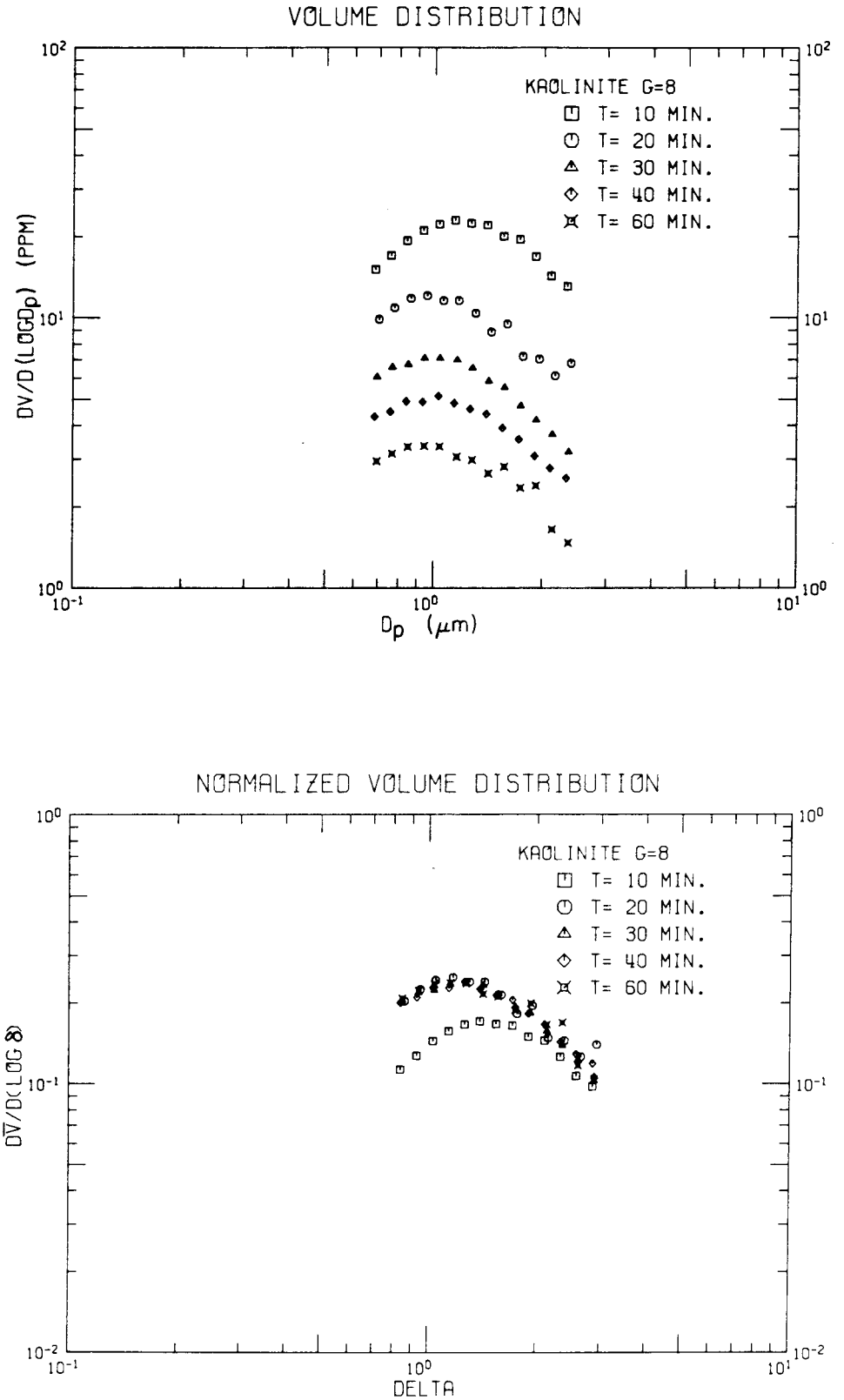

Figure 4.6 Volume distributions and normalized volume distributions for kaolinite at G = 8 sec^{-1}.

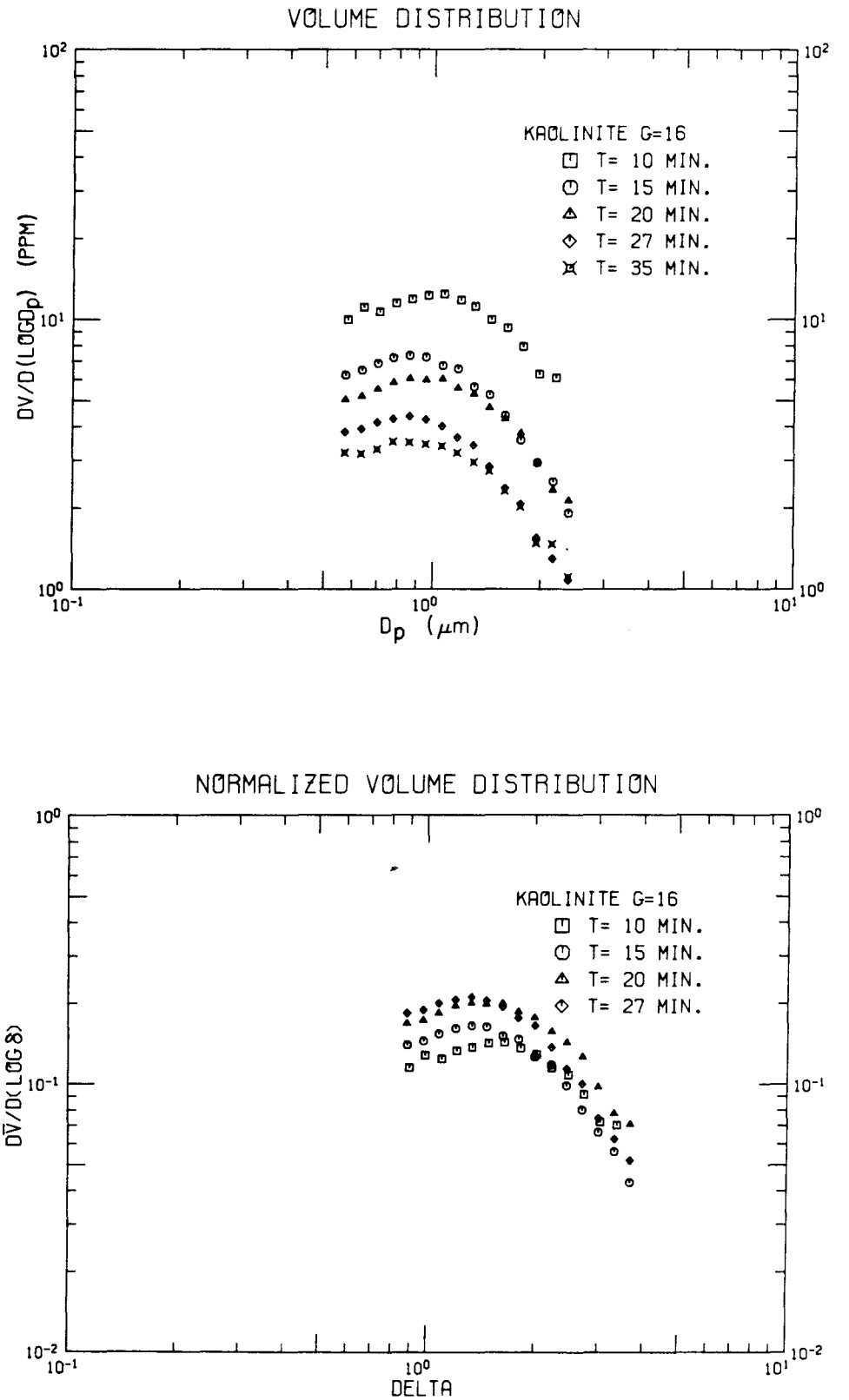

Figure 4.7 Volume distributions and normalized volume distributions for kaolinite at $G = 16\ sec^{-1}$.

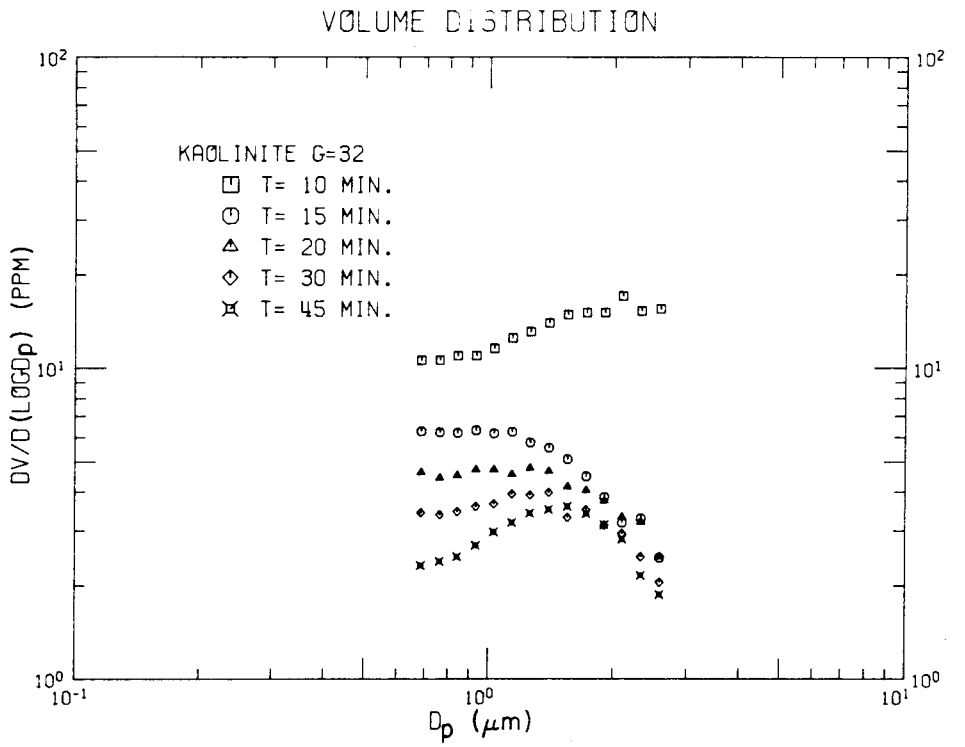

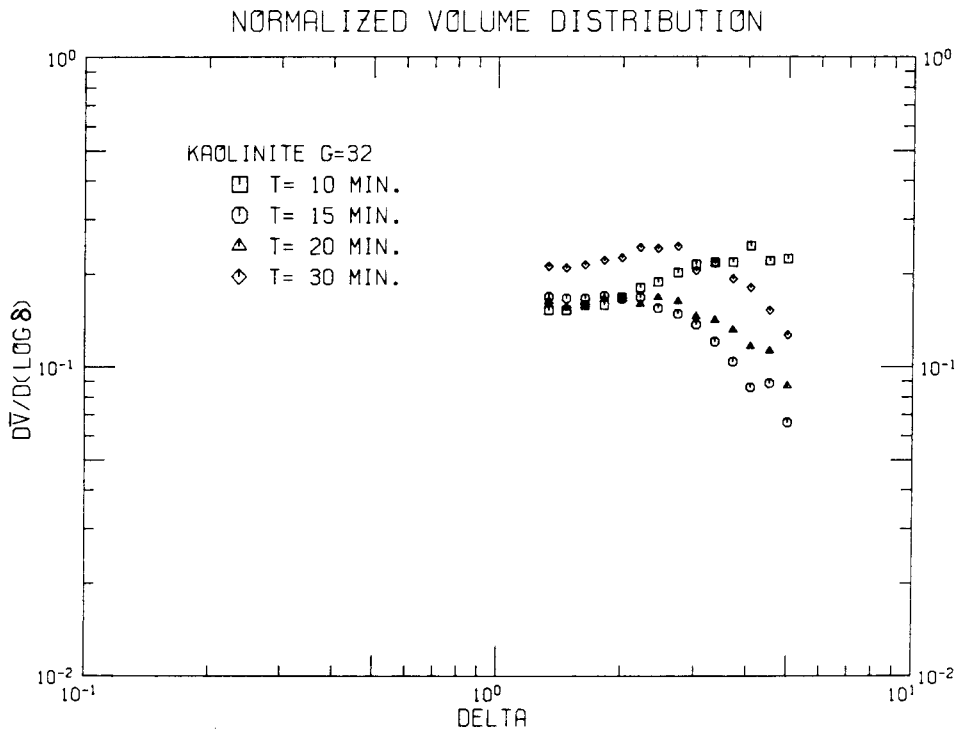

Figure 4.8 Volume distributions and normalized volume distributions for kaolinite at G = 32 sec^{-1}.

the Brownian prediction, drawn on the normalized plot, indicates the general trend of the smaller diameter data. The data do not strictly follow a 3/2 slope and have a hump at larger deltas which probably represents some pieces of larger aggregates broken up during counting. The trend in the normalized data of low values of the normalized volume distribution for earlier times and high values for later times was due to the approximation necessary in computing the volume flux as discussed in Chapter 3.

The volume distributions for $G = 2\ sec^{-1}$ given in Figure 4.4 were substantially reduced in spread on normalization. A Brownian coagulation dominated regime was present for smaller deltas.

The $G = 4\ sec^{-1}$ experimental results shown in Figure 4.5 have less of a Brownian dominated region, as expected for the higher shear rate. The volume distribution of the 110 minute sample did not agree with earlier samples and indicates that a sampling problem distorted the data. On normalization the distributions collapsed very well, except for the ten minute sample. The sample at ten minutes was probably taken too early and the distribution of larger aggregates did not have time to reach the quasi-dynamic steady state. The large total suspended volume in the early sample overestimated the volume flux and depressed the normalized distribution. The decline of the distributions for larger diameters was not as steep as in the previous experiments, but the trend of the data did not follow the differential sedimentation coagulation or gravitational settling predictions with slopes of -1/2 and -3/4, respectively.

On increasing the shear rate to $8\ sec^{-1}$, Brownian dominated volume distributions are evident only for $d_p < 0.9\ \mu m$ in Figure 4.6. After

normalization, the volume distributions collapsed onto one curve except for the ten minute sample. As in the $G = 4\ sec^{-1}$ experiment, the dynamic steady state was not achieved after 10 minutes. For larger diameters the decline in volume distributions was similar to the $G = 4\ sec^{-1}$ results.

At a shear rate of $16\ sec^{-1}$, level distributions in Figure 4.7 indicate the possible dominance of shear coagulation. Normalization of the first four samples reduced the spread in the data substantially. Unlike the $G = 4$ and $8\ sec^{-1}$ results, the sample obtained at ten minutes agreed with the other normalized distributions, indicating steady state was established sooner at the higher shear rate. These distributions have a hump at about 1 μm representing pieces of larger aggregates broken up during counting.

Kaolinite volume distributions for the highest shear rate of $32\ sec^{-1}$ are shown in Figure 4.8. Except for a sampling problem at 45 minutes, the data have a level shear coagulation dominated region followed by a region dominated by breakup during counting. For an unknown reason, the volume distribution at ten minutes increased at larger diameters. On normalization the spread was reduced. The data for $G = 32\ sec^{-1}$ should be viewed with suspicion because the removal rate constant was less than at $16\ sec^{-1}$ indicating coagulation and settling were not the only mechanisms influencing the distributions and the volume removal rate. This point is discussed further in Section 4.5 when the results for the different solids are compared.

While the results at the different shear rates followed the Brownian and shear predictions, a complete test of the predictions

requires that all the normalized data for all shear rates fall on one curve, as indicated by Equations (2.31) and (2.32), repeated below

$$\text{Brownian} \qquad \frac{d\bar{V}}{d(\log \delta)} = \frac{2.3\pi}{6} A_b \delta^{1.5} \tag{4.3}$$

$$\text{shear} \qquad \frac{d\bar{V}}{d(\log \delta)} = \frac{2.3\pi}{6} A_{sh} \, . \tag{4.4}$$

The normalized volume distribution data for all shear rates are plotted in Figure 4.9 excluding the ten minute samples for $G = 4$ and 8 sec^{-1}. Also, only the data not dominated by particle breakup during counting were plotted, which for all shear rates was for particle diameters less than about 1.2 μm.

The normalized data for all shear rates were in agreement with the Brownian and shear coagulation predictions. Lines drawn by eye on Figure 4.9 are at a 3/2 slope, the Brownian prediction, and level, the shear prediction. The vertical spread of the data was generally dominated by the spread at each shear rate, especially for $G = 1$ and 2 sec^{-1}. The break between Brownian dominance and shear dominance occurred at about $\delta = 1$, as expected, and the dimensionless constants A_b and A_{sh} have approximate values of 0.19 and 0.15, respectively.

Thus, within the uncertainties of the experimental system, the Brownian and shear coagulation predictions have been verified for sodium kaolinite in artificial seawater. The breakup of larger aggregates during counting prevented testing of predictions for size distributions dominated by differential sedimentation coagulation and gravitational settling.

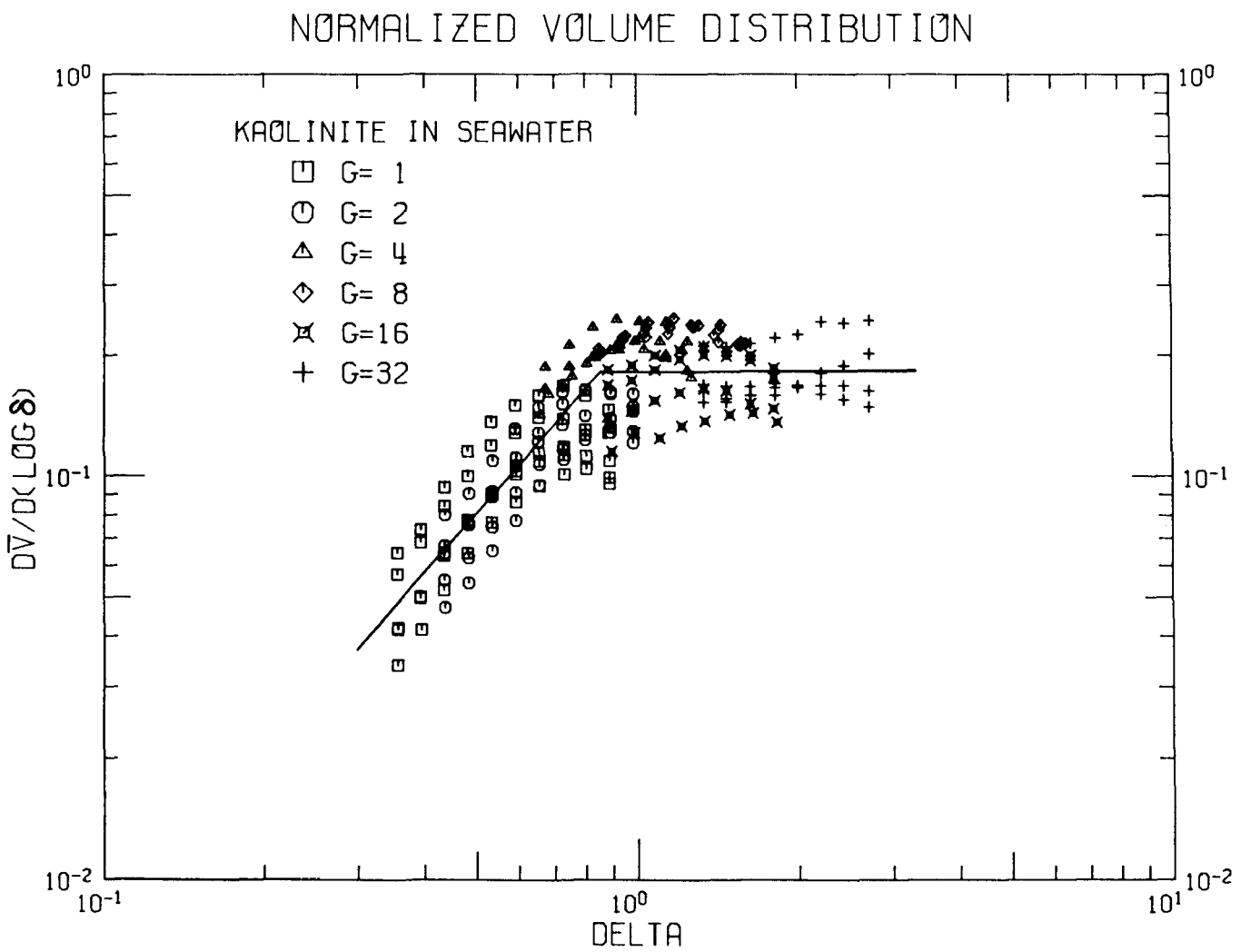

Figure 4.9 Normalized volume distributions for kaolinite at G = 1,2,4,8,16, and 32 sec^{-1}.

4.2 Illite Experiments

Experiments with sodium illite in artificial seawater verified the Brownian and shear coagulation predictions.

Figure 4.10 contains the calibration curves used to obtain total suspended volume from illite suspension absorbance. A solid density of 2.5 g/cm^3 was assumed and absorbance was measured at 375 nm. The calibration curves were linear for absorbances less than 0.5 and the resulting linear regressions were

$$\text{1 cm cell} \quad V = 0.32 + 92.6\ (\text{ABSORBANCE}) \quad r^2 = 0.998 \tag{4.5}$$

$$\text{5 cm cell} \quad V = 0.009 + 17.82\ (\text{ABSORBANCE}) \quad r^2 = 0.999. \tag{4.6}$$

Experiments were conducted at shear rates of 1/2,1,2,4,8,16, and 32 sec^{-1} with five or six samples withdrawn during each experiment for total volume and size distribution determination. At the start of each experiment the total suspended volume of illite was 90 ppm. Table 4.2 contains a summary of total suspended volumes, volume fluxes, and the volume removal rate constants obtained from Figure 4.11. Except for the data at $G = 2$ and 4 sec^{-1}, the inverse total volumes during the experiments were linear with time. For the illite experiments the removal rate increases up to 8 sec^{-1} then declines at 16 sec^{-1}, and there is no volume removal at $G = 32$ sec^{-1}.

The two linear regions observed at $G = 2$ and 4 sec^{-1} in Figure 4.11 were caused by the removal of large volumes for the last two samples. Because the 5 cm sampling tube was at a fixed position, large sample volumes lowered the water surface, resulting in sampling of solution nearer the surface. The lower suspended particle volume concentration

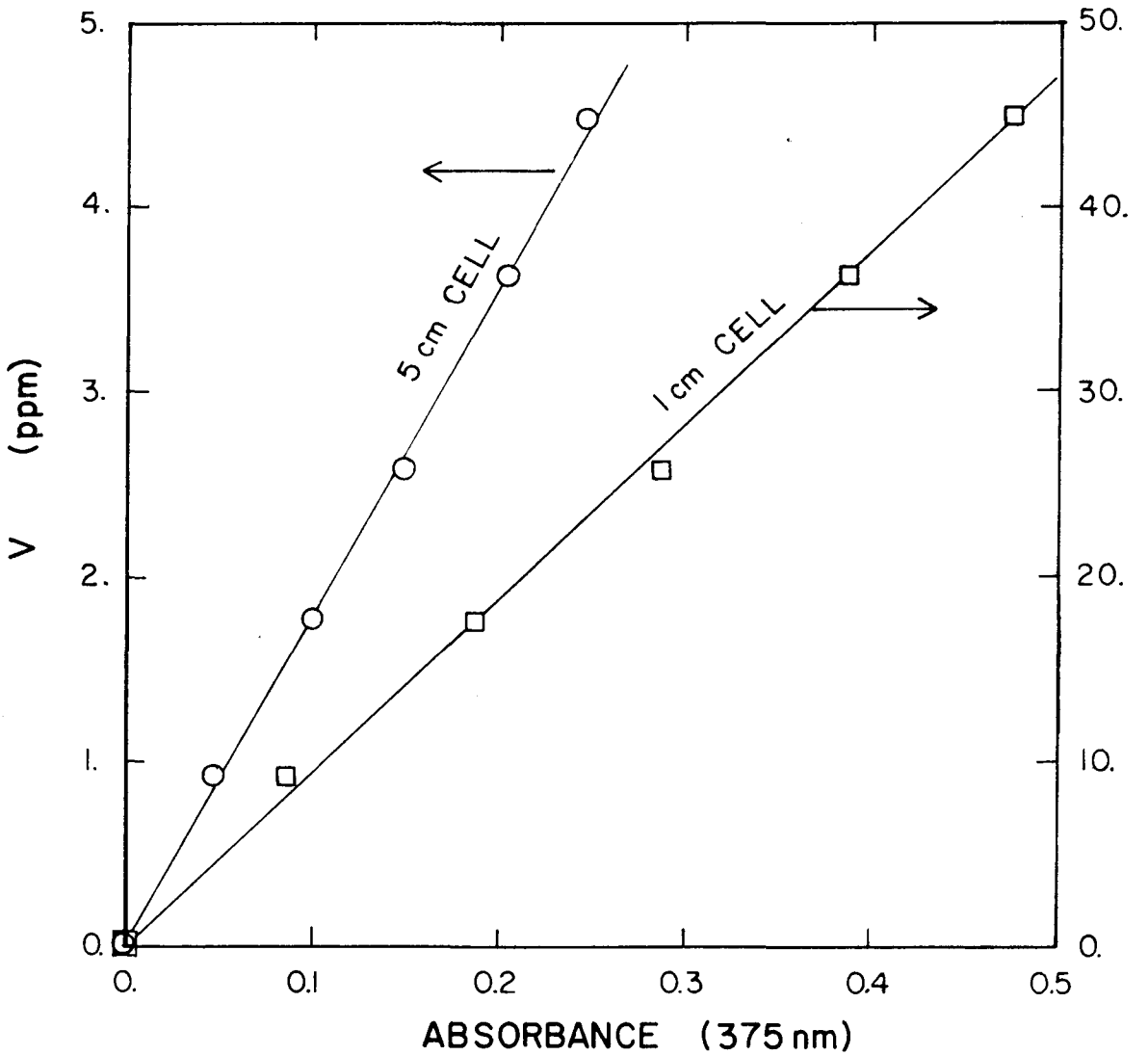

Figure 4.10 Relationship between absorbance and total suspended volume for illite in artificial seawater.

Table 4.2 Total suspended volume (V), volume flux (E), and volume removal rate constant (b) during illite experiments at shear rates of 1/2,1, 2,4,8,16, and 32 sec^{-1}.

$G = 1/2\ sec^{-1}$

Time (min)	V (ppm)	E (ppm/sec)
20	88.	145. $x10^{-3}$
40	28.	14.7 $x10^{-3}$
60	17.1	5.5 $x10^{-3}$
90	11.1	2.3 $x10^{-3}$
130	7.4	1.02 $x10^{-3}$
180	5.0	0.47 $x10^{-3}$

$b = 1.87\ x10^{-5}\ ppm^{-1}/sec$

$G = 1\ sec^{-1}$

Time (min)	V (ppm)	E (ppm/sec)
25	43.	52. $x10^{-3}$
45	19.0	10.1 $x10^{-3}$
70	10.4	3.0 $x10^{-3}$
100	6.9	1.33 $x10^{-3}$
140	4.6	0.59 $x10^{-3}$

$b = 2.8\ x10^{-5}\ ppm^{-1}/sec$

$G = 2\ sec^{-1}$

Time (min)	V (ppm)	E (ppm/sec)
20	37.	44. x10
40	15.9	8.1 x10
65	8.7	2.4 x10
101	5.0	1.38 x10
150	2.8	0.43 x10

$$b = \begin{cases} 3.2\ x10^{-5}\ ppm^{-1}/sec & \leq 65\ min. \\ 5.5\ x10^{-5}\ ppm^{-1}/sec & > 65\ min. \end{cases}$$

$G = 4\ sec^{-1}$

Time (min)	V (ppm)	E (ppm/sec)
20	24.	31. x10
35	14.4	11.0 x10
55	6.5	2.2 x10
86	3.6	1.08 x10
120	2.2	0.40 x10

$$b = \begin{cases} 5.3\ x10^{-5}\ ppm^{-1}/sec & \leq 55\ min. \\ 8.3\ x10^{-5}\ ppm^{-1}/sec & > 55\ min. \end{cases}$$

Table 4.2 (continued) Illite

$G = 8\ sec^{-1}$				$G = 16\ sec^{-1}$			
Time (min)	V (ppm)	E (ppm/sec)		Time (min)	V (ppm)	E (ppm/sec)	
15	34.	83.	$x10^{-3}$	15	40.	48.	$x10^{-3}$
30	11.2	9.0	$x10^{-3}$	30	24.	17.3	$x10^{-3}$
50	5.2	1.95	$x10^{-3}$	45	12.7	4.8	$x10^{-3}$
70	3.6	0.93	$x10^{-3}$	65	9.9	2.9	$x10^{-3}$
100	2.5	0.45	$x10^{-3}$	90	6.3	1.19	$x10^{-3}$
$b = 7.2\ x10^{-5}\ ppm^{-1}/sec$				$b = 3.0\ x10^{-5}\ ppm^{-1}/sec$			

$G = 32\ sec^{-1}$		
Time (min)	V (ppm)	E (ppm/sec)
15	68.	0.
30	65.	0.
50	72.	0.
81	57.	0.
120	52.	0.

$b = 0.0$

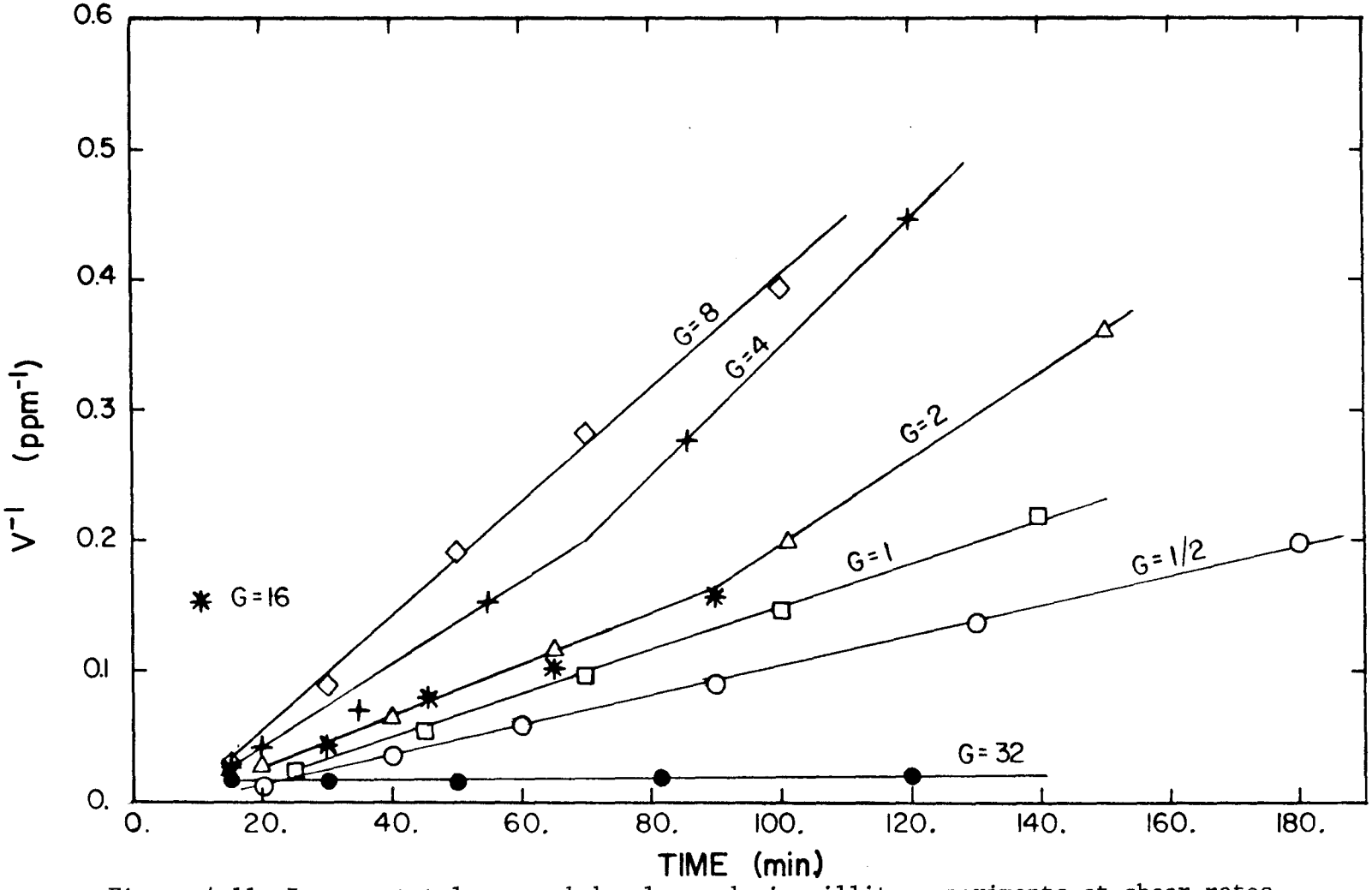

Figure 4.11 Inverse total suspended volumes during illite experiments at shear rates of 1/2,1,2,4,8,16, and 32 sec^{-1}.

closer to the surface gave an apparent increase in the removal rate. The effect of sample depth is illustrated in Figure 4.12 where samples were withdrawn 1 cm and 4 cm below the suspension surface in an experiment with illite at $G = 4\ sec^{-1}$. The two sets of data are nearly parallel with the 4 cm samples having a greater suspended volume than the 1 cm samples due to sedimentation from above. The effect observed in Figure 4.11 for $G = 2$ and $4\ sec^{-1}$ was the result of sampling closer to the surface, which caused an increase in the apparent removal rate. For the $G = 8\ sec^{-1}$ experimental data, only small sample volumes were removed at a fixed position and linearity was maintained.

Volume distributions and normalized volume distributions for the illite experiments at $G = 1/2$ to $16\ sec^{-1}$ are given in Figures 4.13 through 4.18, and volume distributions only for $G = 32\ sec^{-1}$ in Figure 4.19. Volume distributions were measured with a 30 μm aperture which again had the problem of larger aggregate breakup during counting. Multiple aperture sizing examples for one sample during experiments at $G = 1$ and $8\ sec^{-1}$ are included in Appendix B. No valid sizing information was obtained from the larger apertures at these shear rates. Volume distributions obtained at shear rates of 16 and $32\ sec^{-1}$ showed an increase in the region not dominated by particle breakup during counting, qualitatively indicating an increase in aggregate strength.

The volume distributions for $G = 1/2$ through $8\ sec^{-1}$ were self-similar in shape and the spread was substantially reduced on normalization. Sampling was begun after the steady states were established, avoiding some of the problems encountered during the kaolinite

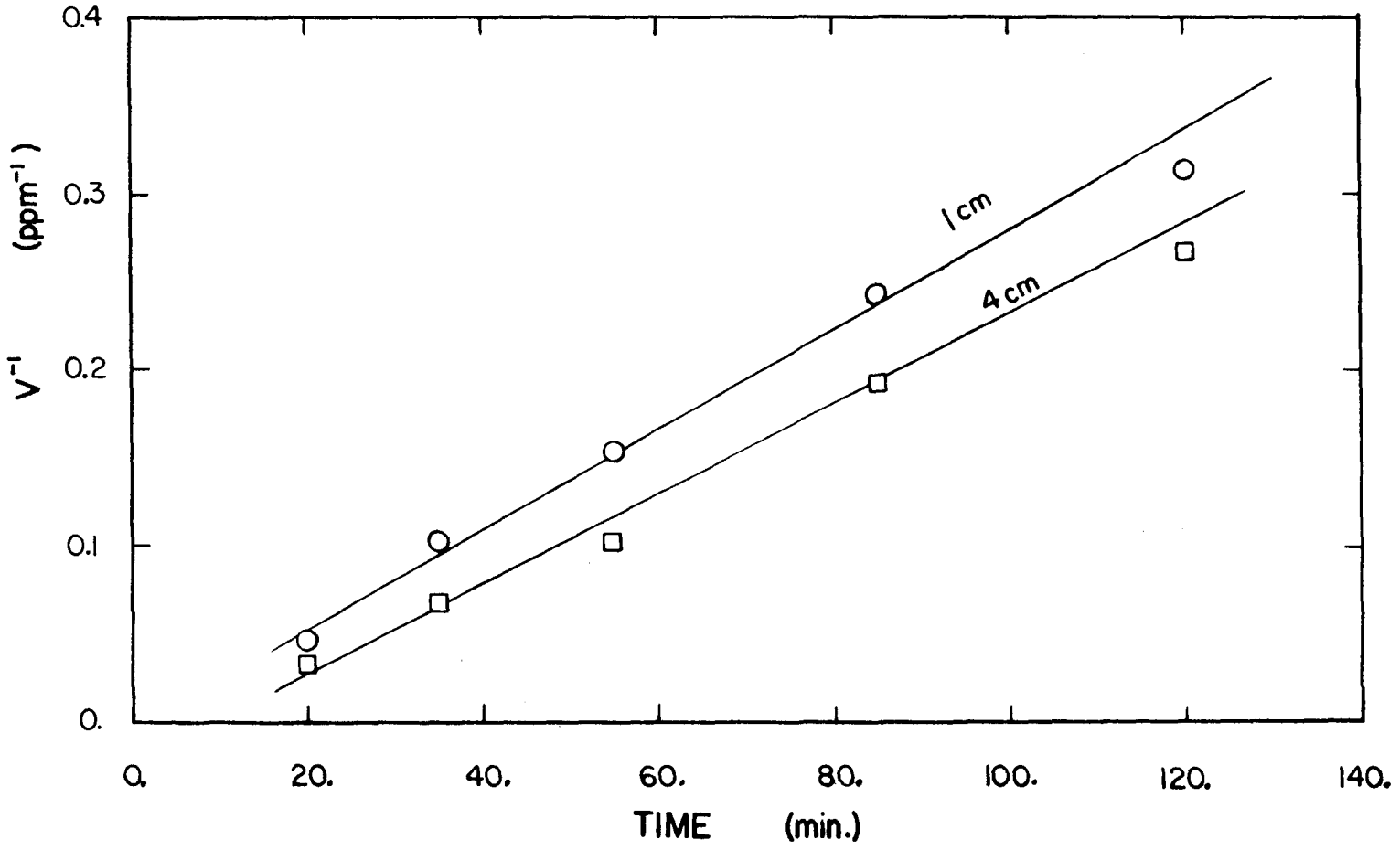

Figure 4.12 Inverse total suspended volumes during an illite experiment at G = 4 sec^{-1} with samples taken 1 cm and 4 cm below the suspension surface.

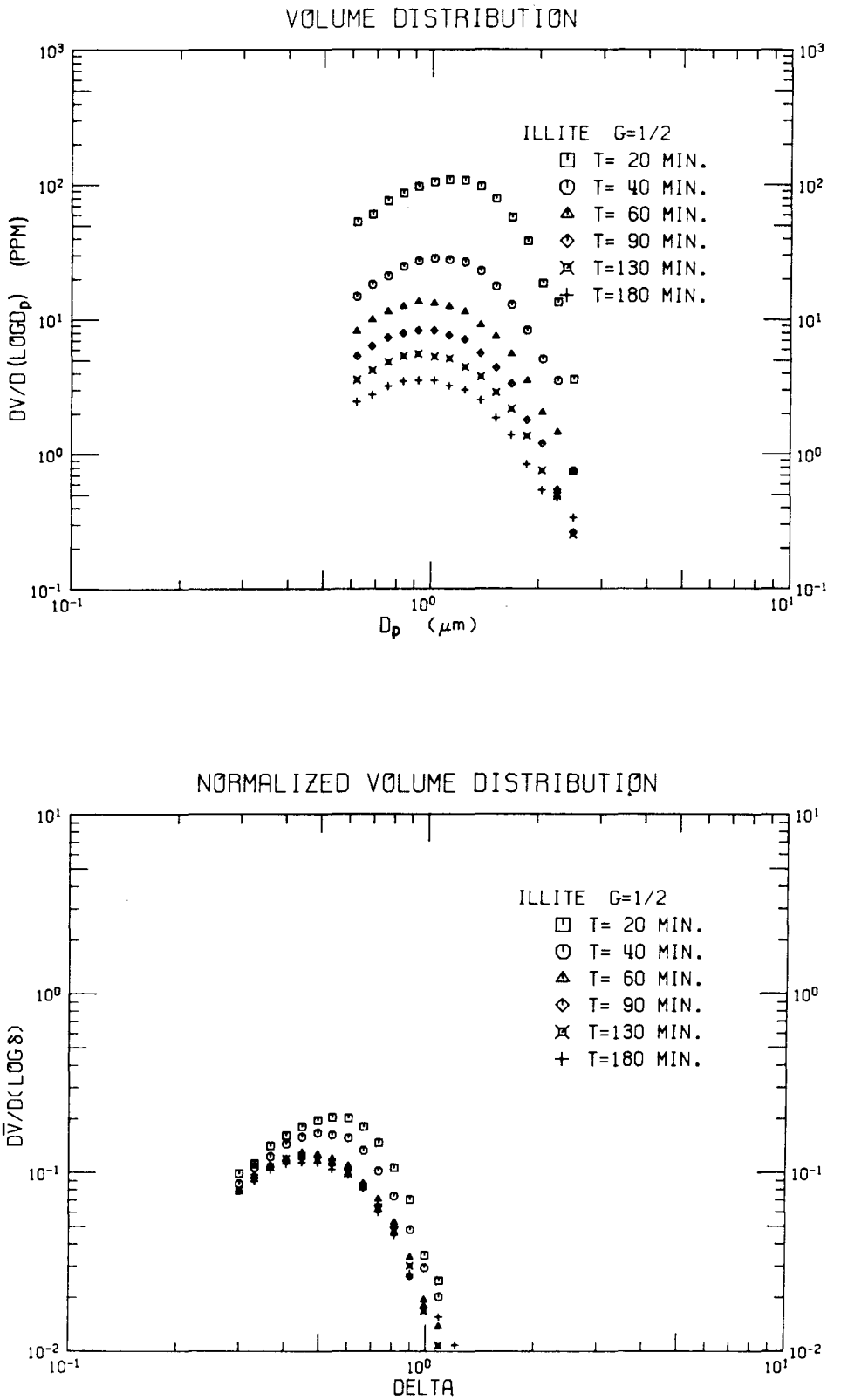

Figure 4.13 Volume distributions and normalized volume distributions for illite at $G = 1/2$ sec^{-1}.

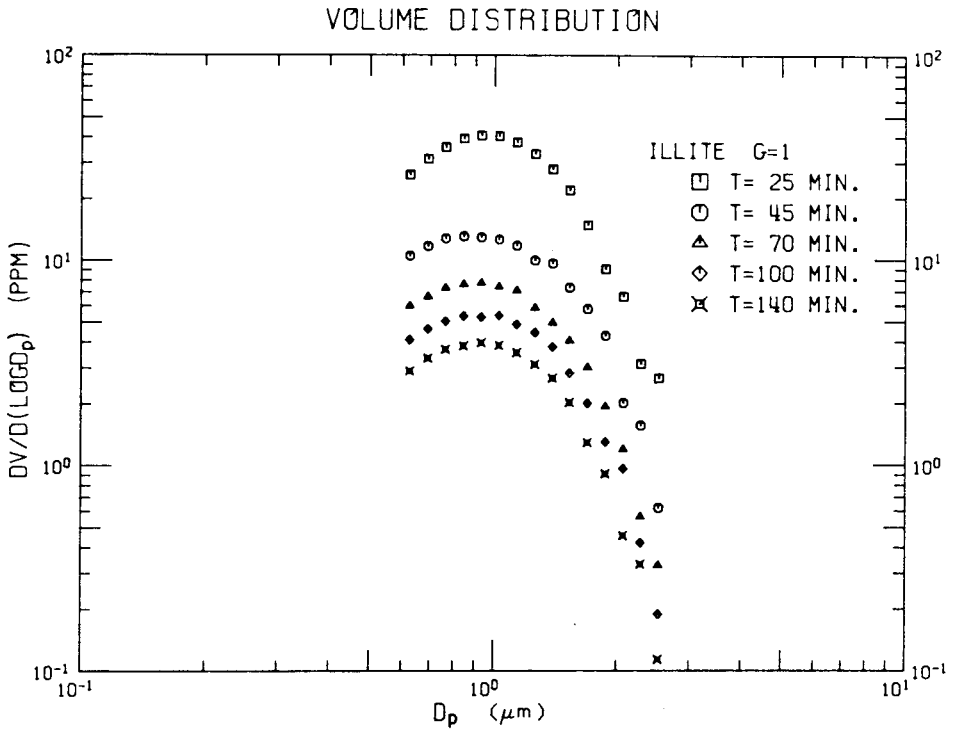

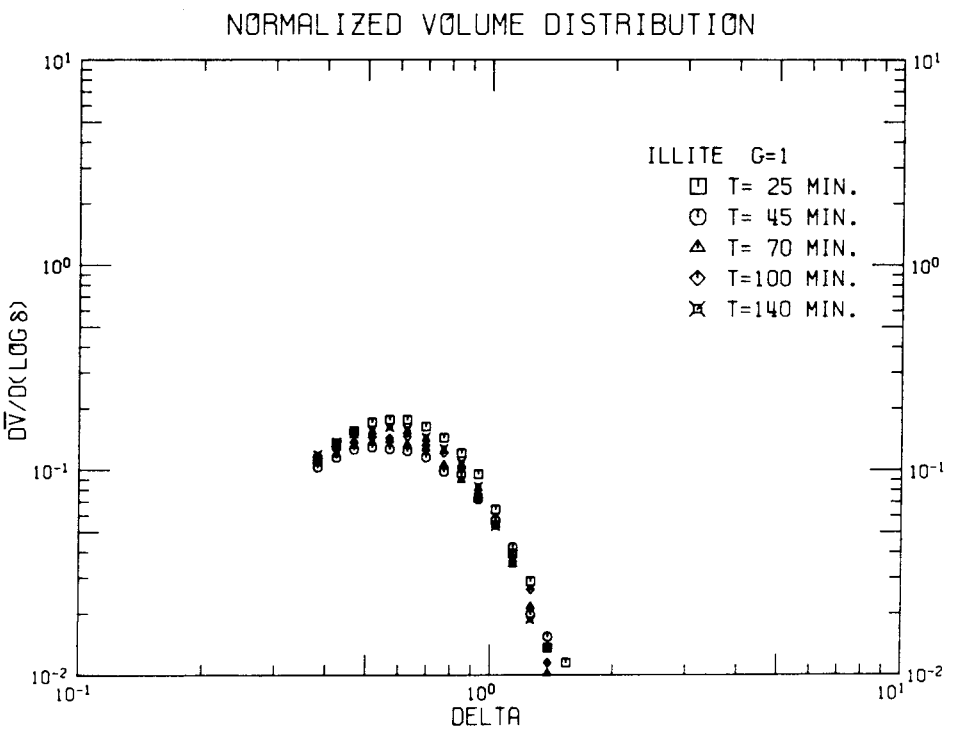

Figure 4.14 Volume distributions and normalized volume distributions for illite at $G = 1\ sec^{-1}$.

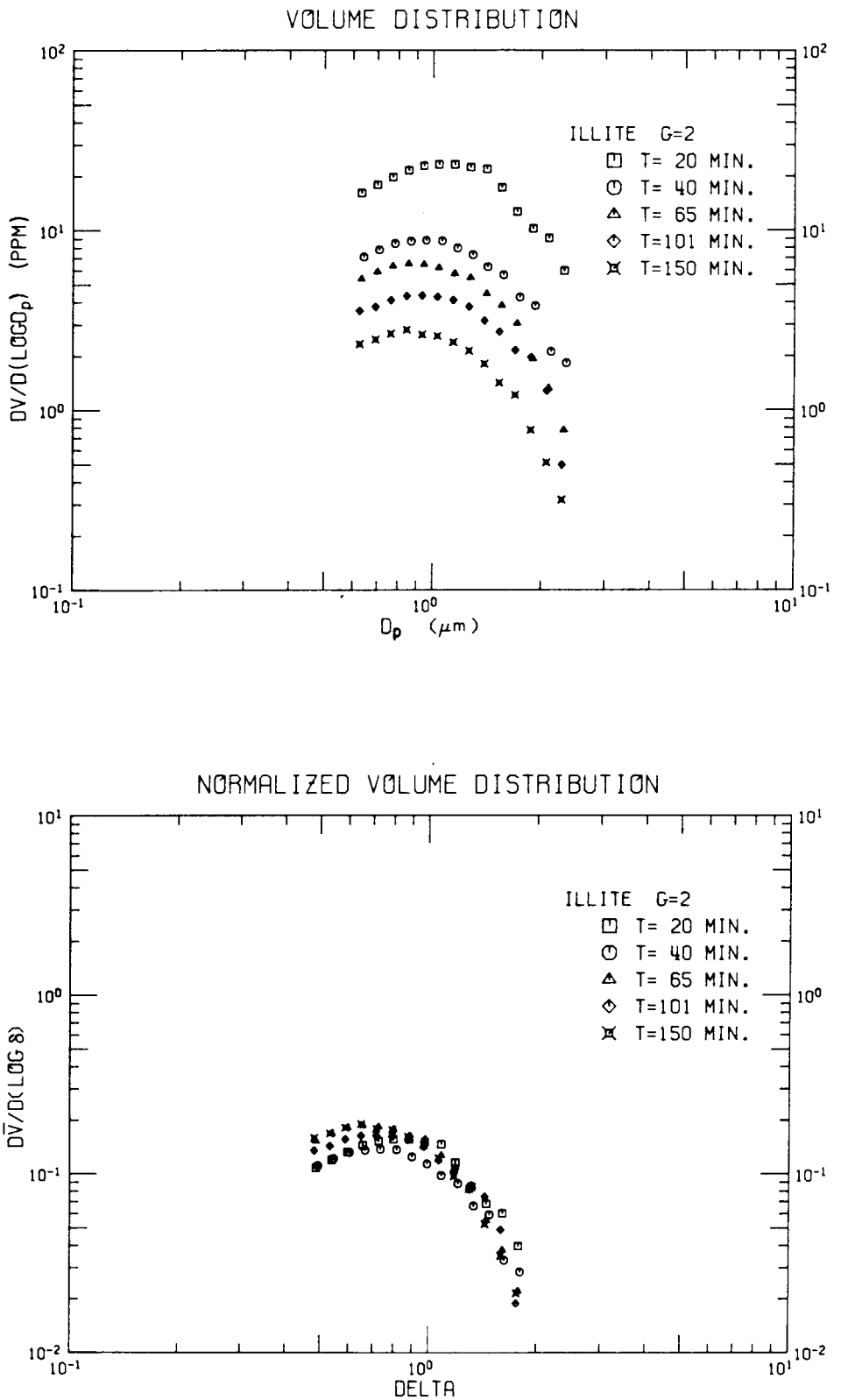

Figure 4.15 Volume distributions and normalized volume distributions for illite at $G = 2\ sec^{-1}$.

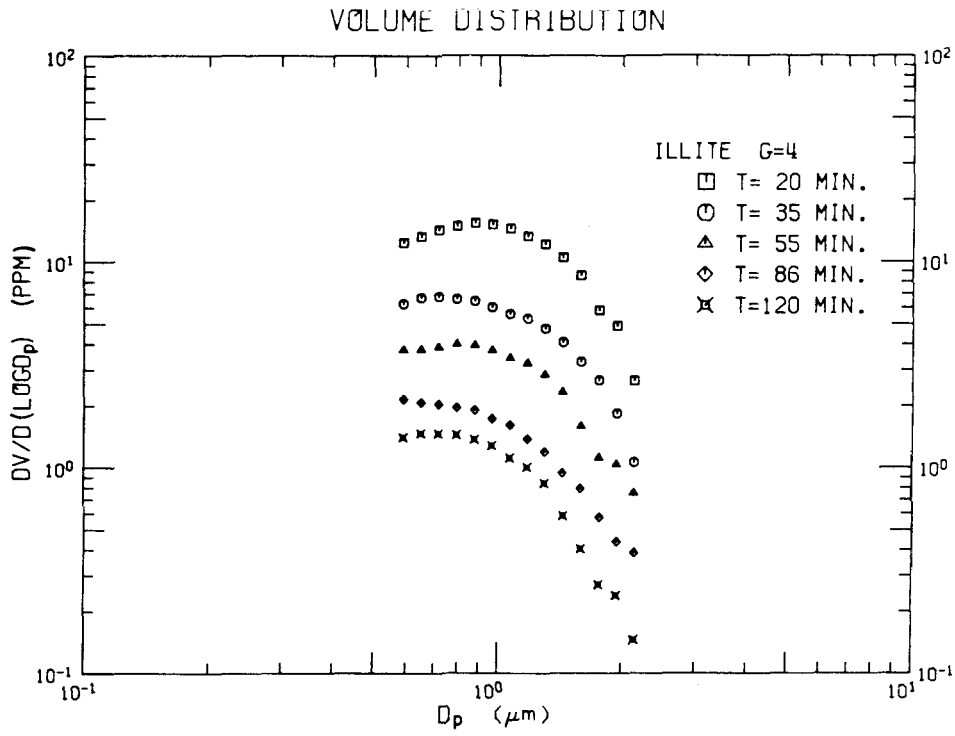

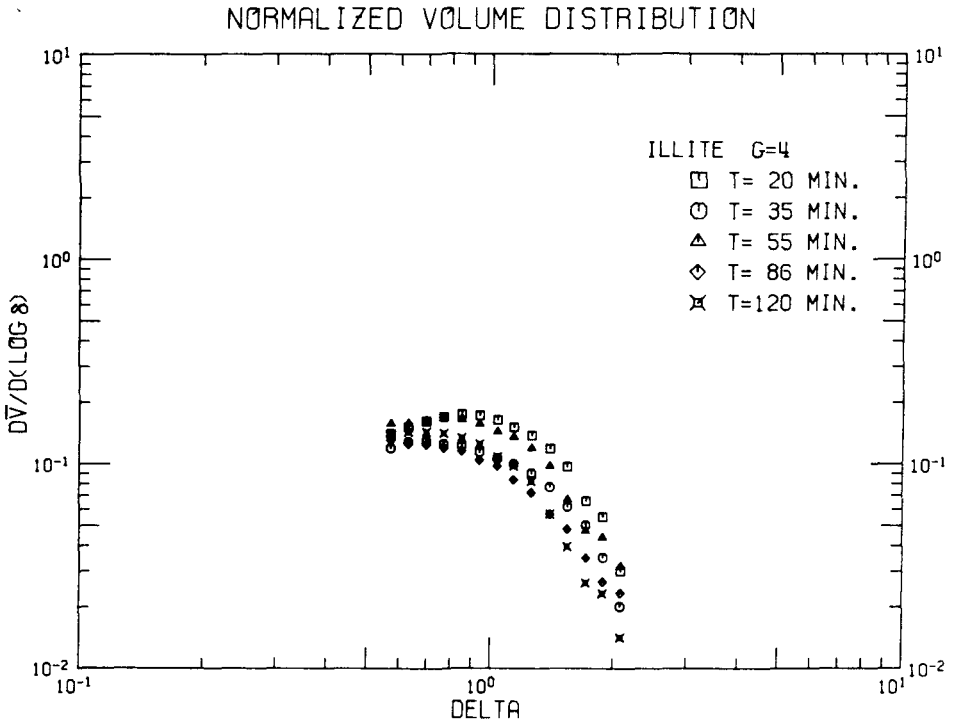

Figure 4.16 Volume distributions and normalized volume distributions for illite at G = 4 sec^{-1}.

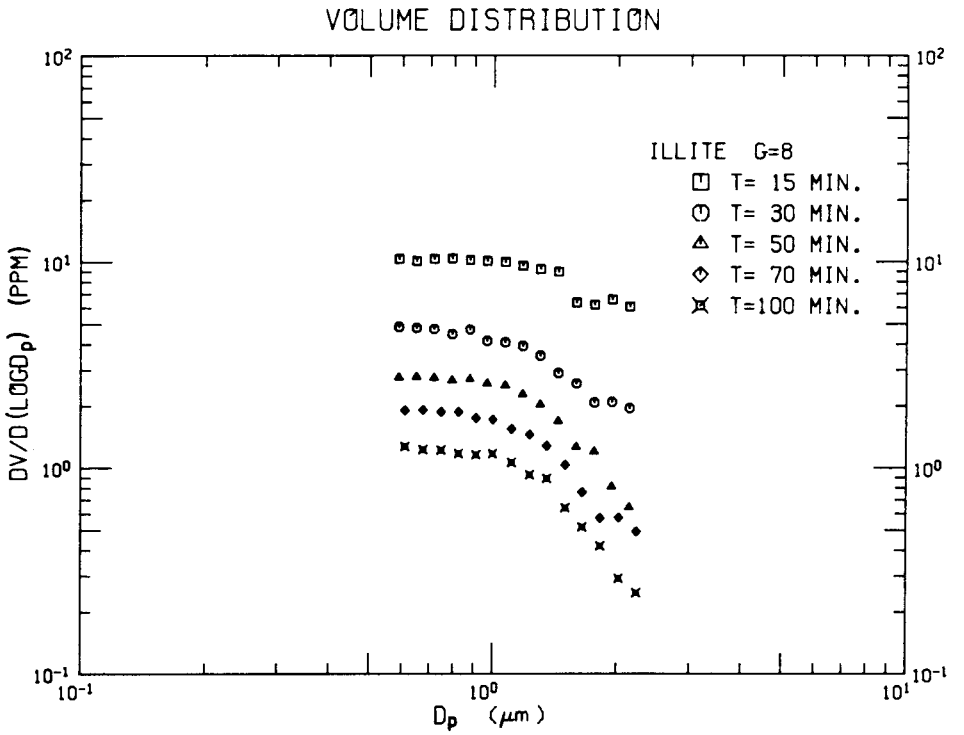

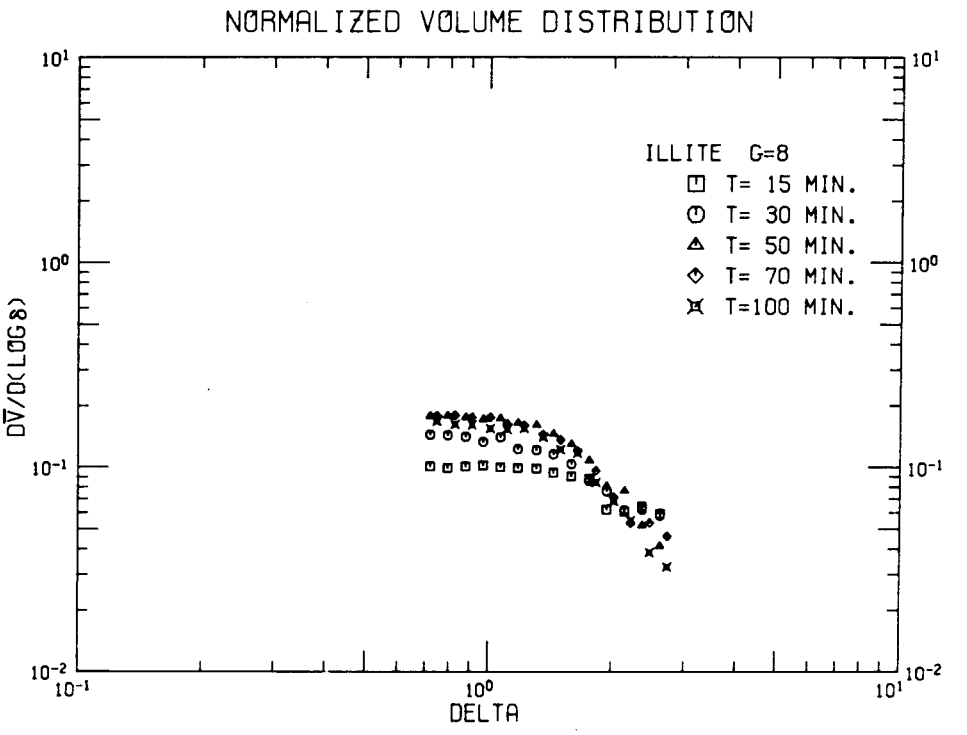

Figure 4.17 Volume distributions and normalized volume distributions for illite at G = 8 sec^{-1}.

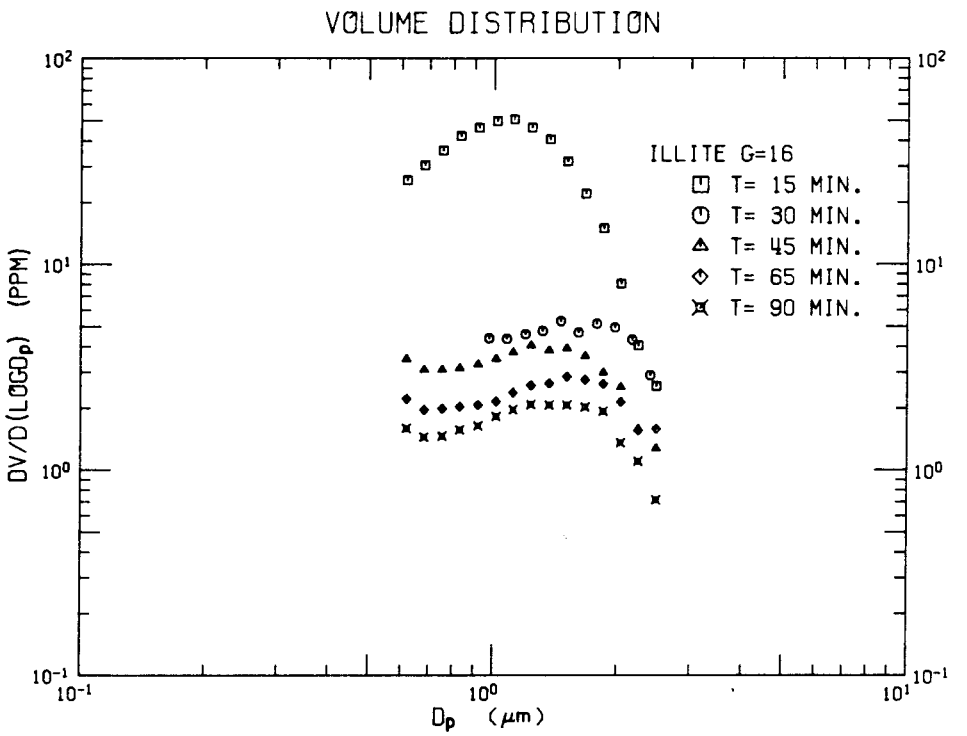

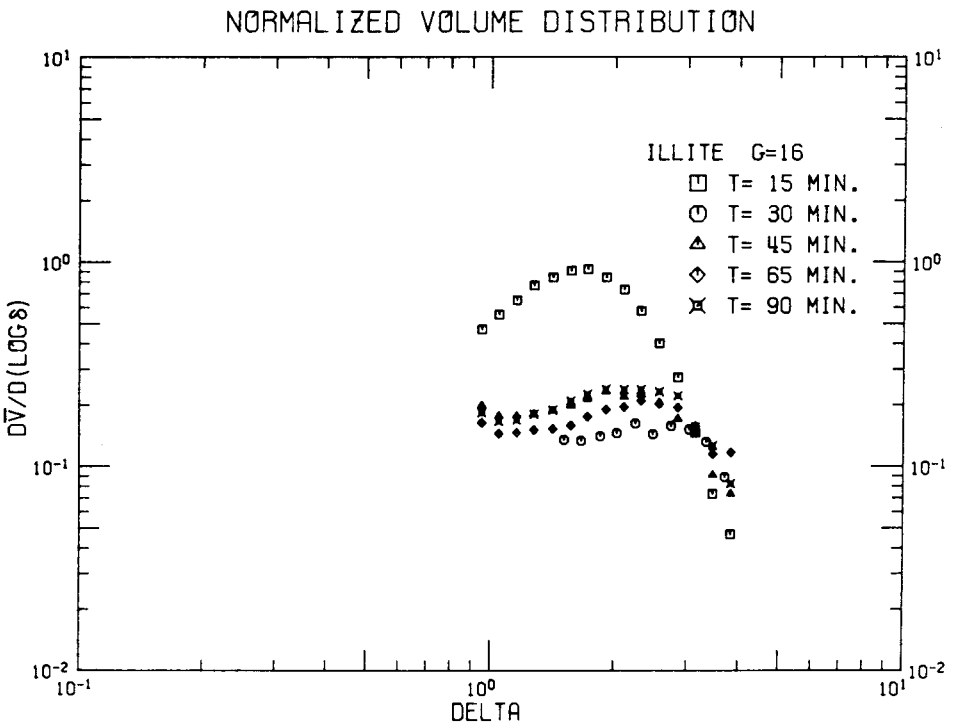

Figure 4.18 Volume distributions and normalized volume distributions for illite at $G = 16\ sec^{-1}$.

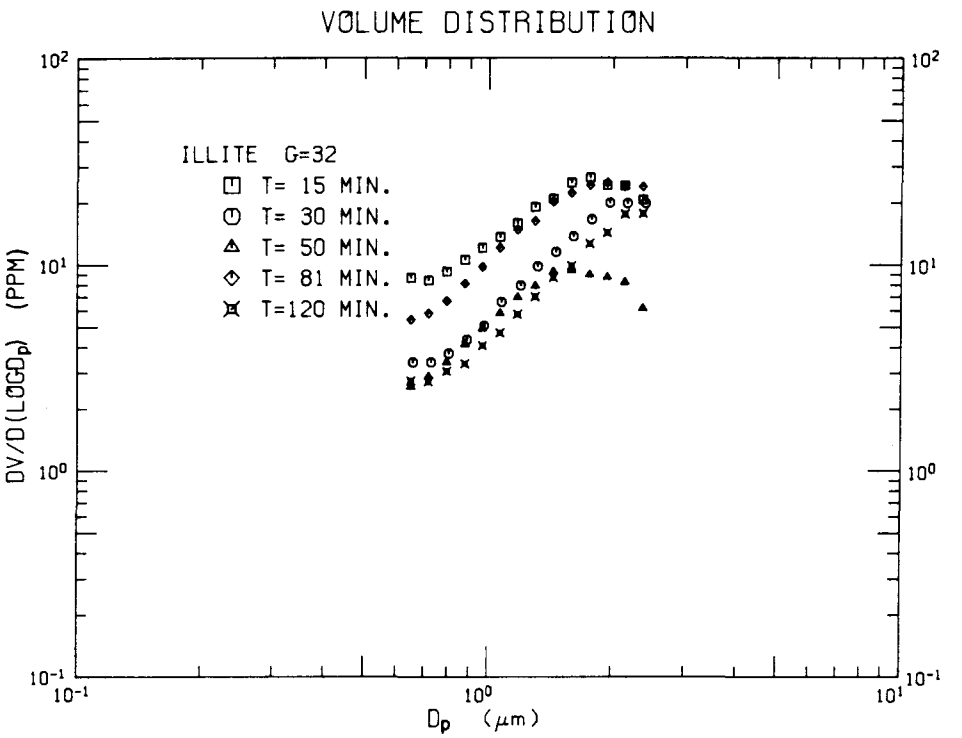

Figure 4.19 Volume distributions for illite at $G = 32\ sec^{-1}$.

experiments. At $G = 16\ sec^{-1}$ the sample for 15 minutes was totally at variance with the other samples at this shear rate, and probably represented an accidental analysis of a sample from a $G = 1/2\ sec^{-1}$ experiment. The remaining samples at $G = 16\ sec^{-1}$ had an increasing volume distribution out to almost 2 μm, where breakup during counting became dominant. At $G = 32\ sec^{-1}$ steeper volume distributions were observed out to diameters greater than 2 μm, but because the total suspended volume did not decrease over time, normalization was not possible.

Figure 4.20 contains all normalized volume distributions, except for the intervals dominated by breakup during counting and the 15 minute sample at $G = 16\ sec^{-1}$. The data for shear rates from 1/2 to 8 sec^{-1} followed one curve described by the Brownian and shear predictions. The normalized volume distributions for $G = 16\ sec^{-1}$ were slightly above the curve, indicating possible importance of other mechanisms. Unlike the kaolinite data, which had a split between Brownian and shear dominance at about $\delta = 1$, illite has a shift in dominance occurring at about $\delta = 0.5$. A possible reason for this difference is discussed in Section 4.5. From the normalized plot, estimates of the dimensionless constants are possible with $A_b = 0.4$ and $A_{sh} = 0.12$. As with the experimental results for kaolinite, size distributions dominated by differential sedimentation coagulation and gravitational settling were not observed because of larger aggregate breakup during counting.

4.3 Montmorillonite Experiments

Experiments with sodium montmorillonite were more difficult than those with the other two clays, and only the shear coagulation prediction

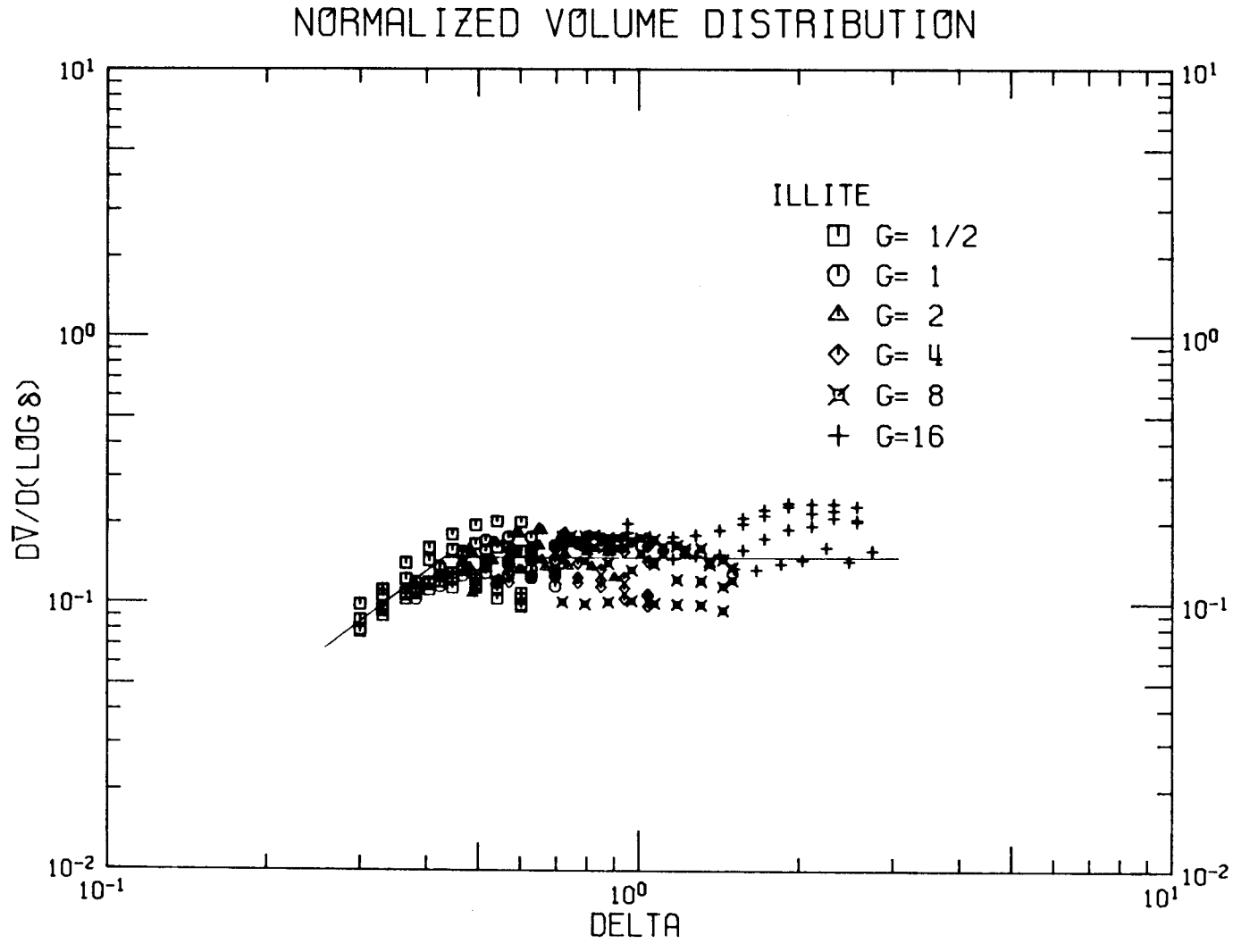

Figure 4.20 Normalized volume distributions for illite at G = 1/2,1,2,4,8, and 16 sec^{-1}.

was verified. The importance of a particle interaction mechanism other than coagulation and settling was observed at higher shear rates.

The plots of absorbance measured with 1 cm and 5 cm cells versus total suspended volume in Figure 4.21 are linear out to an absorbance of 1.3. The resulting linear regressions are

$$\text{1 cm cell} \quad V = -3.46 + 444.\ (\text{ABSORBANCE}) \quad r^2 = 0.9998 \qquad (4.7)$$

$$\text{5 cm cell} \quad V = 0.43 + 80.1\ (\text{ABSORBANCE}) \quad r^2 = 0.998\ . \qquad (4.8)$$

Absorbance was measured at a wavelength of 375 nm and a solid density of 2.5 g/cm^3 was assumed. One of the experimental difficulties encountered with montmorillonite was the low absorbance per part per million of suspension volume, which required the use of the 5 cm cell for all absorbance measurements. Montmorillonite suspension absorbance was low probably because of the small size of the individual particles, which are less efficient at light scattering.

The measured total suspended volumes and removal rate constants, and the calculated volume fluxes are summarized in Table 4.3 for experiments at shear rates of 1/2,1,2,4,8,16 and 32 sec^{-1}. At the start of each experiment the total suspended volume of montmorillonite was 51 ppm. Inverse volume plots in Figure 4.22 were linear over time, and the maximum rate of volume removal occurred at $G = 2\ sec^{-1}$. There was no suspended volume removal at a shear rate of 32 sec^{-1}. Because of the large sample volumes required for absorbance measurements, only four samples were withdrawn during a given experiment. Samples were withdrawn at a fixed position in the gap of the rotating cylinder apparatus which resulted in sampling at a decreasing distance below the surface. The first sample was withdrawn about 4 cm below the surface and the last sample at about 1 cm below the surface.

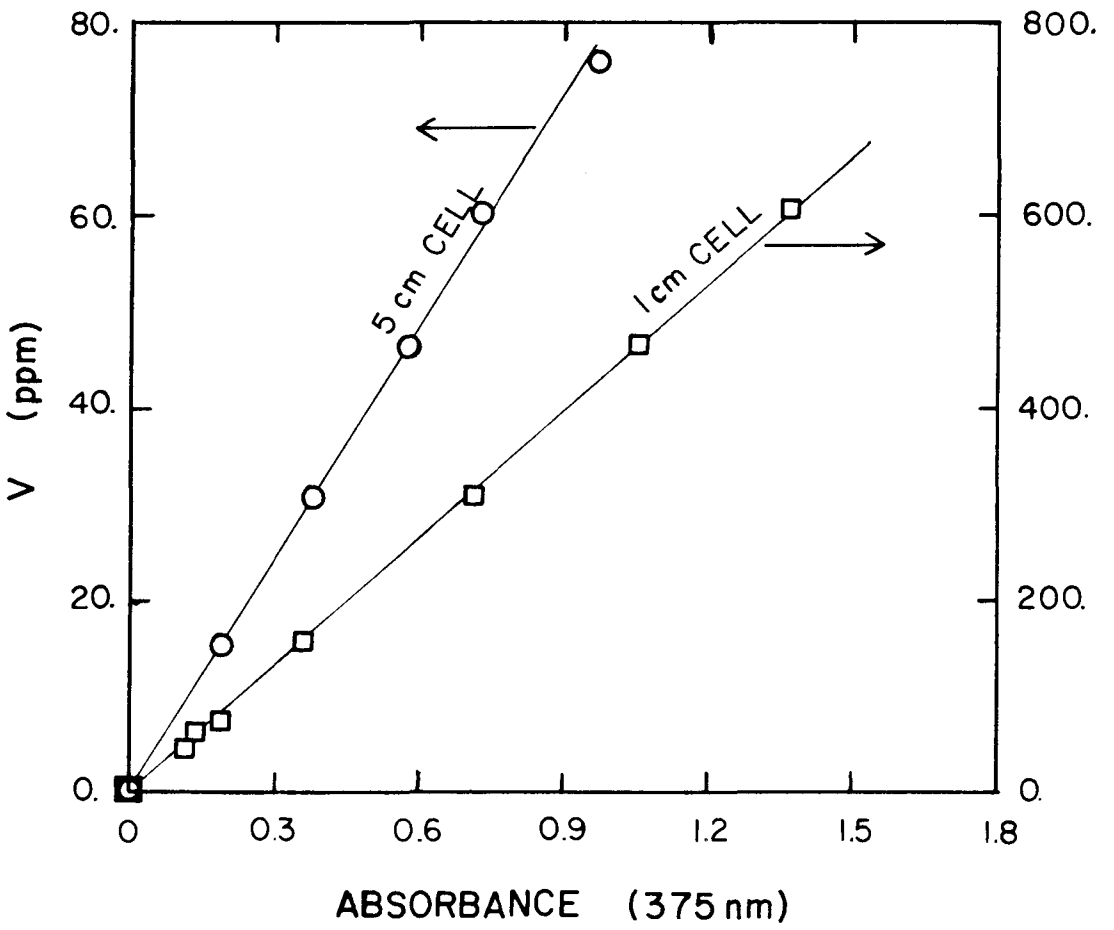

Figure 4.21 Relationship between absorbance and total suspended volume for montmorillonite in artificial seawater.

Table 4.3 Total suspended volume (V), volume flux (E), and volume removal rate constant (b) during montmorillonite experiments at shear rates of 1/2,1,2,4,8,16, and 32 sec^{-1}.

$G = 1/2\ sec^{-1}$		
Time (min)	V (ppm)	E (ppm/sec)
25	10.1	6.2×10^{-3}
50	5.5	1.85×10^{-3}
90	2.8	0.48×10^{-3}
150	1.87	0.21×10^{-3}

$b = 6.1 \times 10^{-5}\ ppm^{-1}/sec$

$G = 1\ sec^{-1}$		
Time (min)	V (ppm)	E (ppm/sec)
20	10.8	7.1×10^{-3}
40	5.5	1.85×10^{-3}
70	3.7	0.84×10^{-3}
120	2.3	0.32×10^{-3}

$b = 6.1 \times 10^{-5}\ ppm^{-1}/sec$

$G = 2\ sec^{-1}$		
Time (min)	V (ppm)	E (ppm/sec)
20	13.6	16.6×10^{-3}
35	4.8	2.1×10^{-3}
60	3.2	0.92×10^{-3}
90	1.95	0.34×10^{-3}

$b = 9.0 \times 10^{-5}\ ppm^{-1}/sec$

$G = 4\ sec^{-1}$		
Time (min)	V (ppm)	E (ppm/sec)
20	17.0	15.9×10^{-3}
30	10.8	6.4×10^{-3}
45	7.1	2.8×10^{-3}
65	6.1	--

$b = 5.5 \times 10^{-5}\ ppm^{-1}/sec$

Table 4.3 (continued)

$G = 8\ sec^{-1}$		
Time (min)	V (ppm)	E (ppm^{-1}/sec)
15	33.	$34. \times 10^{-3}$
25	25.	19.4×10^{-3}
40	14.3	6.3×10^{-3}
60	9.3	2.7×10^{-3}

$b = 3.1 \times 10^{-5}\ ppm^{-1}/sec$

$G = 16\ sec^{-1}$		
Time (min)	V (ppm)	E (ppm^{-1}/sec)
20	38.	$46. \times 10^{-3}$
40	17.2	9.5×10^{-3}
70	6.1	1.19×10^{-3}
110	5.0	0.80×10^{-3}

$b = 3.2 \times 10^{-5}\ ppm^{-1}/sec$

$G = 32\ sec^{-1}$		
Time (min)	V (ppm)	E (ppm/sec)
20	31.	--
40	29.	--
70	29.	--
110	38.	--

$b = 0.$

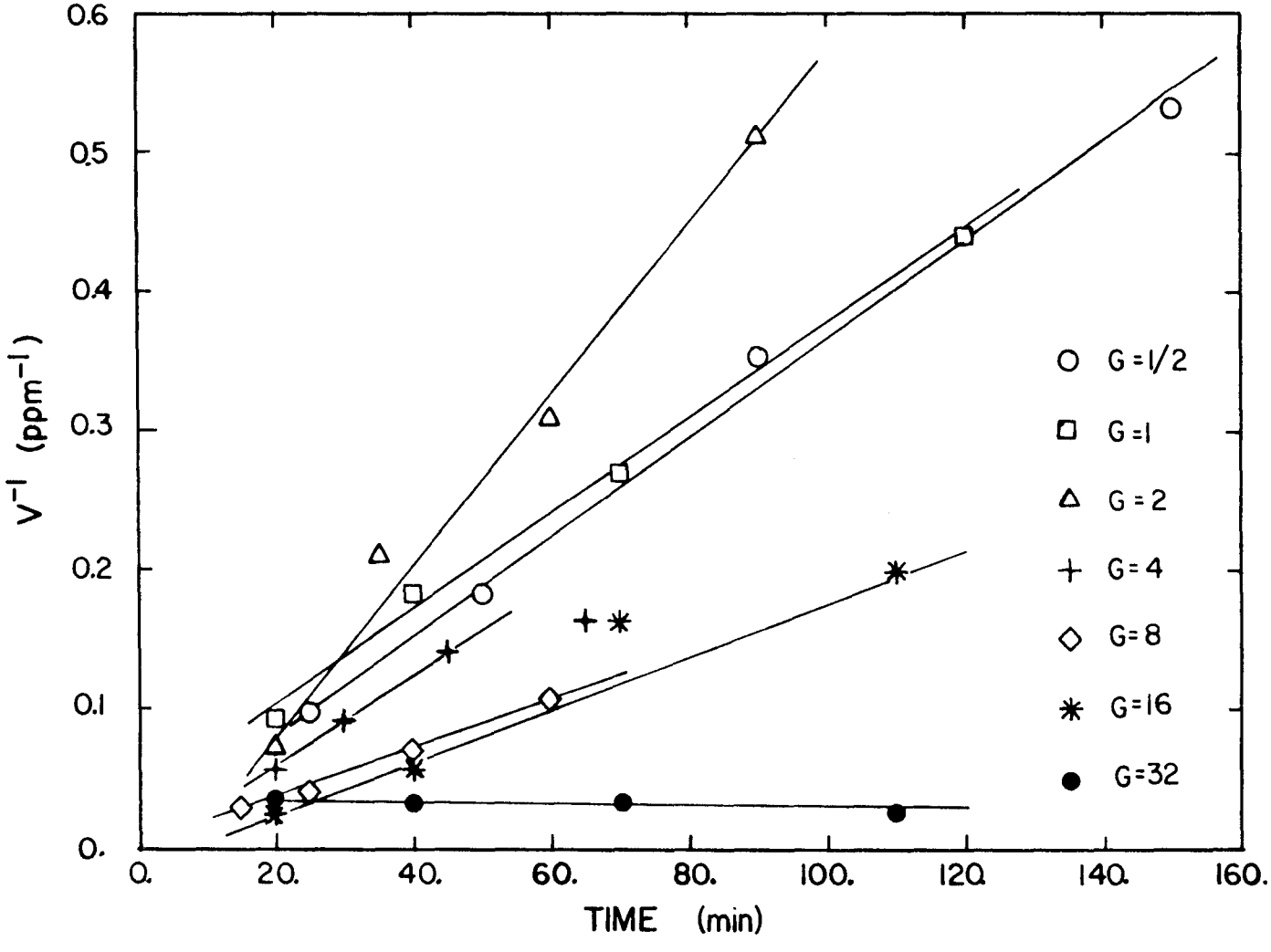

Figure 4.22 Inverse total suspended volumes during montmorillonite experiments at shear rates of 1/2,1,2,4,8,16, and 32 sec^{-1}.

Volume distributions and normalized volume distributions are plotted in Figures 4.23 through 4.28 for shear rates of 1/2 through 16 sec^{-1}. Figure 4.29 contains volume distributions at 32 sec^{-1}, which were not normalized because there was no decrease in total suspended volume. Only distributions collected with a 30 μm aperture are reported for shear rates of 1/2 through 8 sec^{-1}, while at G = 16 and 32 sec^{-1} data from 30, 70, 140, and 280 μm apertures were merged together, giving a broader distribution not dominated by aggregate breakup during counting. Two examples of multiple aperture sizing for montmorillonite are included in Appendix B. Volume distributions measured with 30, 70, and 140 μm apertures for one sample during the G = 1/2 sec^{-1} experiments had no regions of overlap between apertures as a result of weak aggregate structure. For one sample at G = 16 sec^{-1}, overlap regions were obtained with 30, 70, 140, and 280 μm apertures, indicating formation of stronger aggregates.

The volume distributions obtained for shear rates of 1/2, 1, and 2 sec^{-1} did not strictly establish a quasi-dynamic steady state, while higher shear rate volume distributions were self-similar in shape over time. The low shear rate data revealed volume distributions which increased at larger diameters in the early samples but decreased at larger diameters in later samples. On normalization of the low shear rate data, substantial reduction in spread was obtained. At 4, 8, and 16 sec^{-1}, volume distributions increased with increasing particle diameters accompanied by a decrease in total volume removal rate. There were two sample errors: at G = 4 sec^{-1} the sample obtained at 65 minutes was off the linear curve of Figure 4.22 and the 40 minute

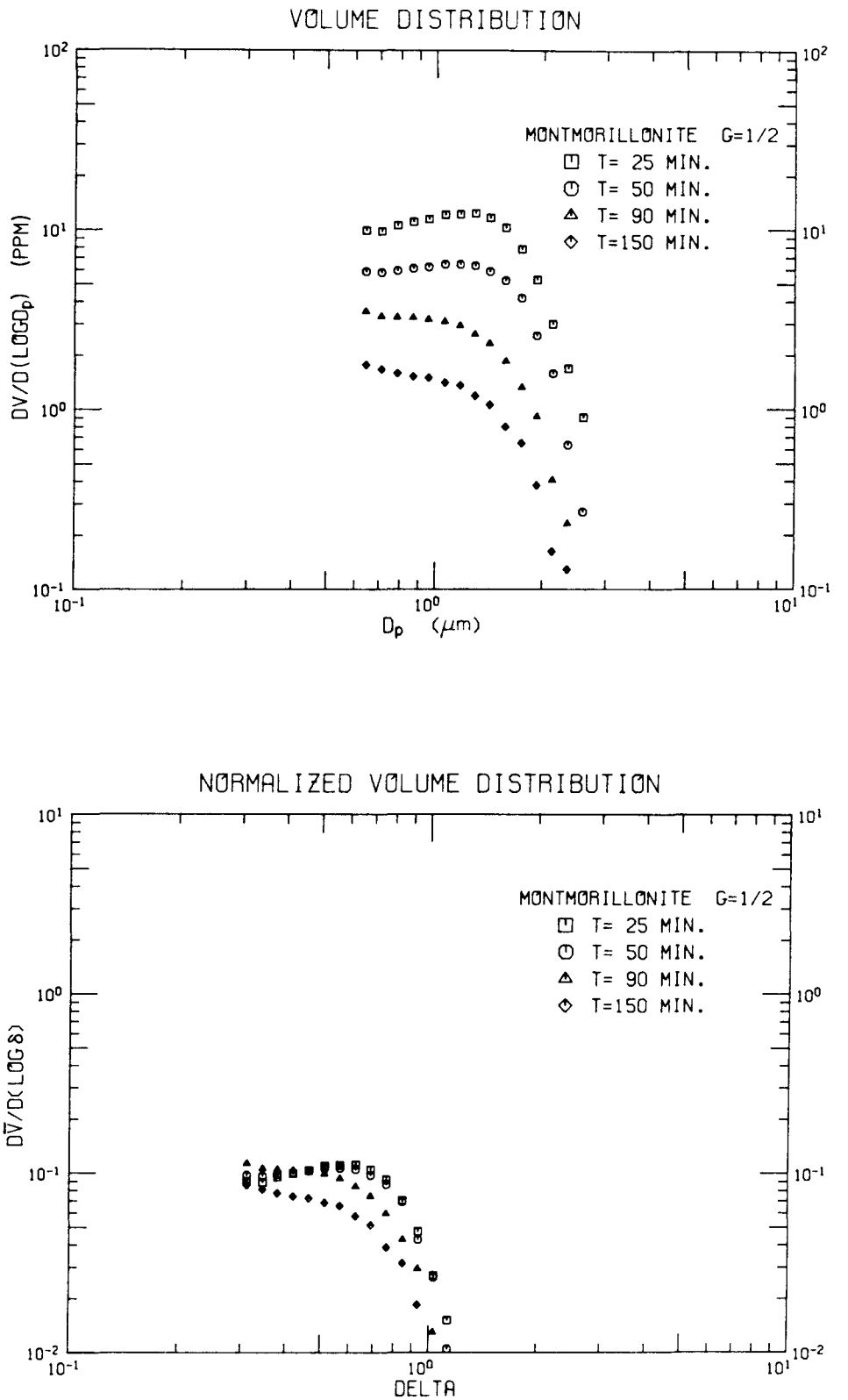

Figure 4.23 Volume distributions and normalized volume distributions for montmorillonite at $G = 1/2$ sec^{-1}.

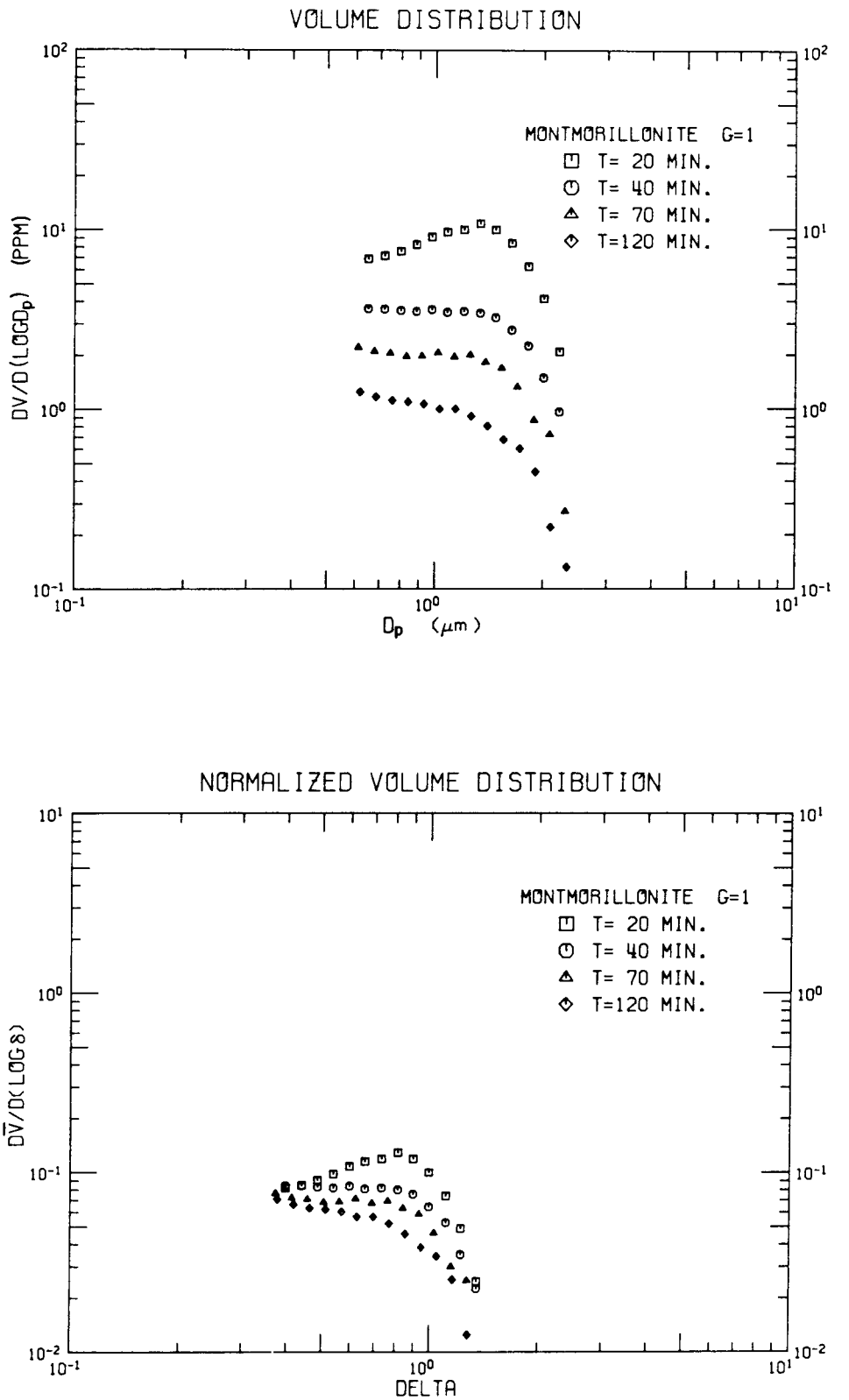

Figure 4.24 Volume distributions and normalized volume distributions for montmorillonite at $G = 1\ sec^{-1}$.

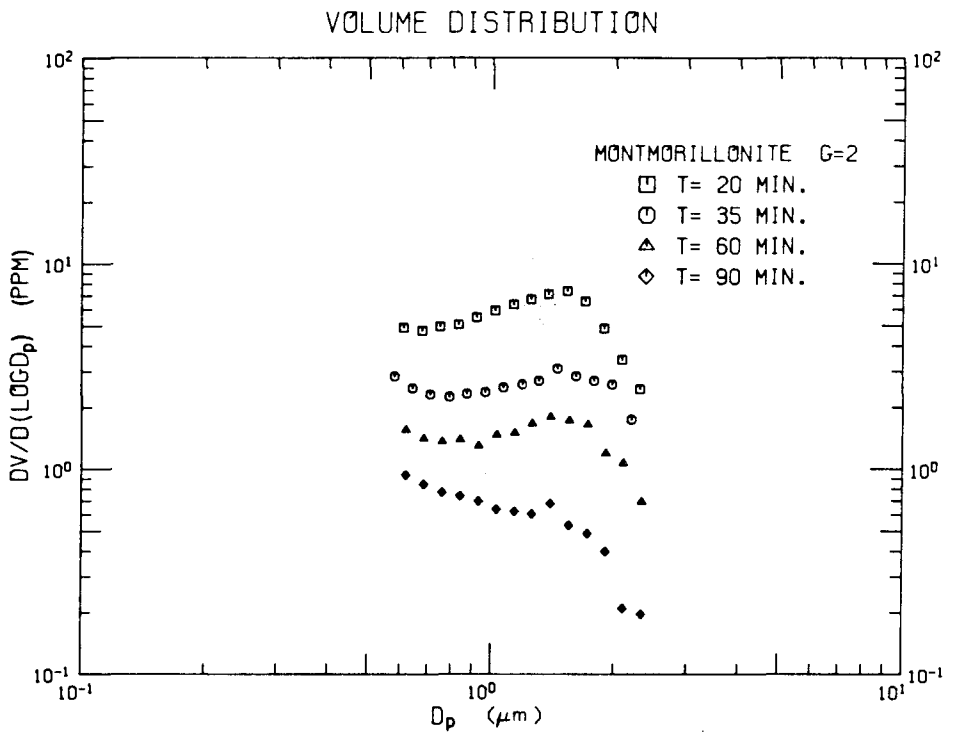

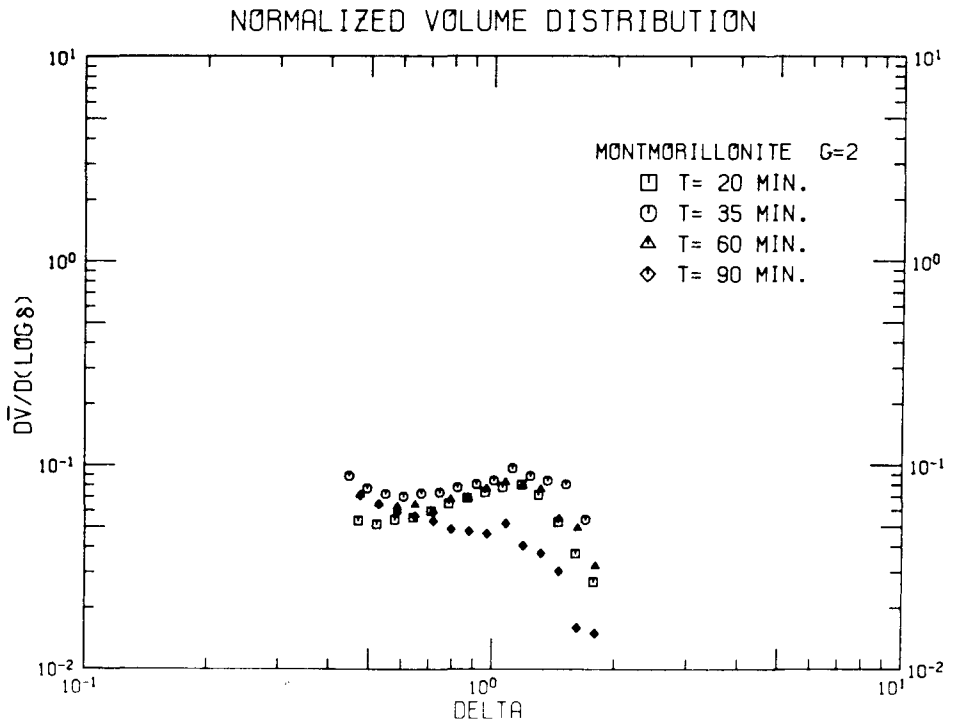

Figure 4.25 Volume distributions and normalized volume distributions for montmorillonite at $G = 2\ sec^{-1}$.

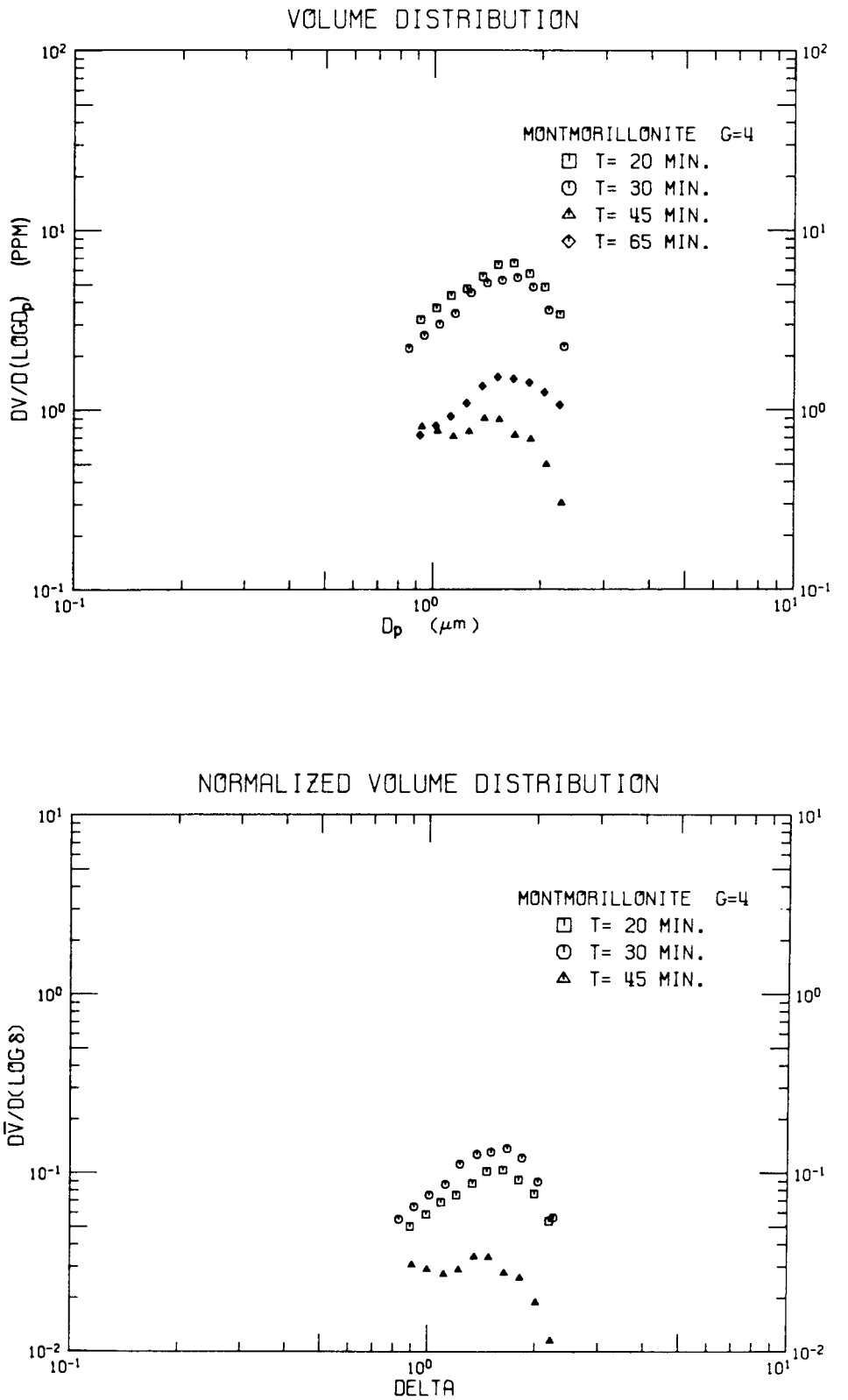

Figure 4.26 Volume distributions and normalized volume distributions for montmorillonite at $G = 4\ sec^{-1}$.

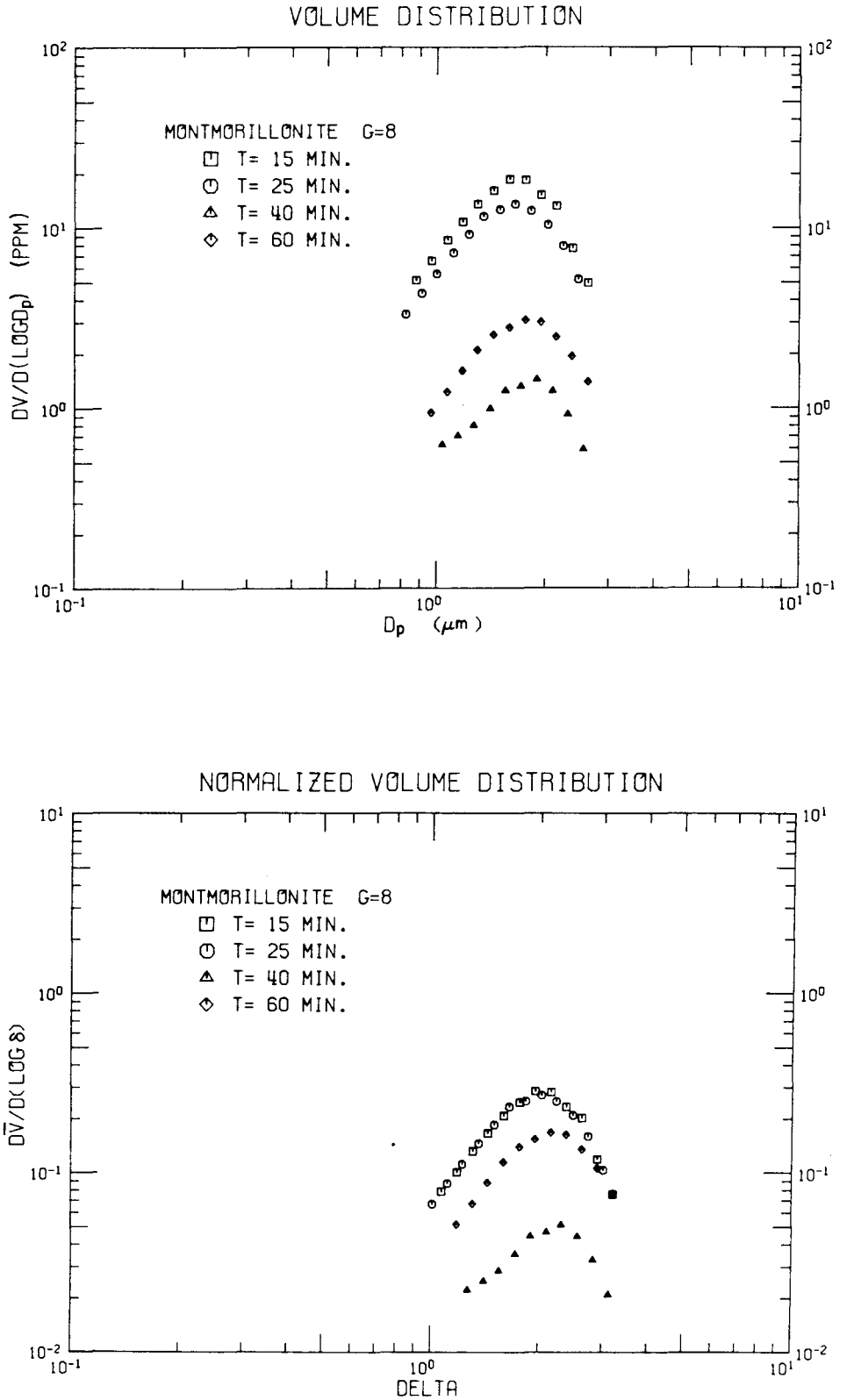

Figure 4.27 Volume distributions and normalized volume distributions for montmorillonite at $G = 8\ sec^{-1}$.

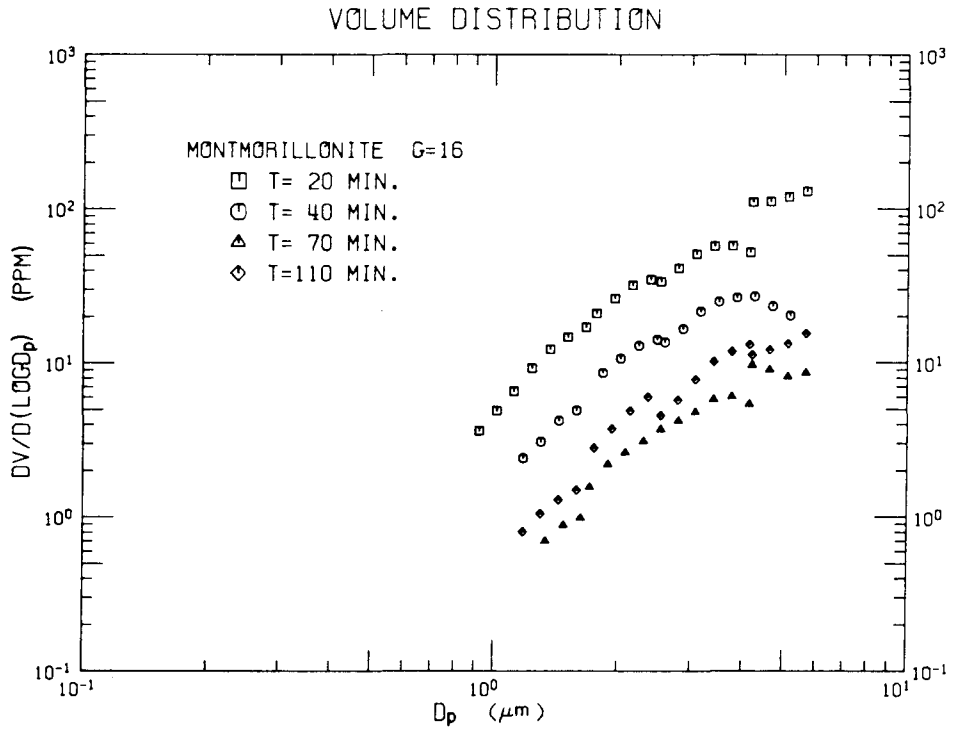

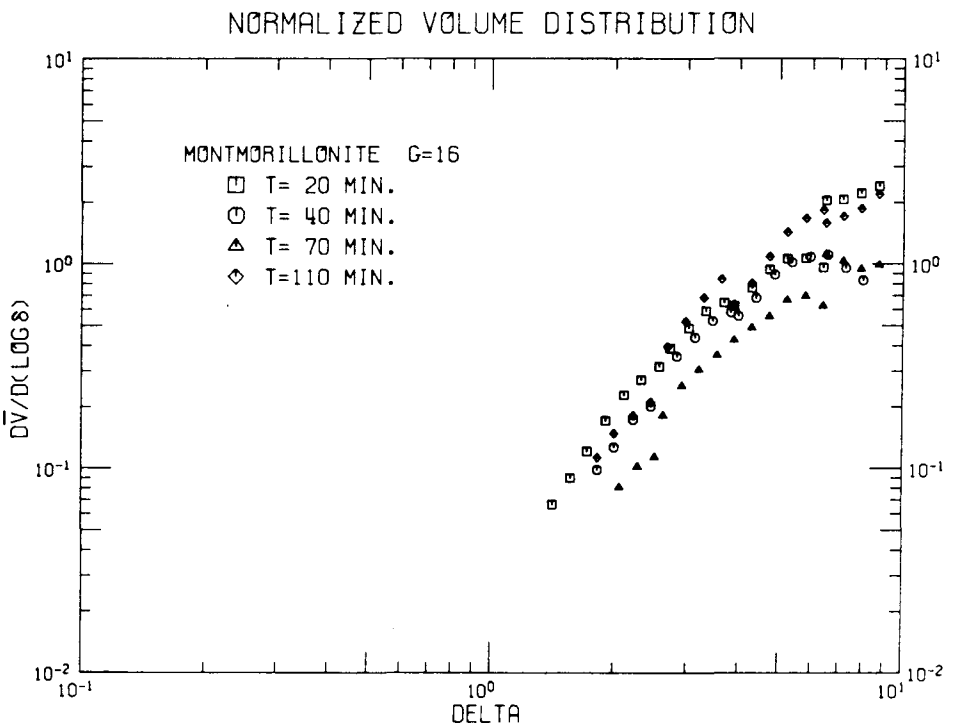

Figure 4.28 Volume distributions and normalized volume distributions for montmorillonite at $G = 16\ sec^{-1}$.

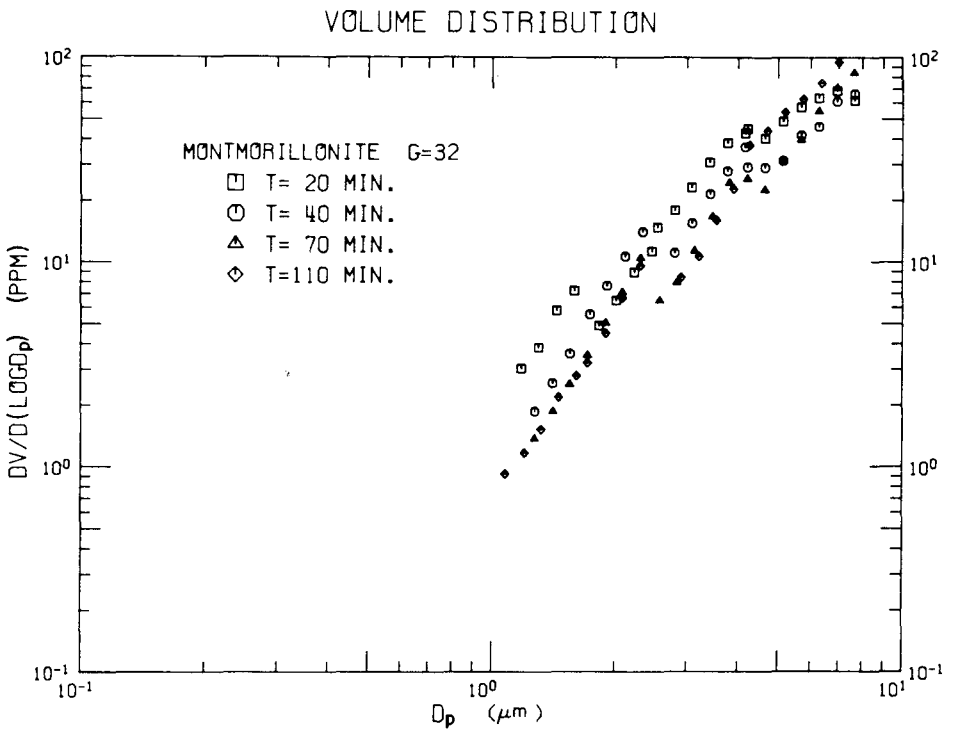

Figure 4.29 Volume distributions for montmorillonite at $G = 32\ sec^{-1}$.

sample at $G = 8\ sec^{-1}$ appeared below the distribution obtained at 60 minutes. Normalized plots at 4, 8, and 16 sec^{-1} were only fair to poor in agreement. At $G = 32\ sec^{-1}$ the volume distributions became steeper over time as particles coagulated into larger sizes which were not removed.

When all normalized data not dominated by breakup during counting are plotted in Figure 4.30, two regimes are discernible. For low shear rates up to 2 sec^{-1} the data approximately follow a level curve as predicted for shear coagulation, although occurring at $0.3 < \delta < 1.0$, where Brownian coagulation was expected to be dominant. For shear rates of 4 to 16 sec^{-1} a normalized volume distribution increasing with δ^2 was obtained, with considerable scatter. These higher shear rates correspond to decreasing removal rates, indicating the importance of a particle interaction mechanism other than coagulation and settling. From the initial level region the dimensionless shear coagulation constant was estimated to be 0.08. Section 4.5 discusses these results in terms of the porosity of the montmorillonite aggregate.

4.4 Silica Experiments

Experiments with cleaned silica in seawater found no size distributions in agreement with theoretical predictions for coagulation and settling.

The calibration data for silica suspension absorbance and total suspended volume are plotted in Figure 4.31. The linear regression lines relating absorbance at 375 nm to total suspended volume, assuming a solid density of 2.65 g/cm^3, were

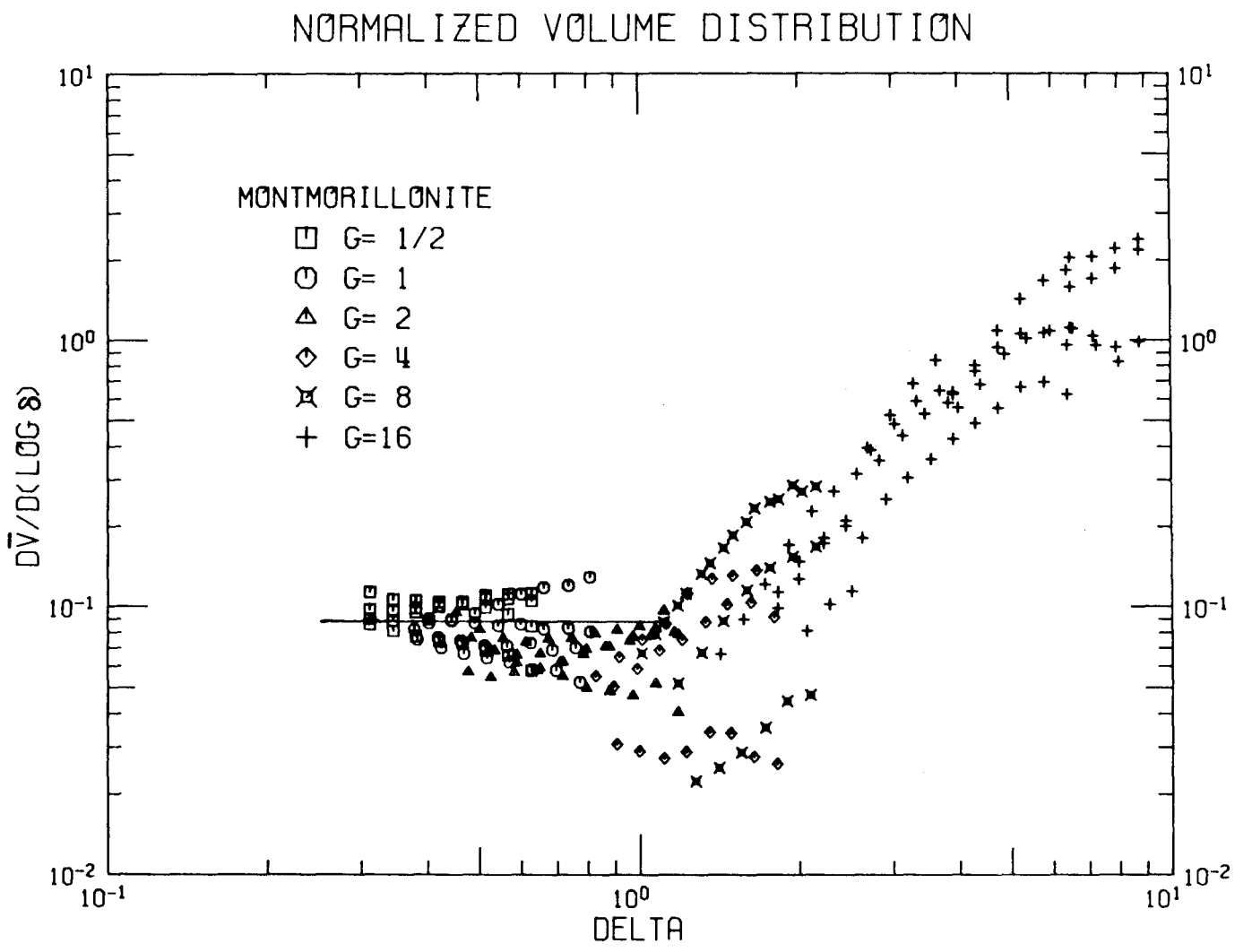

Figure 4.30 Normalized volume distributions for montmorillonite at G = 1/2,1,2,4,8, and 16 sec^{-1}.

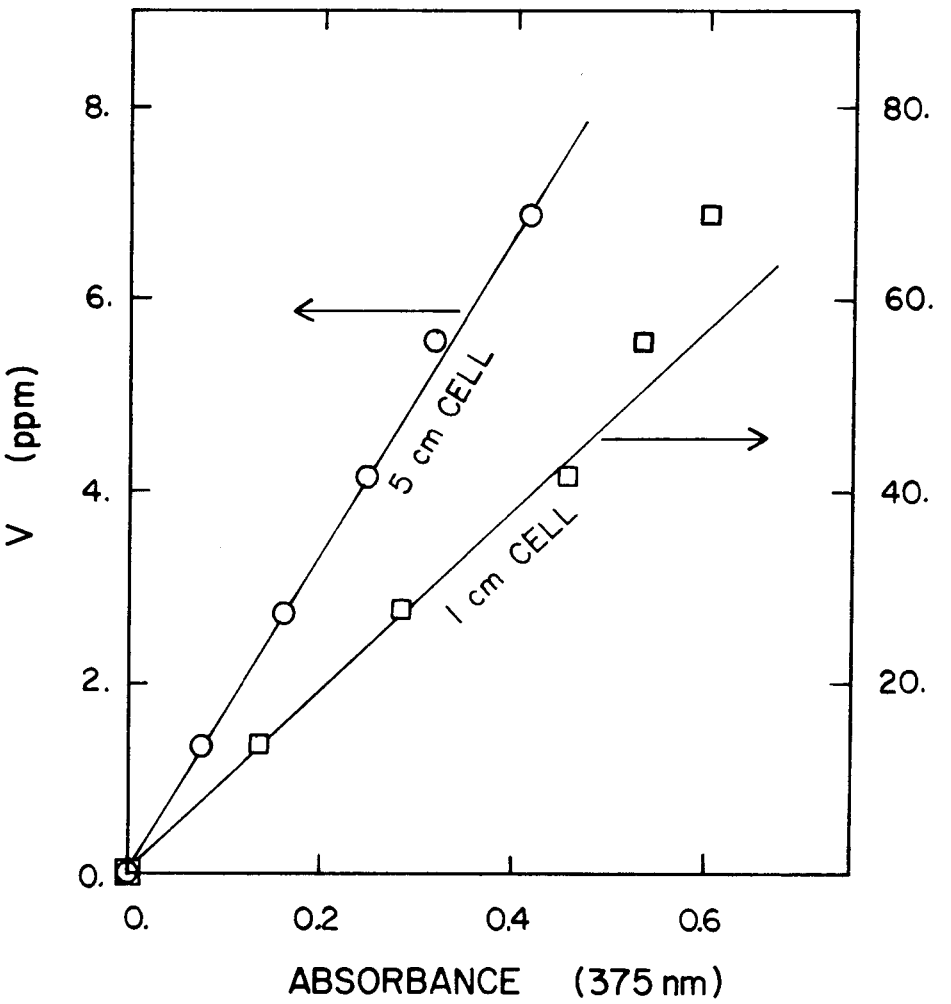

Figure 4.31 Relationship between absorbance and total suspended volume for silica in artificial seawater.

1 cm cell $V = 0.50 + 91.9$ (ABSORBANCE) $r^2 = 0.998$ (4.9)

5 cm cell $V = 0.03 + 16.8$ (ABSORBANCE) $r^2 = 0.998$. (4.10)

Linearity was observed for absorbance less than 0.5, and Equation (4.9) was based on the data for the origin and the first three points.

Suspended volumes, volume fluxes, and removal rate constants from slopes in Figure 4.32 are given in Table 4.4 for the silica experiments at shear rates of 1,2,4,8,16, and 32 sec^{-1}. At the start of each experiment the total suspended volume of silica was 49 ppm, slightly lower than for the early samples reported in Table 4.4. Four to seven samples were analyzed at each shear rate, and all the samples were removed from a depth one centimeter below the surface of the suspension. Only small volumes were removed for each sample because all absorbances were measured with the 1 cm cell. Figures 4.32 indicates that linearity in inverse total suspended volume over time was achieved after a lag time of 50 to 90 minutes. The maximum rate of suspended volume removal occurred at a shear rate of 4 sec^{-1}.

Figures 4.33 through 4.38 contain the volume and normalized volume distributions for silica in seawater at shear rates of 1,2,4, 8,16, and 32 sec^{-1}. The volume distributions were obtained with a 30 μm aperture, which could not size larger aggregates due to breakup during counting. The diameter at which breakup during counting dominated, increased with increasing shear rate, for example, at $G = 1\ sec^{-1}$ breakup dominated for $d_p > 1.5$ μm, and at $G = 16\ sec^{-1}$, $d_p > 2$ μm. This increase in aggregate strength was also evident from the multiple aperture sizing examples included in Appendix B for one

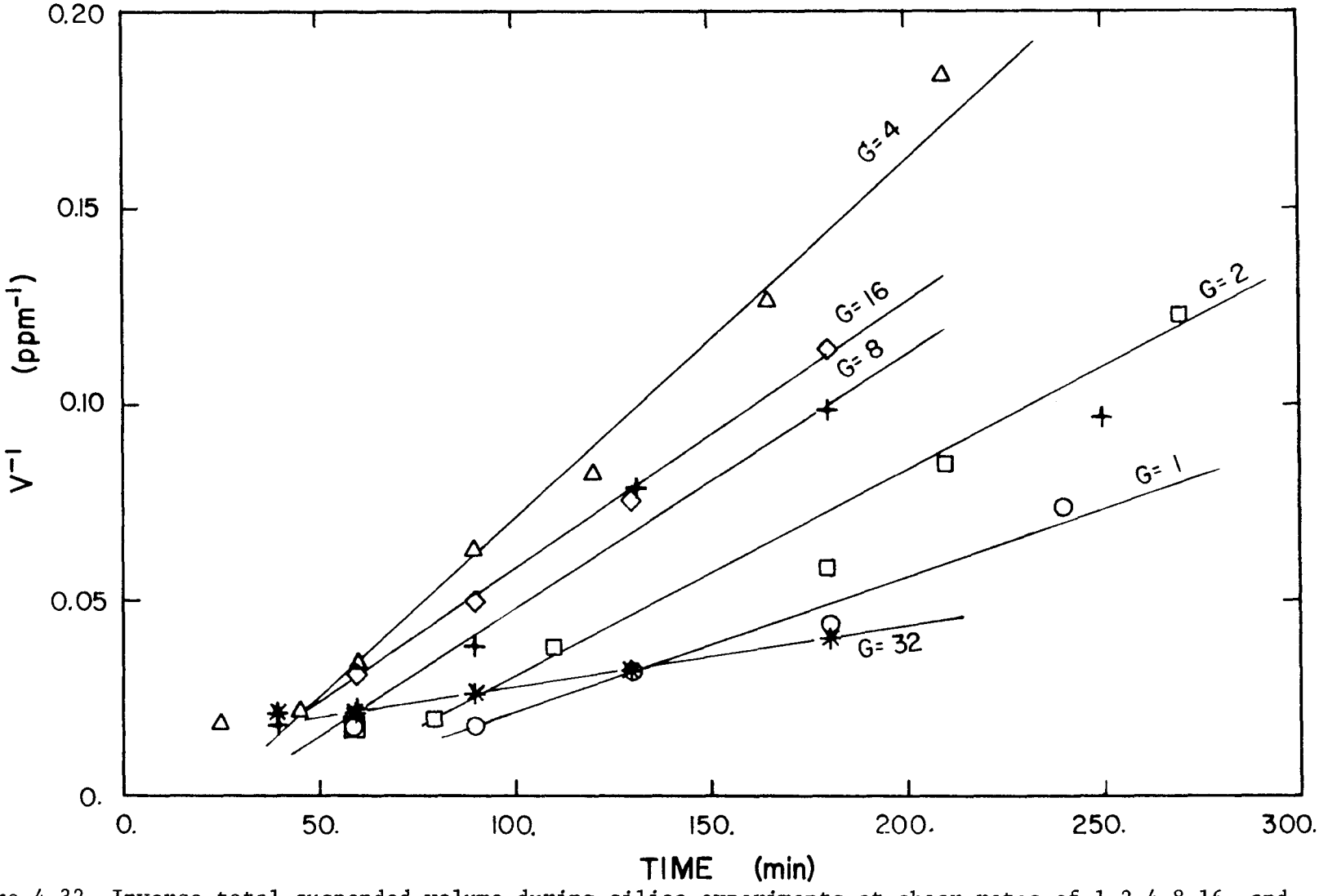

Figure 4.32 Inverse total suspended volume during silica experiments at shear rates of 1,2,4,8,16, and 32 sec^{-1}.

Table 4.4 Total suspended volume (V), volume flux (E), and volume removal rate constant (b) during silica experiments at shear rates of 1,2,4, 8,16, and 32 sec^{-1}.

$G = 1\ sec^{-1}$

Time (min)	V (ppm)	E (ppm/sec)
60	55.	--
90	52.	14.6 $x10^{-3}$
130	31.	5.2 $x10^{-3}$
180	23.	2.9 $x10^{-3}$
240	13.6	1.00 $x10^{-3}$

$b = 0.54\ x10^{-5}\ ppm^{-1}/sec$

$G = 2\ sec^{-1}$

Time (min)	V (ppm)	E (ppm/sec)
60	55.	--
80	49.	21. $x10^{-3}$
110	26.	5.9 $x10^{-3}$
180[a]	17.1	2.6 $x10^{-3}$
210	11.7	1.20 $x10^{-3}$
270	8.1	0.58 $x10^{-3}$

$b = 0.88\ x10^{-5}\ ppm^{-1}/sec$

[a]Size distribution was not measured for this sample.

$G = 4\ sec^{-1}$

Time (min)	V (ppm)	E (ppm/sec)
25	53.	--
45	45.	31. $x10^{-3}$
60	29.	13.0 $x10^{-3}$
90	15.5	3.7 $x10^{-3}$
120	12.2	2.3 $x10^{-3}$
165	7.9	0.96 $x10^{-3}$
210	5.4	0.45 $x10^{-3}$

$b = 1.54\ x10^{-5}\ ppm^{-1}/sec$

$G = 8\ sec^{-1}$

Time (min)	V (ppm)	E (ppm/sec)
40	53.	--
60	43.	21. $x10^{-3}$
90	25.	7.1 $x10^{-3}$
131	12.7	1.82 $x10^{-3}$
180	10.1	1.15 $x10^{-3}$
250	10.3	--

$b = 1.13\ x10^{-5}\ ppm^{-1}/sec$

Table 4.4 (continued)

$G = 16\ sec^{-1}$			$G = 32\ sec^{-1}$		
Time (min)	V (ppm)	E (ppm/sec)	Time (min)	V (ppm)	E (ppm/sec)
60	31.	$11.0\ x10^{-3}$	40	48.	--
90	20.	$4.6\ x10^{-3}$	60	46.	$5.5\ x10^{-3}$
130	13.1	$1.96\ x10^{-3}$	90	38.	$3.8\ x10^{-3}$
180	8.8	$0.88\ x10^{-3}$	130	31.	$2.5\ x10^{-3}$
			180	25.	$1.63\ x10^{-3}$
$b = 1.14\ x10^{-5}\ ppm^{-1}/sec$			$b = 0.26\ x10^{-5}\ ppm^{-1}/sec$		

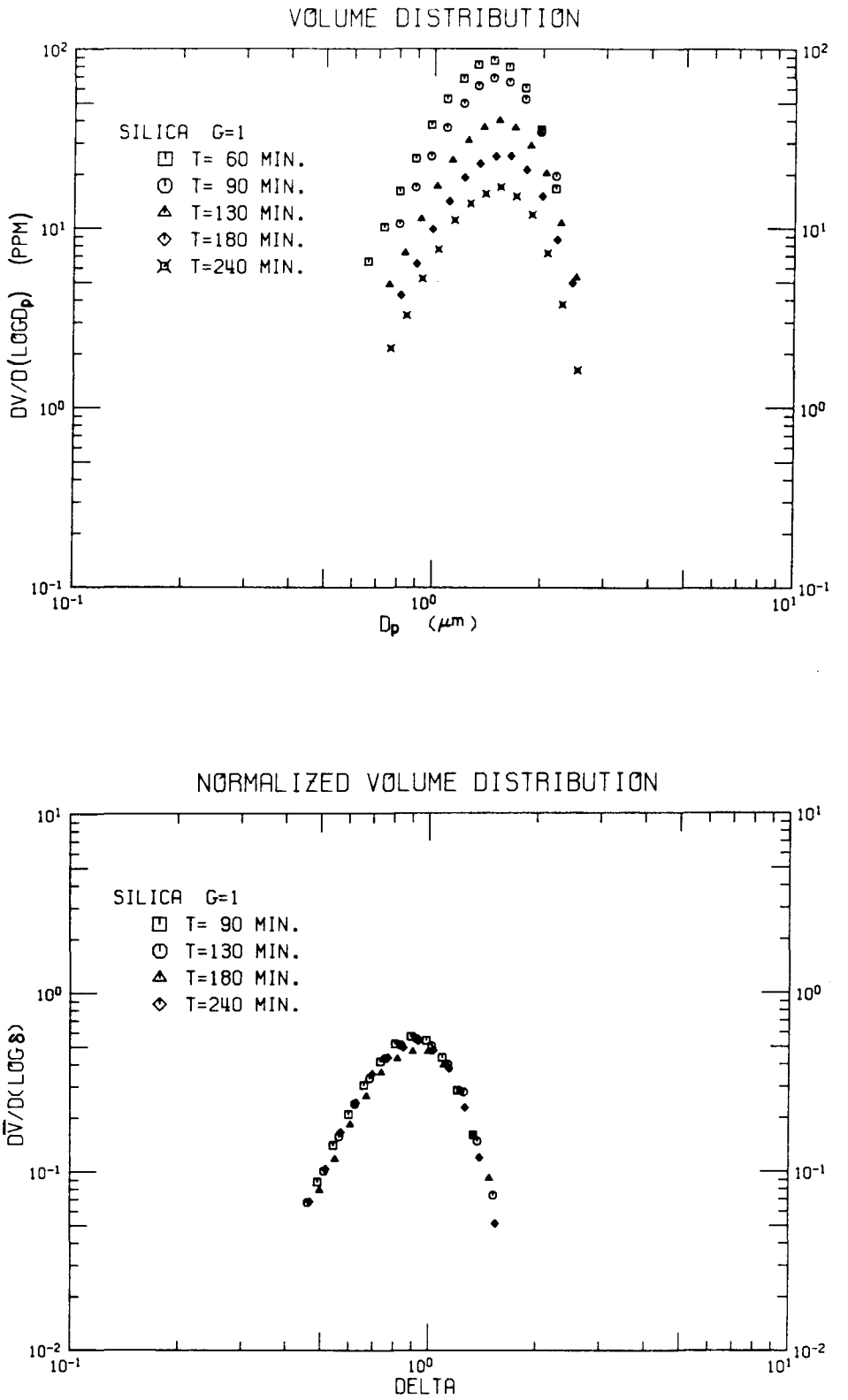

Figure 4.33 Volume distributions and normalized volume distributions for silica at $G = 1\ sec^{-1}$.

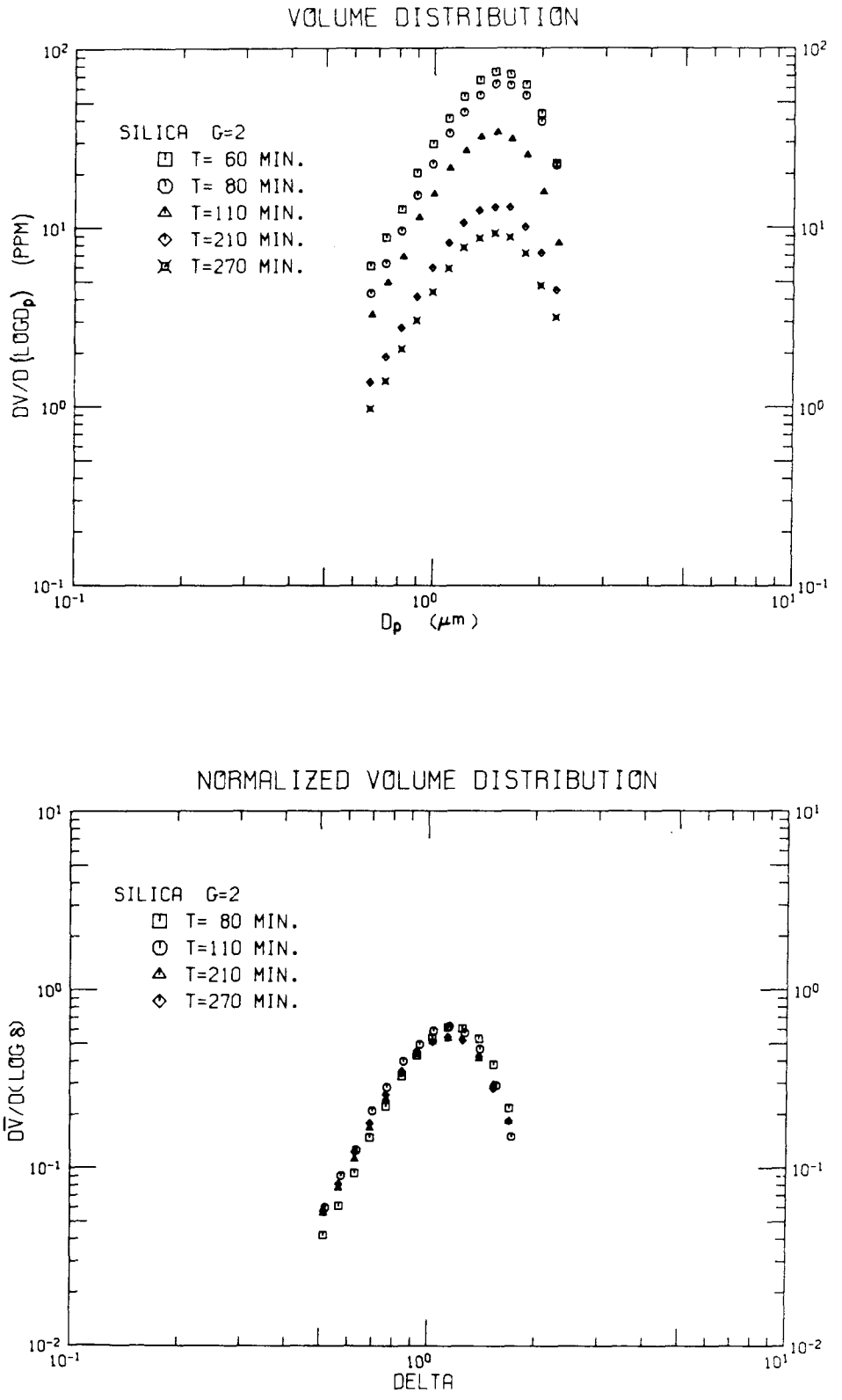

Figure 4.34 Volume distributions and normalized volume distributions for silica at G = 2 sec^{-1}.

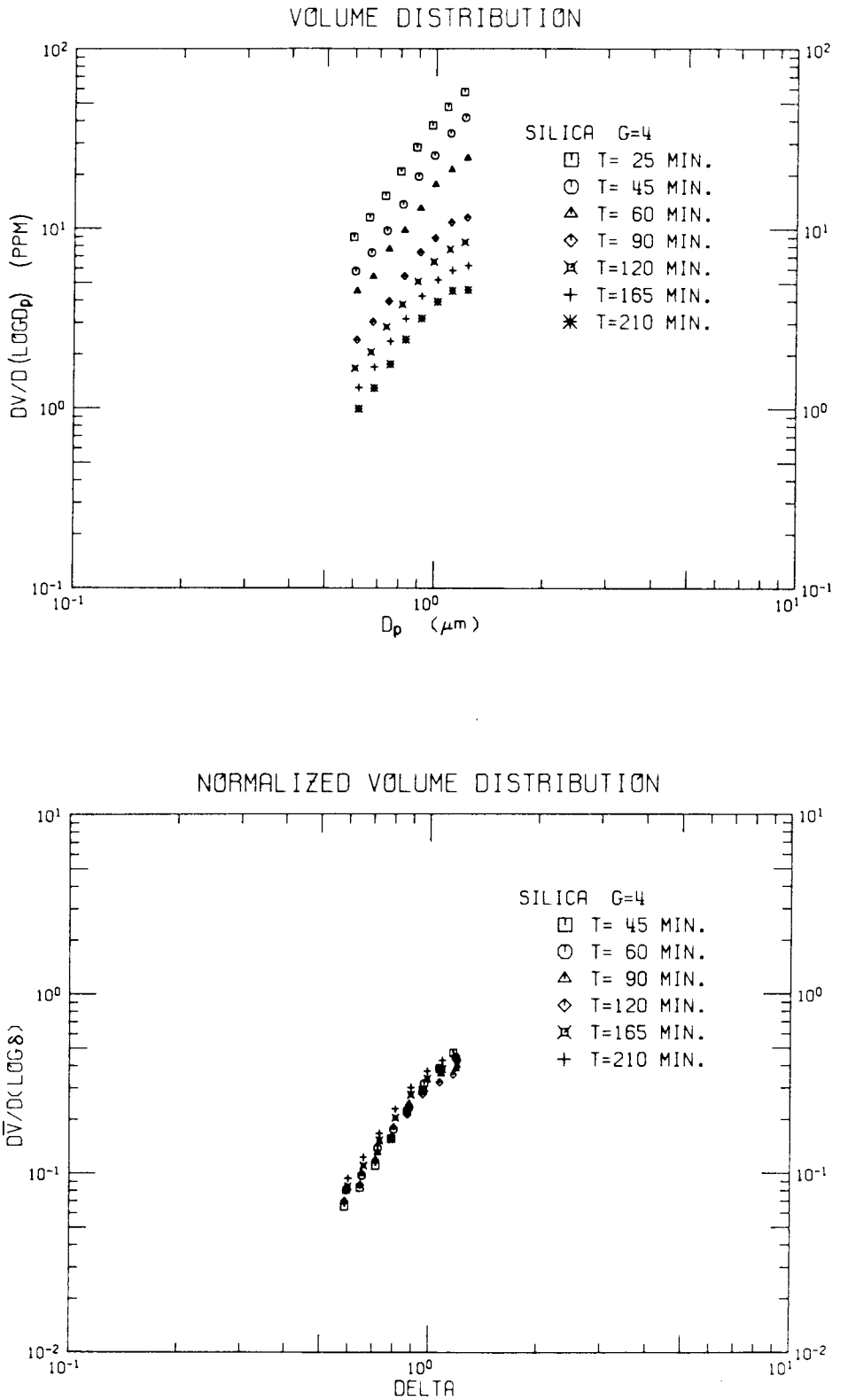

Figure 4.35 Volume distributions and normalized volume distributions for silica at $G = 4\ sec^{-1}$.

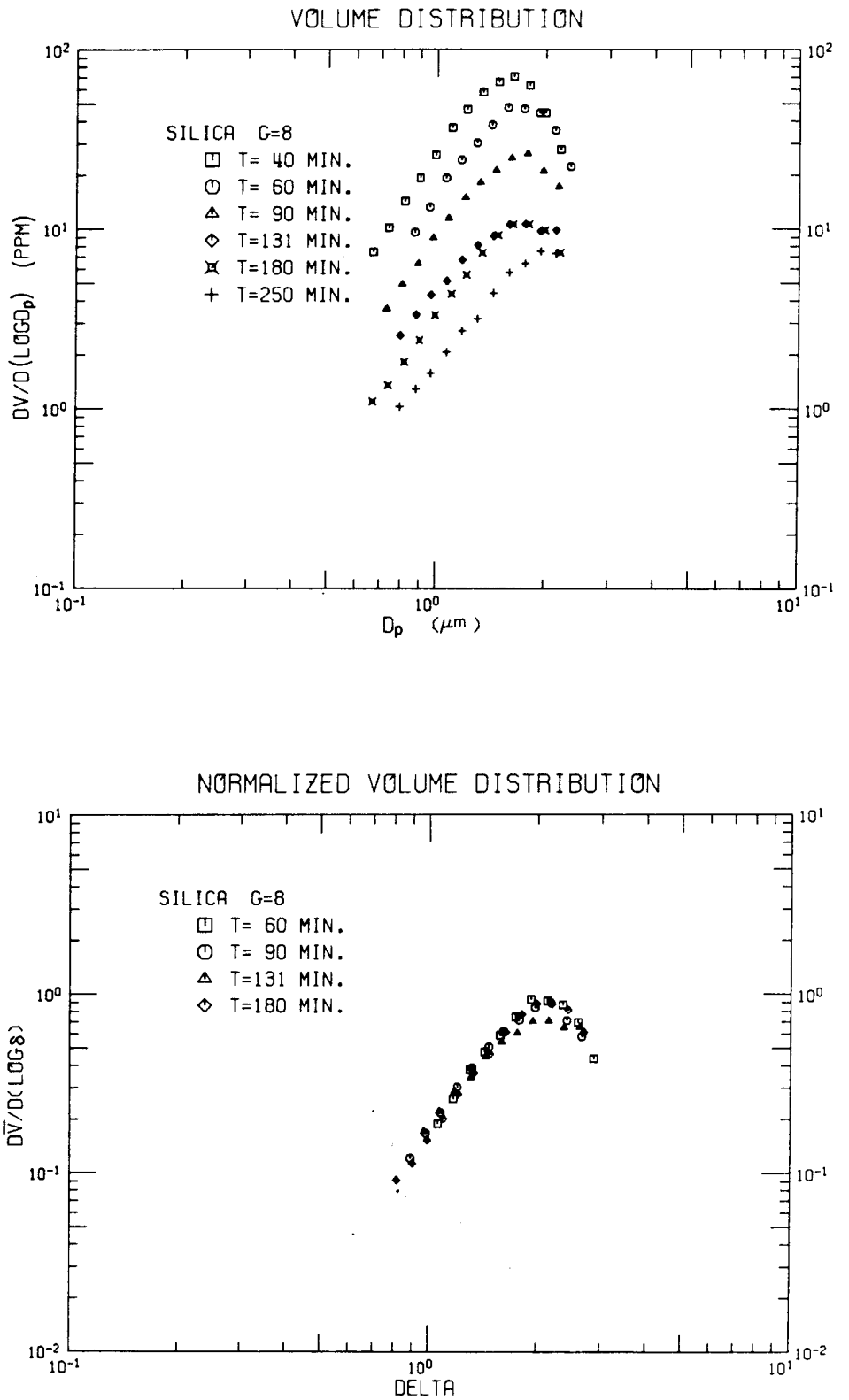

Figure 4.36 Volume distributions and normalized volume distributions for silica at $G = 8\ sec^{-1}$.

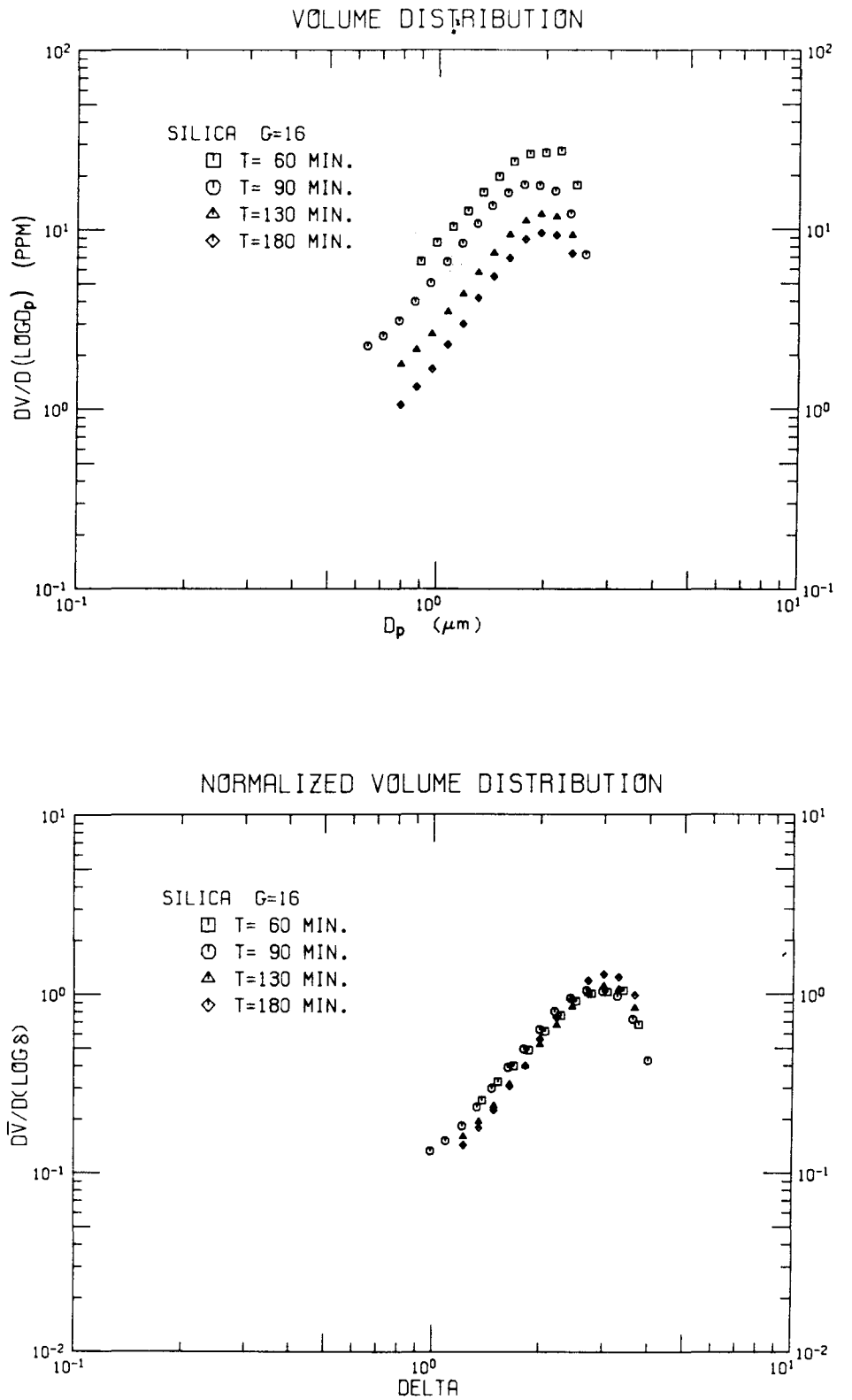

Figure 4.37 Volume distributions and normalized volume distributions for silica at G = 16 sec^{-1}.

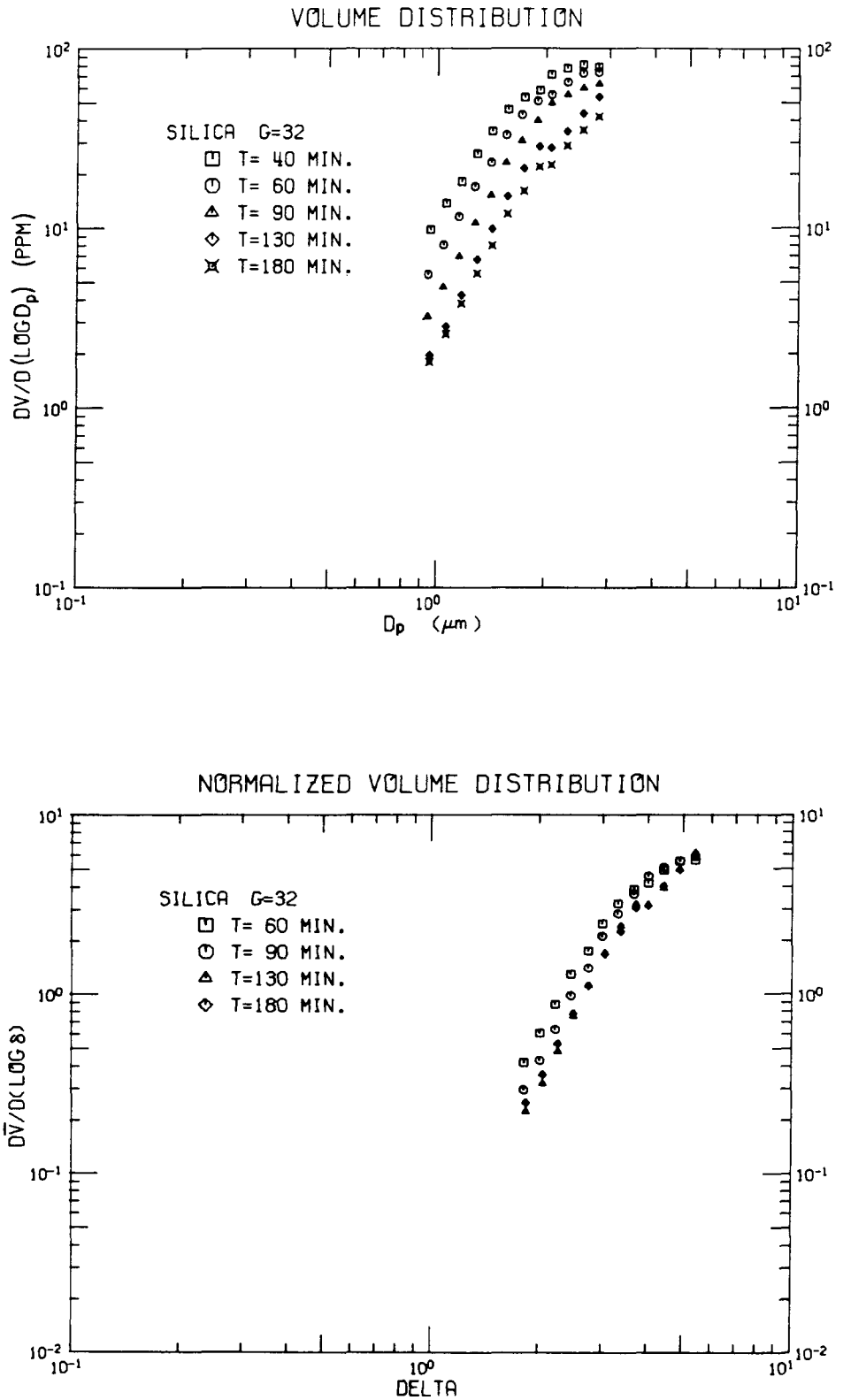

Figure 4.38 Volume distributions and normalized volume distributions for silica at $G = 32\ sec^{-1}$.

sample at $G = 2\ sec^{-1}$ and another at $G = 16\ sec^{-1}$. At both shear rates the volume distributions measured with 30 to 70 μm apertures were in agreement, with greater overlap at the higher shear rate. No overlap with 140 μm aperture data was achieved at either shear rate, although at $G = 16\ sec^{-1}$ the 140 μm aperture data were close to the 70 μm aperture data. Volume distributions in Figure 4.35 at $G = 4\ sec^{-1}$ were limited to particle diameters less than 1.2 μm because of a problem in sizing larger diameters with the Coulter Counter during that experiment.

The volume distributions at each shear rate maintained a self-similar distribution over time, and on normalization, substantial reduction in spread was obtained. The lag time of 50 to 90 minutes observed in the inverse volume plots was caused by the time necessary to form larger settleable aggregates from the low initial concentration of small particles. The magnitude of the volume distributions for the early samples at all shear rates declined, but these data could not be normalized because the volume flux was estimated from changes in total suspended volume.

The shapes of the normalized volume distributions for all shear rates are compared in Figure 4.39 which excludes the regions dominated by aggregate breakup during counting. None of the normalized data at different shear rates agree, and the theoretical predictions for coagulation and settling do not describe the distributions. The normalized volume distributions increase roughly with δ^4 for $G = 1$, 2, and 32 sec^{-1} and with δ^3 for $G = 4$, 8, and 16 sec^{-1}. The volume distributions are nearly independent of shear rate and the spread in Figure 4.39 is due to the normalization procedure.

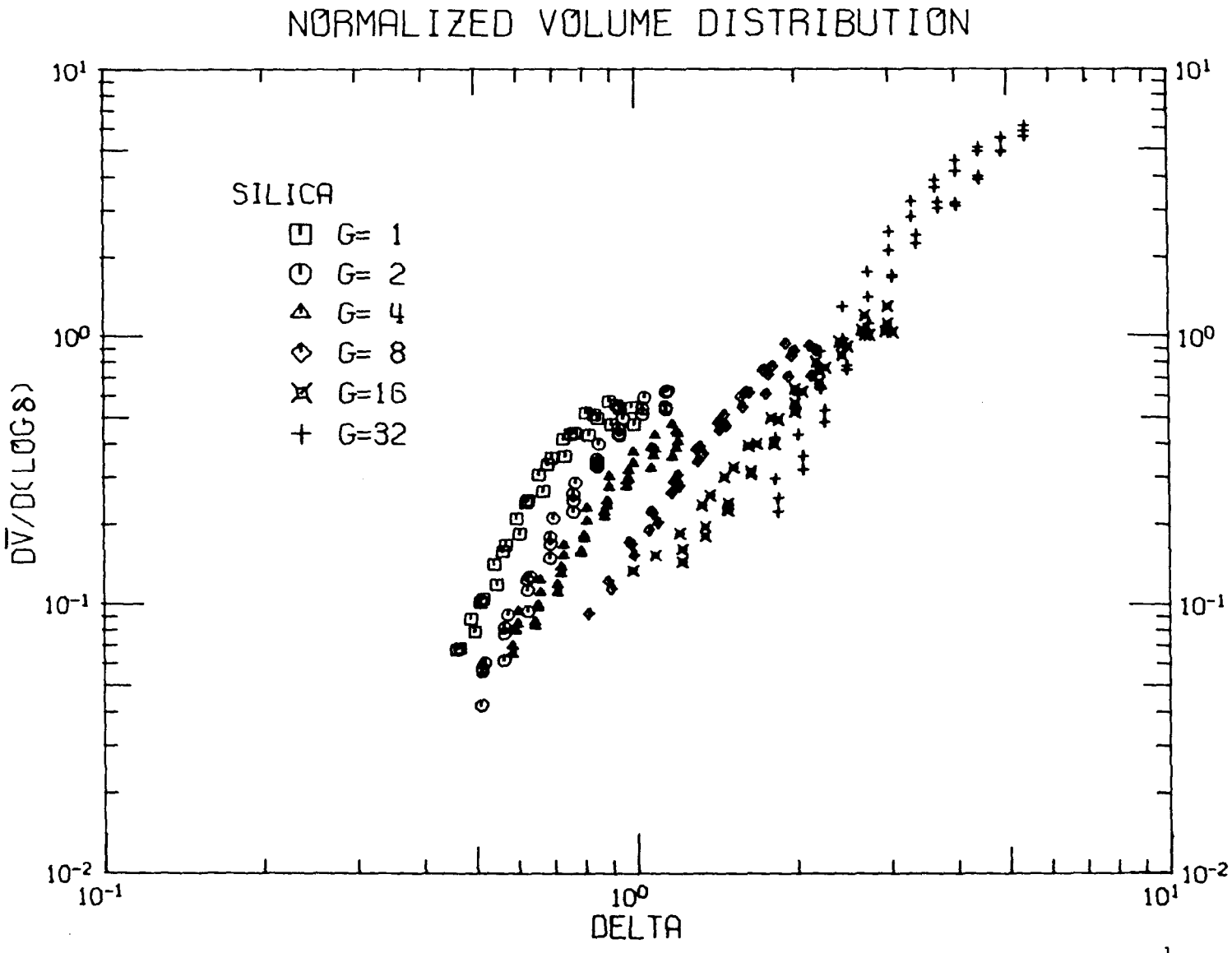

Figure 4.39 Normalized volume distributions for silica at G = 1,2,4,8,16, and 32 sec^{-1}.

The experiments with cleaned silica in artificial seawater are characterized by low rates of suspended volume removal and volume distributions which were nearly independent of shear rate. The observed volume distributions cannot be explained by the predictions for coagulation and settling because silica is not completely destabilized in seawater, as discussed in the next two sections.

4.5 Discussion of Experimental Results

In this section the results of the experiments with different solids are compared with predictions, and explanations are offered for the differences observed among the solids and for deviations from the predictions at higher shear rates. To guide in the discussion, Figure 4.40 is included; it plots the second order rate constants for total suspended volume removal, b, at different shear rates for the kaolinite, illite, montmorillonite, and silica experiments.

Relevant data on solid and aggregate properties are included in Table 4.5 along with the measured Brownian and shear coagulation dimensionless constants. Sediment per cent solid volume was obtained for each solid by preparing an approximately 300 ppm by volume suspension in artificial seawater. The sediment volume was recorded after one day

Table 4.5 Solid and sediment properties and dimensionless constants for Brownian and shear coagulation.

Solid	Exchange Capacity (meq/100g)	Sediment Per Cent Solid Volume	A_b	A_{sh}
Kaolinite	12.2	1.4	0.19	0.15
Illite	25.0	1.1	0.4	0.12
Montmorillonite	153.0	0.11	>0.5	0.08
Silica	--	2.	--	--

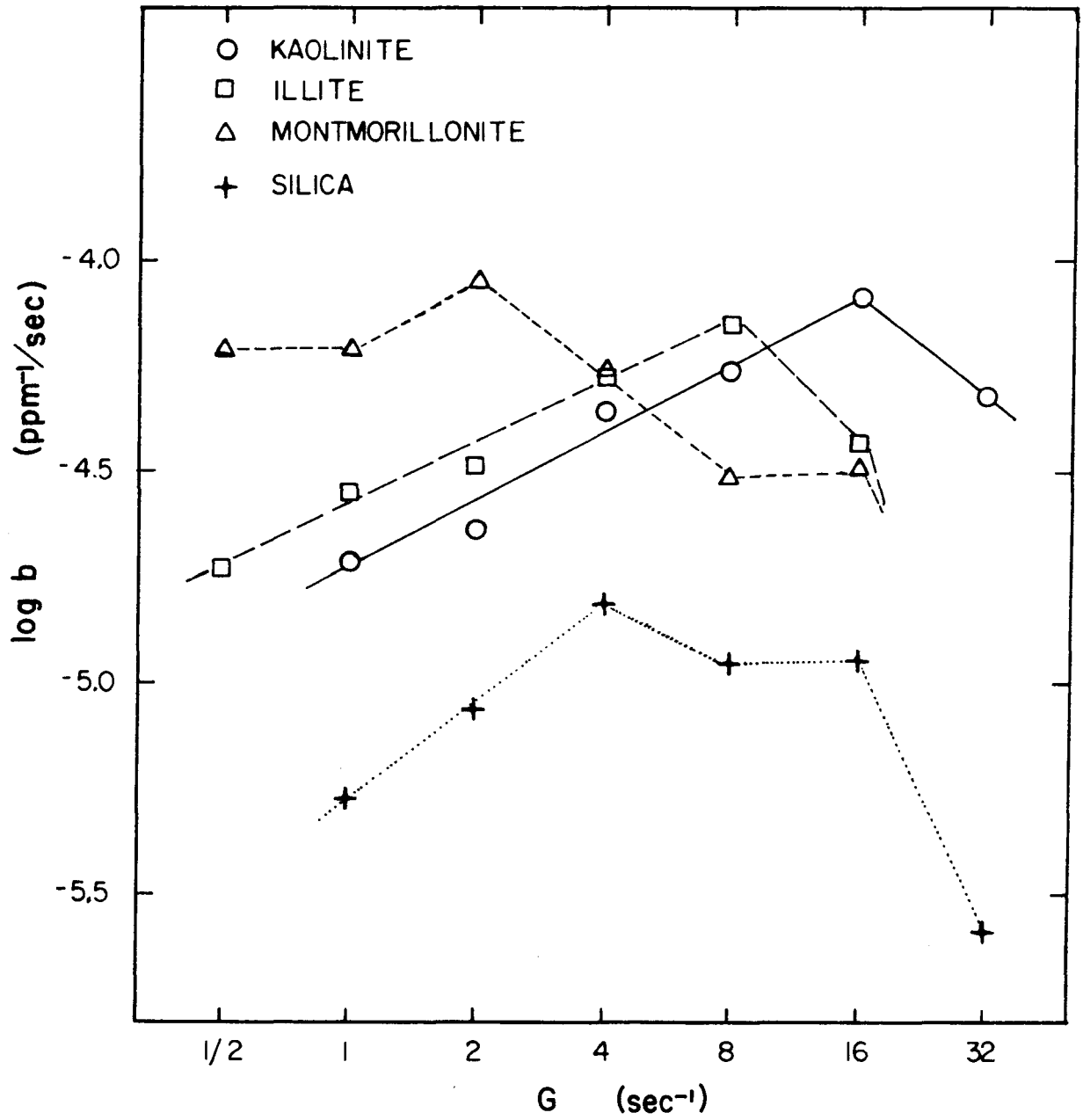

Figure 4.40 Volume removal rate constant as a function of shear rate for kaolinite, illite, montmorillonite, and silica experiments in artificial seawater.

of quiescent settling in a 100 mL graduated cylinder of 1.3 cm inside diameter. Individual aggregate porosity was not measured and the sediment per cent solid values are an approximate inverse indicator of aggregate porosity. The lower the per cent solids in the sediment, the greater the individual aggregate porosity.

Comparison of data with coagulation predictions is valid only for removal rate constants which increase with increasing shear rate, specifically for kaolinite, $G \leq 16$ sec^{-1}; illite, $G \leq 8$ sec^{-1}; montmorillonite, $G \leq 2$ sec^{-1}; and silica, $G \leq 4$ sec^{-1}. All data obtained at $G = 32$ sec^{-1} should be suspect because there was no total suspended volume removal at this shear rate for the illite and montmorillonite experiments, probably because of a fluid instability in the rotating cylinder apparatus. Total suspended volume was removed during the kaolinite and silica experiments at $G = 32$ sec^{-1} because the denser aggregates were able to overcome the vertical fluid velocities. The decline in the volume removal rate constant with increasing shear rate up to 32 sec^{-1} is interpreted as a consequence of weak aggregate breakup by fluid shear in the rotating cylinder apparatus.

For the clay mineral experiments at low shear rates, the theoretical predictions were tested and verified both for the shape of Brownian and shear coagulation dominated regimes, and for the dependence of the size distribution on the shear rate and volume flux through the distribution. Kaolinite and illite had regions dominated by Brownian and shear coagulation while only a shear dominated region was observed for montmorillonite. A lower bound on the Brownian coagulation dimensionless constant, A_b, for montmorillonite is included in Table 4.5.

The three clay minerals were observed to differ in two ways. First, the separation between Brownian and shear coagulation dominance occurred at different normalized diameters, and second, at a given shear rate, the volume removal rate constant was dependent on the kind of solid. Both of these observations can be explained qualitatively by the variation in the clay aggregate porosities.

The shift in the regions dominated by Brownian and shear coagulation for the three clays is probably an artifact of the Coulter Counting principle. The Coulter Counter responds only to solid particles in the sensing zone and not the electrolyte, so the signal produced for an aggregate is proportional only to the solid volume, not the aggregate volume. For a very porous montmorillonite aggregate, the reported diameter would be much smaller than the aggregate diameter. Experimentally, Brownian coagulation was not observed for normalized diameters down to $\delta = 0.3$. Illite had a Brownian dominated region for $\delta < 0.5$ and kaolinite with lowest aggregate porosity had a Brownian region for $\delta < 1.0$. Treweek and Morgan (1977) presented a correction to Coulter Counter measured aggregate sizes to account for aggregate porosity, but the empirical technique has application only to a suspension of initially monodisperse primary particles.

The clay removal rate constants in Figure 4.40 for $G \leq 2$ sec^{-1} indicate that montmorillonite was removed faster than illite which was removed faster than kaolinite. These results are explained qualitatively based on the aggregate porosity, since a very porous aggregate has a greater collision cross section than a less porous aggregate containing the same solid volume. The larger collision

cross section increases the collision frequency, which increases the volume removal rate.

The theoretical predictions for coagulating and settling size distributions were integrated in Appendix D to arrive at expressions for the total suspended volume as a function of time:

$$V(t) = \frac{1}{a+bt} \tag{4.11}$$

where a and b are constants and b was predicted to be dependent on the fluid shear rate. From Figure 4.40, the removal rate constant was approximately proportional to $G^{1/2}$ for the clay data and to about $G^{3/4}$ for silica. The observed removal rate constants increased with the shear rate but comparison with predicted removal rates was not possible without knowledge of the parameters and dimensionless constants for differential sedimentation coagulation and gravitational settling.

The experimental results for silica at shear rates of 4 sec^{-1} and less are not in agreement with size distributions predicted either for Brownian or for shear coagulation. In seawater, silica is probably not destabilized, which causes the low removal rates and lack of agreement with predictions. This result is in accord with silica coagulation rates observed by others as discussed in the next section.

At higher shear rates in the illite and montmorillonite experiments, aggregate breakup by fluid shear became important in the gap of the rotating cylinder apparatus. The decline in removal rates, the increase in volume distributions, and the increase in aggregate strength all support this explanation. At low shear rates, aggregates are formed and removed by settling without disruption. At higher shear rates,

weak aggregates are disrupted, which limits aggregate size and decreases the rate of particle volume removal by sedimentation. This combination of coagulation and breakup causes an accumulation of aggregates in the volume distribution and an increase in the strength of the aggregates. The more porous montmorillonite aggregates were observed to be breakup-dominated at shear rates of 4 sec^{-1} and greater, while less porous illite aggregates became breakup-dominated at 16 sec^{-1}.

The experimental results of the different clay minerals are strongly related to the porosity of the coagulated particles. The variation in porosity is due to the difference in exchange capacities of the three clays listed in Table 4.5 and the resulting aggregate structures in seawater. The individual clay particles are in the shape of thin sheets with negative charges on the faces and positive charges on the edges. van Olphen (1977) has discussed the dependence of aggregate structure on ionic strength as interpreted from the rheological behavior of clay suspensions. With increasing ionic strength there is a shift from porous edge-to-face aggregates (house-of-cards structure) to denser face-to-face aggregates; the ionic strength for this transition increases with increasing exchange capacity. Thus, in seawater montmorillonite has a more porous aggregate structure than illite, which is more porous than kaolinite, corresponding to different degrees of edge-to-face clay particle association. Silica particles are not plate-like and do not have distinct regions of opposite charge.

4.6 Comparison with Previous Coagulation Studies

Previous studies of particle coagulation kinetics have usually compared the observed initial coagulation rate with the theoretical

rate for a monodisperse suspension as given in Equation (2.15) for shear coagulation. The ratio of the observed coagulation rate to the theoretical rate has been called the collision efficiency and is usually a measure of the extent of destabilization. At this time there is no quantitative relationship between collision efficiency and the dimensionless coagulation constants. Qualitatively, high collision efficiencies correspond to high coagulation rates, which would give high volume removal rates, and this corresponds to a low value of the shear coagulation constant (see Appendix D).

Clay particle dynamics in estuarine waters has been studied by Whitehouse *et al.* (1960) and Edzwald *et al.* (1974) with different results. Whitehouse *et al.* measured the quiescent settling velocity of clays in varying salinity seawaters. The experimental methods have been criticized by Edzwald and O'Melia (1975) because shear coagulation, which is important in natural waters, was not included. Results of the present study have demonstrated the importance of the shear rate on the rate of total suspended volume removal.

Edzwald *et al.* conducted coagulation experiments with narrowly-sized kaolinite, illite, and montmorillonite in waters of varying salinity at a shear rate of about 52 sec^{-1}. At a salinity of 17 parts per thousand (ppt), montmorillonite coagulated faster than kaolinite which coagulated faster than illite. The collision efficiency observed for montmorillonite was 15 per cent. No coagulation experiments were conducted at salinities greater than 17 ppt.

Eppler *et al.* (1975) studied the coagulation kinetics of kaolinite, illite, montmorillonite, and silica in solutions of varying ionic

composition. No attempt was made to prepare initially narrow solid distributions. In 1 M NaCℓ the observed ordering of collision efficiency from largest to smallest was montmorillonite, kaolinite, illite, and silica, agreeing with the clay results of Edzwald *et al.*

Earlier studies of silica coagulation kinetics were conducted by Hahn and Stumm (1968) using hydrolyzed Aℓ(III) for destabilization. At the optimum coagulant dose, the collision efficiency for shear coagulation was only 1.2 per cent.

These previous studies of the initial rate of particle coagulation are in qualitative agreement with the present results. Montmorillonite coagulates most rapidly and silica least rapidly in all the available data, while the present results indicated illite was slightly faster than kaolinite, the opposite of the results of Edzwald *et al.* and Eppler *et al.* Two possible explanations for this result are, first, the illite and kaolinite clays were not from the same geographical location, and second, only in this work were the clays cleaned and converted to the sodium form. Except for the experiments of Hahn and Stumm, the shear rates were fixed at about 50 sec^{-1}. At this high shear rate, aggregate breakup in the initial stages of coagulation probably was not a problem because the aggregates were small. Rates of total suspended volume removal in the present results became breakup-dominated at lower shear rates because larger aggregates were present.

CHAPTER 5

SUMMARY AND CONCLUSIONS

Particle coagulation is important in determining the fate of suspended particles in oceanic waters, but previous theories for coagulation are not applicable to the continuous particle size distributions encountered in natural waters.

In this work an approach developed by Friedlander for aerosol coagulation and sedimentation was extended to hydrosols. After considerable simplification, predictions of particle size distributions were obtained dimensionally for size intervals dominated by Brownian, shear, and differential sedimentation coagulation, and gravitational settling. The size distributions were assumed to be in a dynamic steady state maintained by a flux of particle volume through the distribution.

Experiments were designed to test the validity of the predictions using cleaned clay and silica minerals in artificial seawater. Batch experiments were conducted in the gap of a rotating cylinder apparatus which maintained laminar fluid flow at different shear rates and allowed aggregate settling. For each mineral, a series of experiments was conducted at fixed shear rates with measurements taken over time of aggregate size distributions and total suspended volume. Within the uncertainties of the experimental system, the Brownian and shear coagulation predictions were verified at low shear rates for kaolinite and illite. Only the shear coagulation prediction was verified for montmorillonite. Experiments with cleaned silica were not in

agreement with any of the predicted size distributions probably because silica was not completely destabilized in seawater. Because of larger aggregate breakup during counting, experimental verification of predictions for differential sedimentation coagulation and gravitational settling was not possible for any of the solids.

At higher rates of fluid shear, the total suspended volume removal rate decreased; the maximum removal rate occurring at 2 sec^{-1} for montmorillonite, 4 sec^{-1} for silica, 8 sec^{-1} for illite, and 16 sec^{-1} for kaolinite. For shear rates higher than these values, clay aggregate size distributions no longer agreed with theoretical predictions due to aggregate breakup by fluid shear in the rotating cylinder apparatus.

While the experimental results for the three clays were in agreement with the predictions, there was considerable variation in regions of Brownian and shear coagulation dominance, total suspended volume removal rates, and susceptibility to aggregate breakup in the rotating cylinder apparatus. These results were explained by the porosity of the clay aggregates in seawater. For very porous aggregates, the diameters reported by the Coulter Counter were much less than the aggregate diameters, which shifted the regions dominated by Brownian and shear coagulation. Increased porosity increased the collision cross section, thus the removal rate, and a highly porous aggregate would be weak and disrupted at low shear rates. These differences in clay coagulation were reflected in the dimensionless constants for Brownian and shear coagulation which must be determined experimentally at this time. Since clay aggregate porosity is a function of exchange capacity and ionic strength, the dimensionless constants are probably

a function of solution composition, although this was not examined.

This approach to coagulation has direct application to understanding particle removal from oceanic waters for particles produced biologically, discharged from an outfall, or resuspended from bottom sediments. For these conditions, prediction of suspended particle removal requires more information than has been available. Specifically, the dimensionless coagulation constants must be known along with the fluid shear rate. Determination of the dimensionless constants involves a rather lengthy series of experiments, and fluid shear rates are not easily measured in the field.

This research is an initial attempt at a theoretical and experimental study of coagulation in continuous particle size distributions. In the course of the work, a number of areas for further research have been identified. First, to adequately test the validity of the predictions for differential sedimentation coagulation and gravitational settling, new sizing techniques are needed for larger aggregates. Second, to apply the theory to estuarine waters and water and wastewater treatment operations, the influence of solution composition must be studied. Third, a better theoretical and experimental understanding of aggregate disruption is needed, both in terms of the particle size distribution and in the total suspended volume removal rate. Finally, it should be recognized that the fluid flow in the experiments was laminar, while in natural waters and in water and wastewater treatment operations, the fluid motion is turbulent. For turbulent fluids a mean shear rate may not be an adequate representation of the fluid motion for consideration of particle dynamics in continuous particle size

distributions. An experimentally verified theory for Brownian and shear coagulating size distributions should provide a reasonable starting point for the investigation of these topics.

APPENDIX A

EMULSION EXPERIMENTS

Because solid aggregates could not be completely sized by the Coulter Counter, coagulation and settling of dilute oil in water emulsions were briefly examined. Emulsion experiments possessed some ideal properties for testing the size distribution predictions, namely, coalesced aggregates would not be broken up by the Coulter Counter sensing technique, and the density of all particles would be known. Unfortunately, simple chemical systems of oil droplets in solutions of high ionic strength were not completely destabilized as was assumed in the derivation, and only very slow coagulation was observed. Results of emulsion experiments cannot be used for testing predictions, but the data have some interesting features and should be useful to others.

Preparing oil in water emulsions and separating oil droplets from water are important in many fields, including food processing, pharmaceuticals, tertiary oil recovery, and oil removal from wastewaters. A recent review by Carrol (1976) summarized current knowledge on the preparation of stable emulsions and the methods for destabilizing emulsions for phase separation. The review indicated the lack of general theoretical principles with wide application and the generally empirical nature of most emulsion studies.

Few studies of oil droplet coagulation kinetics are available because monodisperse droplet suspensions cannot be produced and theoretical predictions have not been available for polydisperse suspensions. An

attempt at measuring coagulation kinetics was reported by Bernstein *et al.* (1971) where the total number of droplets greater than the lower limit of detection of the Coulter Counter were counted over time. Total counts were used to obtain a second order rate constant for Brownian coagulation, a procedure valid only for monodisperse suspensions. The second order rate constant at 0.9 per cent NaCℓ decreased with the addition of sodium lauryl sulfate; a surfactant. Without surfactants, oil in water emulsions of ditolyl, dioctyl phthalate-dibutyl phthalate, hexadecane, and Unity Oil were destabilized by high ionic strength. Spielman and Goren (1972) formed destabilized silicone oil emulsions when solutions of silicone oil dissolved in acetone were injected into a nitric acid solution. Destabilization was stated as complete at 0.6 per cent by weight nitric acid because further increases in acid concentration did not increase coagulation rate. The method for determining the coagulation rate was not indicated. Wasan *et al.* (1978) have examined the stability of emulsions in tertiary oil recovery with salt solutions, surfactants, and cosurfactants. Emulsion stability was correlated with interfacial viscosity and interfacial tension.

Emulsion coagulation and settling experiments were designed to be as simple as possible with only an oil droplet emulsion prepared mechanically in an aqueous phase of high ionic strength. A Model B Coulter Counter was interfaced to the multichannel analyzer system for sizing. The calibration and analysis procedures were similar to the experimental techniques described in Appendix B. All

labware was washed in warm detergent solutions of MICRO and rinsed in warm water followed by distilled deionized water. Two sets of experiments are described, light paraffin oil in 2.0 M $CaCl_2$ and 4.0 M $NaClO_4$, and Dow-Corning 710 silicone oil in 1.0 M NaCl.

A.1 Light Paraffin Oil

Light paraffin oil (MC/B, PX 44-07) had a reported viscosity of 0.381 cm^2/sec at 37.8°C (100°F) and a measured density of 0.854 g/cm^3. In the first experiment 0.5 mL of light paraffin oil was mixed with 200 mL distilled deionized water in a Servall Omni-Mixer. Forty milliliters of the emulsion were mixed by hand with 160 mL of filtered 2.5 M $CaCl_2$ resulting in a 500 ppm oil emulsion in 2.0 M $CaCl_2$. The shear rate in the rotating cylinder apparatus was set at 1 sec^{-1}, and volume distributions obtained over time with 30, 70, and 140 μm apertures are plotted in Figure A.1. The lower limit of detection was only 1.7 μm because of electronic noise in the Coulter Counter.

The dispersion of light paraffin oil in 2.0 M $CaCl_2$ appeared to be stable and the dominant removal mechanism was floating of individual particles to the surface. After almost 4 hours the droplet volume distribution less than 5 μm did not change substantially while the larger droplets were removed by floating. Table A.1 lists the total droplet volume obtained by integration of the volume distributions at each sample time. While an initial total suspended volume of 500 ppm was expected only 51.8 ppm was observed at the first sample.

A second coagulation experiment with light paraffin oil in 4.0 M $NaClO_4$ examined the influence of ionic media. Also an attempt

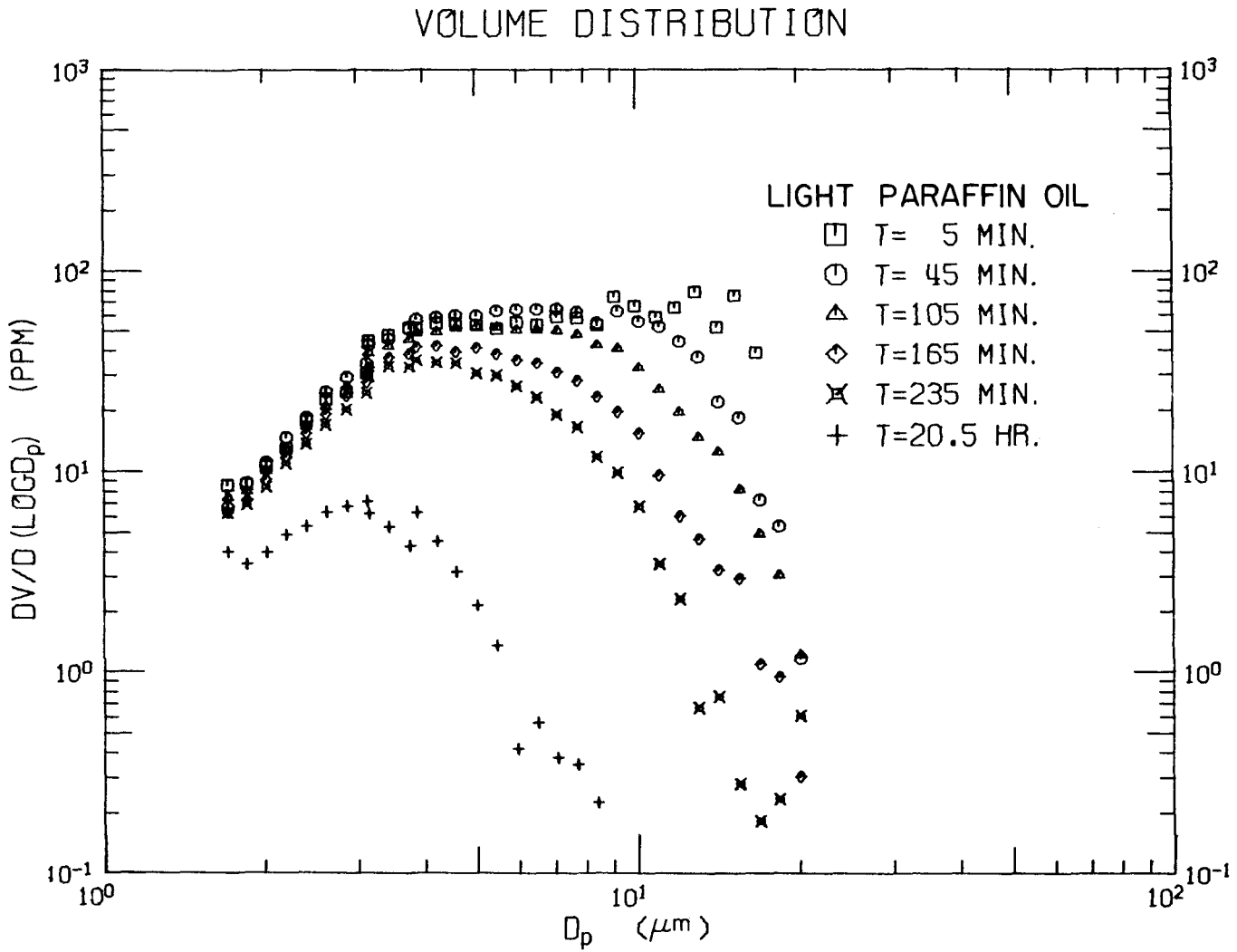

Figure A.1 Volume distributions of a light paraffin oil emulsion in 2.0 M $CaCl_2$ at G = 1 sec^{-1}. Aperture sizing intervals were: 30 μm, 1.7 to 3.8 μm; 70 μm, 3.9 to 8.5 μm; 140 μm, 9.2 to 20 μm.

Table A.1 Suspended volume for light paraffin oil experiment in 2.0 M $CaCl_2$ at G = 1 sec^{-1}.

Time	Volume (ppm)
5 min.	51.8
45 min.	45.0
105 min.	34.1
165 min.	23.6
235 min.	17.7
20.5 hr.	2.7

Table A.2 Suspended volume and minimum droplet diameter expected for light paraffin oil experiment in 4.0 M $NaClO_4$ at G = 4 sec^{-1}.

Time	Volume (ppm)	Minimum Diameter (μm)
10 min.	313.	25
35 min.	32.4[a]	13.5
90 min.	54.0	8.4
180 min.	24.3	5.9
270 min.	7.6	4.8
390 min.	3.4	4.0
22.5 hr.	0.38	1.2

[a]sample analyzed 30 minutes after collection.

was made to emulsify more paraffin oil by mixing 0.5 mL of oil with 200 mL of filtered 4.0 M $NaC\ell O_4$ in the Omni-Mixer at a Variac setting of 100 out of 140 for four minutes. The shear rate was 4 sec^{-1}. Volume distributions over time are plotted in Figure A.2 which again show the very slow rate of coagulation and the rapid removal of the larger droplets by floating to the surface. Discontinuities in the volume distributions result from misalignment problems between apertures. Table A.2 summarizes the calculated total suspended volume at the various sample times. The sample at 35 minutes was accidently left sitting for 30 minutes before counting and the larger particles were removed to the surface of the counting vial. A higher initial oil concentration was obtained but, the first measurement of particle volume at 313 ppm was much less than the 2500 ppm expected from the amount of oil added to the mixer. A large amount of the oil was not dispersed and found attached to the walls of the mixer.

The 4.0 M $NaC\ell O_4$ light paraffin oil experiment also allowed examination of droplet floating in the sheared annulus. During the experiment, the 5 cm sampling tube was placed at the same depth for all but the last sample where a 10 cm tube was needed. With a solution density of 1.299 g/cm^3 measured at room temperature and a light paraffin oil density of 0.854 g/cm^3, rising velocities can be calculated for a given droplet diameter using Stokes' equation. For each sample, the distance from the bottom of the annulus to the sampling tube and the time are known, allowing calculation of a droplet rising velocity which should not be sampled. The minimum droplet diameter that should

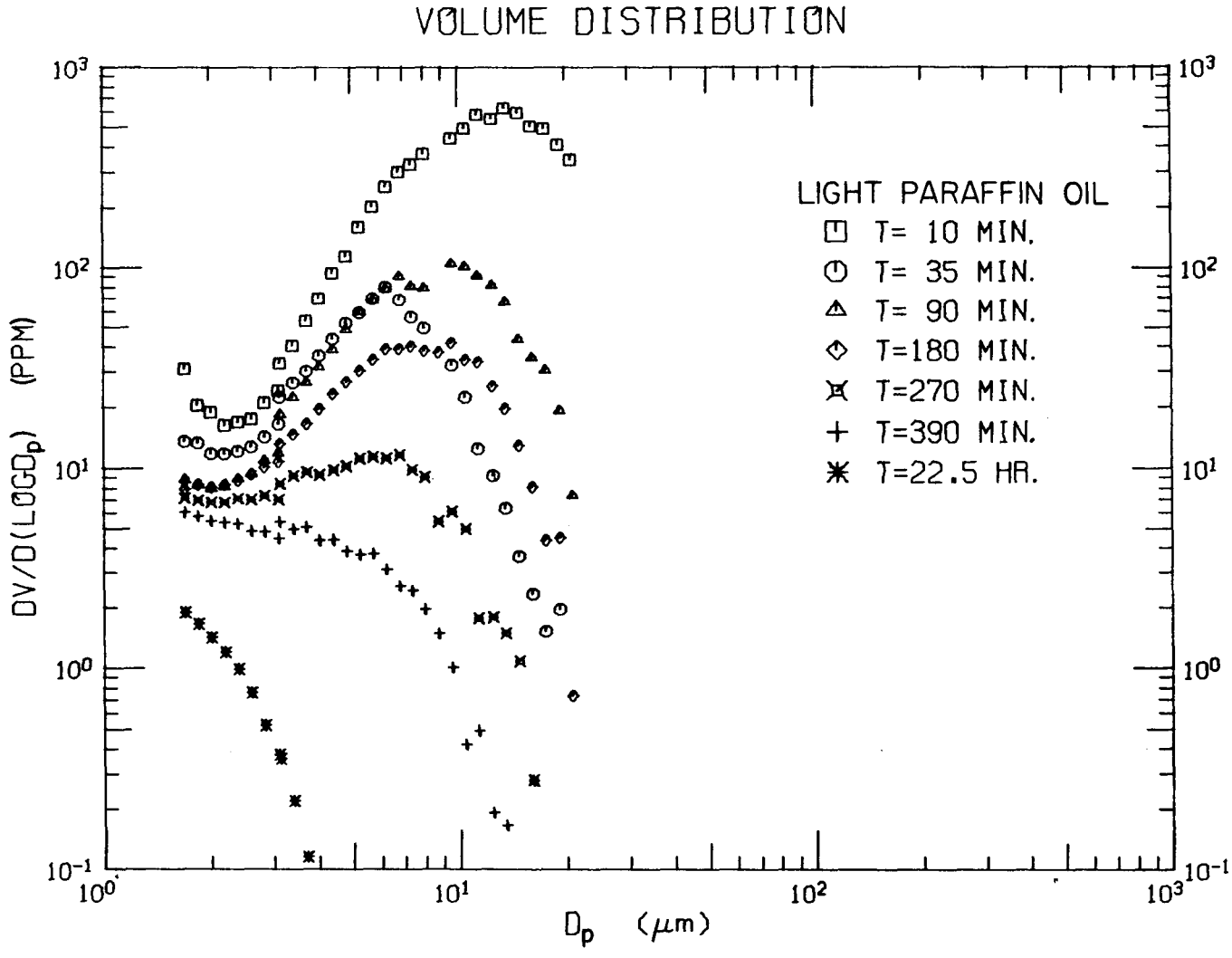

Figure A.2 Volume distributions of a light paraffin oil emulsion in 4.0 M $NaCl O_4$ at G = 4 sec^{-1}. Aperture sizing intervals were: 30 μm, 1.7 to 6.8 μm; 70 μm, 7.4 to 21. μm.

have floated above the sampling tube for each sample is listed in Table A.2. The short sampling tube was 7 cm off the annulus bottom and the long tube was 2 cm off the bottom. Corrections to Stokes' equation for internal currents within the oil droplets were less than one per cent due to the high oil viscosity. For all but the first two samples, droplets observed in solution are greater than the calculated droplet diameter which should have floated above the sampling tube. The observed volume distributions do begin to decrease substantially near the calculated cutoff, but some mechanism in the rotating cylinder apparatus appears to hinder settling of the sheared particles.

A.2 Silicone Oil

Following the lack of coagulation in paraffin oil experiments, silicone oil similar to that used by Spielman and Goren (1972) was examined. Dow-Corning 710 fluid is a phenylmethyl polysiloxane silicone fluid with an average molecular weight of 2600 g/mole, a density of 1.11 g/cm^3, and a reported viscosity of 300 cm^2/sec, both at 25°C. For the silicone oil experiments the shear rate was 4 sec^{-1} and the aqueous phase was 1.0 M NaCℓ at room temperature.

In the first experiment one drop of silicone oil was dispersed in 100 mL of distilled deionized water with the Servall Omni-Mixer for four minutes. The emulsion was mixed by hand with 100 mL of filtered 2.0 M NaCℓ and poured into the rotating cylinder apparatus. Nine volume distributions were measured from one minute after mixing to 24.5 hours as shown in Figure A.3a and A.3b. The total suspended volume

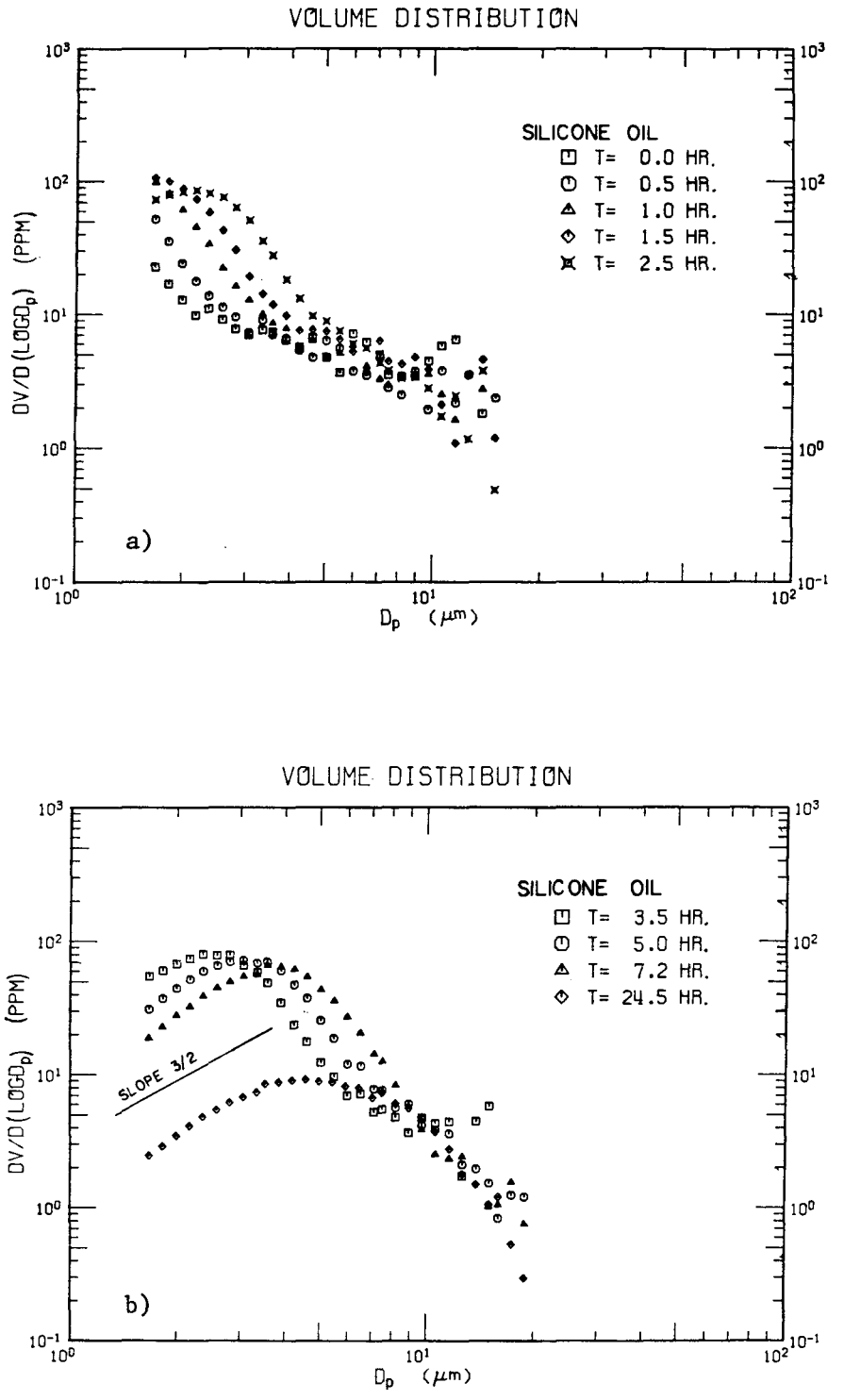

Figure A.3 Volume distributions of a silicone oil emulsion in 1.0 M NaCℓ at G = 4 sec^{-1}. a) T ≤ 2.5 hours, b) T ≥ 3.5 hours. Aperture sizing intervals were: 30 μm, 1.7 to 3.3 μm; 70 μm, 3.6 to 15. μm; 140 μm, 16. to 19. μm.

greater than 1.7 μm, the lower limit of detection, increased up to 7.2 hours after mixing as small droplets coagulated into the observable size range. Figure A.3b shows the development of a linear region of approximate slope 3/2 as predicted for a Brownian dominated region. Tests of theoretical predictions were not possible because a quasi-dynamic steady state was not achieved after 7.2 hours. The observed linear region of slope 3/2 out to 3 μm was unexpected for a shear rate of 4 sec^{-1} where Brownian should be dominant only below 1.3 μm based on Equation (3.1). Use of Equation (3.1) assumes Brownian and shear coagulation have the same collision efficiencies as experimentally observed by Swift and Friedlander (1964) for destabilized particle suspensions.

In the next experiment the amount of silicone oil was increased from one drop to 0.5 mL in an attempt to increase the suspended volume of oil and increase the frequency of droplet collisions. The same solution conditions and mixing procedures were used as before, and the resulting size distributions are shown in Figure A.4. More silicone oil was dispersed than in the previous experiment even though much oil remained on the walls of the mixing chamber. The volume distributions have poor alignment between apertures because of problems with the Model B Coulter Counter.

A line of slope 3/2 is drawn on Figure A.4 indicating, as in Figure A.3b, a possibly Brownian dominated coagulation region out to about 3 μm. The volume distribution for the larger droplets was dominated by settling and no calculation of volume flux was attempted for normalization because of the settling dominance. Suspended volumes

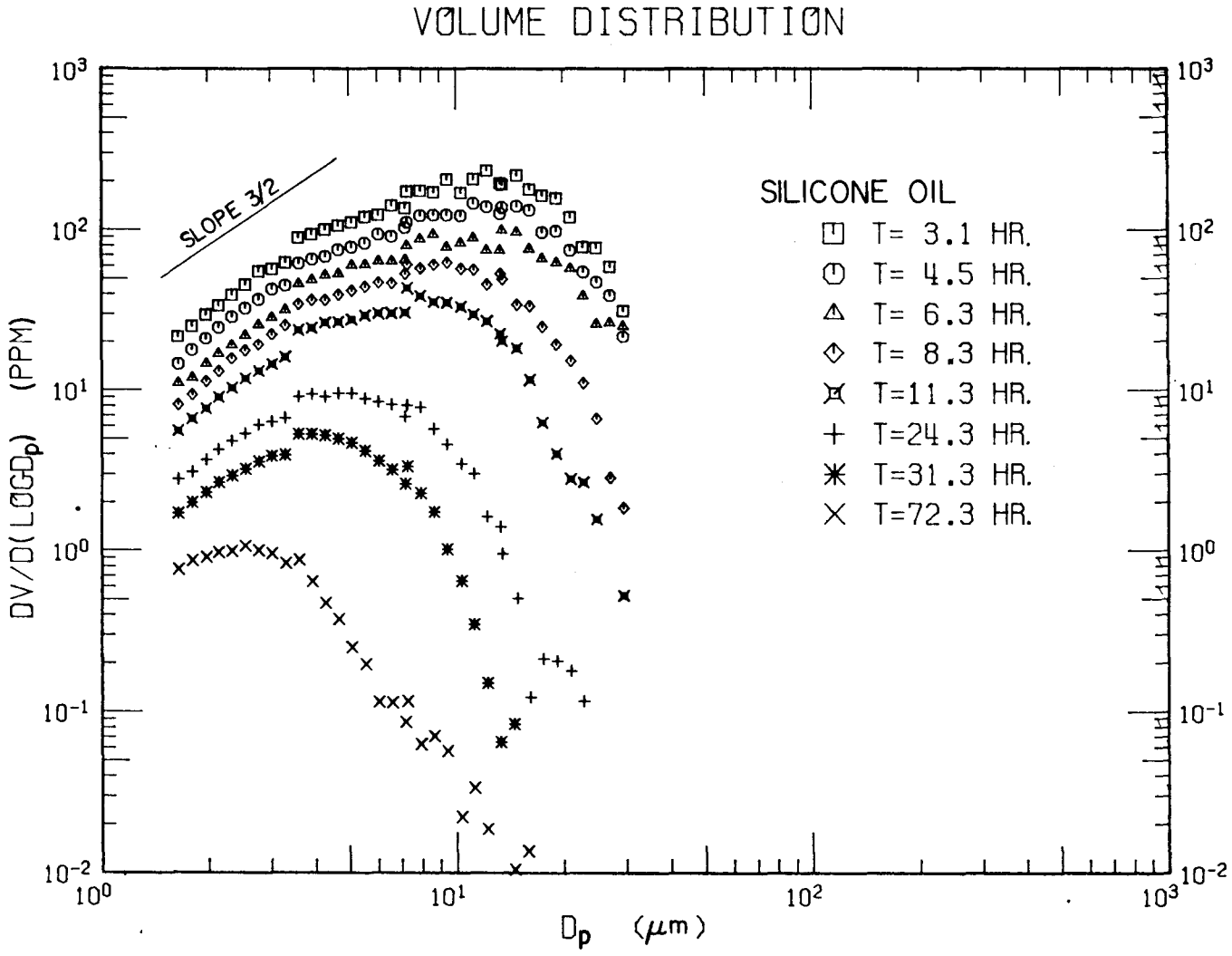

Figure A.4 Volume distributions of a silicone oil emulsion in 1.0 M NaCℓ at G = 4 sec^{-1}. Aperture sizing intervals were: 30 μm, 1.65 to 3.3 μm; 70 μm, 3.6 to 13.3 μm; 140 μm, 13.5 to 29.5 μm.

during the experiment are tabulated in Table A.3. The silicone oil experiments showed evidence of coagulation but very slowly unlike the rapid coagulation of silicone oil in acetone and nitric acid reported by Spielman and Goren (1972). The acetone possibly altered the surface of the silicone oil droplets such that collision and coalescence of droplets could occur.

Table A.3 Suspended volume for silicone oil experiment of Figure A.4.

Time (hour)	Volume (ppm)
3.1	150.
4.5	101.
6.3	68.
8.3	41.
11.3	23.8
24.3	6.9
31.3	2.75
72.3	0.45

A.3 Summary

Emulsion experiments were undertaken because the droplets would have well defined densities and the size distribution could be measured with a Coulter Counter without aggregate breakup. Unfortunately, the emulsions were not completely destabilized in the high ionic strength salt solutions as was necessary to test the theoretical predictions of Chapter 2. Light paraffin oil dispersed in various salt solutions showed no tendency to coagulate while silicone oil droplets developed a possibly Brownian dominated regime. Droplet removal for

both oils was controlled by settling. Existence of a Brownian dominated regime at particle diameters considerably larger than expected warrants further study of the efficiency of Brownian and shear collision mechanisms in partially stabilized emulsions.

APPENDIX B

MEASUREMENT OF PARTICLE SIZE DISTRIBUTIONS

This appendix discusses the procedures developed for obtaining particle size distributions with a modified Coulter Counter. The sizing instrument was a Model ZBI Coulter Counter modified to include multichannel analysis. Coulter Counters interfaced with multichannel analyzers have been used by others in this laboratory (Chang, 1973; Treweek, 1975; Faisst, 1976), but the techniques developed for calibration and sizing are sufficiently different to justify the lengthy discussion.

B.1 Principles of Operation

The Coulter Counter electronically senses the passage of a particle carried by a suspending electrolyte through a small orifice by noting the change in resistance across the orifice. Since particle resistivity is much greater than suspending electrolyte resistivity, the resistance across the orifice increases during passage of a particle. Theoretically, the resistance change is proportional to the particle volume when the particle diameter is less than 40 per cent of the orifice diameter. One aperture tube can effectively sense particles in the range from 2 to 40 per cent of the orifice diameter. To size broad distributions, multiple apertures are required and available in orifice diameters from 15 μm to 2000 μm.

Mechanically, the Coulter Counter operates by pulling the particle suspension through the orifice with a partial vacuum inside the

aperture tube. The volume of sample pulled through the orifice is measured by a mercury manometer with electrodes at preset intervals which transmit signals to start and stop particle counting.

B.2 Electronic Signal Processing

The Model ZBI Coulter Counter was not designed for rapid measurement of particle size distributions. The instrument was developed with a single channel analyzer to count only those particles within a given size range. This single channel analyzer was bypassed with output from the main amplifier sent to a particle sizing amplifier (Nuclear Data PSA) connected to a multichannel analyzer (MCA) with 128 channels for data storage (Nuclear Data MCA 555). Multichannel analyzer data were displayed on an oscilloscope (Hewlett Packard 1208B), and the data were saved by punching paper tape on a Teletype (ASR 33) with a teletype interface module (Nuclear Data TTY IN/OUT). The PSA, MCA, and TTY IN/OUT modules plugged into a System Power Supply (Nuclear Data Series 1100). The MCA had been modified by Nuclear Data for volumetric control (81-0335) to allow the mercury manometer of the Coulter Counter to control data acquisition.

The passage of a particle through the aperture causes a voltage pulse with the magnitude determined by the 1/CURRENT and 1/AMPLIFICATION settings of the Coulter Counter. Since $\Delta V = I\Delta R$, increasing the current, I, increases the voltage pulse ΔV. The 1/CURRENT setting is inversely proportional to the current, so decreasing 1/CURRENT will increase the voltage pulse. The 1/AMPLIFICATION setting is inversely proportional to the gain of a voltage amplifier, so decreasing 1/AMPLIFICATION

amplifies the voltage pulse. Coulter Electronics recommends minimum settings of 1/CURRENT to prevent nonlinear operation of amplifiers. Minimum settings are listed in Table B.1 for each aperture and the matching switch setting corresponding to the approximate resistance across the orifice for seawater media. The Model ZBI automatically

Table B.1 Coulter Counter settings of matching switch and minimum 1/CURRENT for artificial seawater media.

Aperture (μm)	Matching Switch (kΩ)	Minimum 1/CURRENT
30	40	1/4
70	20	0.177
140	10	0.088
280	5	1/16

switches current polarity through the electrodes between samples, preventing deposition of material on the electrodes.

The PSA logarithmically amplifies the voltage pulses from the main amplifier of the Coulter Counter. The equation relating the magnitude of the voltage pulse from the Coulter Counter ΔV_{in}, to the magnitude of the voltage pulse out of the PSA, V_{out}, is

$$V_{out} = (\text{fine gain})\ \log_x[(\text{coarse gain})\Delta V_{in}]$$

$$= (\text{fine gain})\ \log_x \Delta V_{in} + \text{constant} \qquad \text{(B.1)}$$

where (fine gain) and (coarse gain) are fine and coarse gain settings of the PSA and x is the base of the logarithm. From the mathematical identity $\log_b a \log_a M = \log_b M$, and noting that for $\log_b a$ = (fine gain), a = x, and M = ΔV_{in}, Equation (B.1) becomes

$$V_{out} = \log_b \Delta V_{in} + \text{constant} \quad . \tag{B.2}$$

This is the desired relationship for the output as a function of the input to the PSA with the log base, b, determined by the fine gain setting and found by calibration. Fixed settings for the PSA are given in Table B.2.

Table B.2 Fixed settings for the PSA.

Coarse Gain = 1
Fine Gain = 10.00
Log Bias = 0.50
POS (trigger on positive voltage pulse)
LOG (logarithmic conversion of input pulse)

The multichannel analyzer has a number of functions in the control of data collection, storage, and output. In the ACQUIRE mode, voltage pulses from the PSA are digitized and counts are sized and stored into 128 channels. ZERO positions signals in desired channels and upper and lower level discriminators (ULD, LLD) select the range in channels for storage. At the end of data acquisition, the counts stored in the 128 channels are written to a Teletype and punched on paper tape. Fixed settings for the MCA are summarized in Table B.3.

Table B.3 Fixed settings for the MCA.

PHA SEC/MCS MSEC = EXT (external trigger)
ZERO = 15
LLD = 3
ULD = 28
ACQUIRE = PHA (pulse height analysis)
AUTOCYCLE = SINGLE, ADD
Circuit Board Number 101; switch to ADC DIRECT
Backside: switch at OFF not DISTR
(data not erased after typing)
switch at PULSE not GATE

B.3 Calibration

Calibration of the sizing system requires determining the log base of the PSA logarithmic amplifier and the diameter at one of the 128 channels. With the log base and a reference channel of known diameter, the diameters at all other channels can be computed along with particle size distributions. One test of the calibration procedure is to measure a broad size distribution with various overlapping diameter ranges for each aperture and overlapping ranges with different apertures. The calibration is verified if the computed size distributions are in agreement in their regions of overlap. This agreement has been achieved with some difficulty.

Latex microspheres with narrow size distributions were used for calibration and their properties are summarized in Table B.4. The 40 μm particles were supplied dry and were dispersed in artificial seawater by sonication. The other microspheres were supplied as concentrated suspensions which were diluted with artificial seawater before counting.

Table B.4 Latex microsphere calibration particles.

Diameter (μm)	Composition	Standard Deviation Per Cent of Mean	Lot Number	Supplier
1.011	Polystyrene	0.5	2G4H	Dow Diagnostics
2.02	Polyvinyltoluene	0.7	1177	Duke Scientific
5.1	Polystyrene DVB	1.	3750	Duke Scientific
5.17	Polystyrene	2.	1177	Duke Scientific
10.12	Polystyrene	2.	1177	Duke Scientific
19.87	Polystyrene	1.4	1077	Duke Scientific
40.	Polystyrene DVB	10.	3769	Duke Scientific

There is some discussion in the literature on the accuracy of reported diameters for commercially available microspheres. Cassatt *et al.* (1976) used three different techniques (optical microscopy, electron microscopy, and laser diffraction) to measure the diameter of 2 μm spheres. The mean diameters obtained with the three methods were consistent but were two standard deviations away from the reported diameter of the sample. Duke Scientific, the source of all but one of the microspheres, will not estimate the accuracy of their reported diameters (Duke, personal communication, 1978). Duke Scientific sizes particles less than 1 μm by electron microscopy, and optical microscopy is used for particles greater than 20 μm. For the intermediate range of 1 to 20 μm, particle sizes are obtained with a Coulter Counter calibrated with particles less than 1 μm and greater than 20 μm. The Coulter Counter sizing technique has not been published. In this research the reported particle diameters have been used for calibration and satisfactory size distributions were obtained.

The first step in calibration is to determine the log base of the electronic system. Since the voltage pulse from the Coulter Counter is proportional to particle volume, $\Delta V_{in} \propto d_p^3$, and the MCA is linear in response to the output voltage pulse of the PSA, the following expression from Equation (B.1) relates particle diameter d_i to MCA channel i

$$i = \log_b d_i^3 + \text{constant} \quad . \tag{B.3}$$

There are two unknowns in this equation, the log base and the constant, With two monodisperse particle suspensions of diameters d_i and d_j appearing in channels i and j, there are two equations and two unknowns. Eliminating the constant and solving for the log base gives

$$b = \left(\frac{d_i}{d_j} \right)^{3/(i-j)} \quad . \tag{B.4}$$

Assigning a channel number to a given calibration particle requires judgment. For latex microspheres of diameters 1.011 and 2.02 μm, the size distributions are not monodisperse, but unimodal and have well defined maxima. For these particles the peak channel number is used for calibration. The larger calibration particles are either bimodal or have a broad distribution so that the mean channel number of the distribution is used to calculate the log base. Plots of the MCA counts for the calibration particles are shown in Figure B.1 for various apertures. All distributions have been normalized to contain 1000 counts.

The MCA output for 1.011 μm and 2.02 μm latex microspheres shown

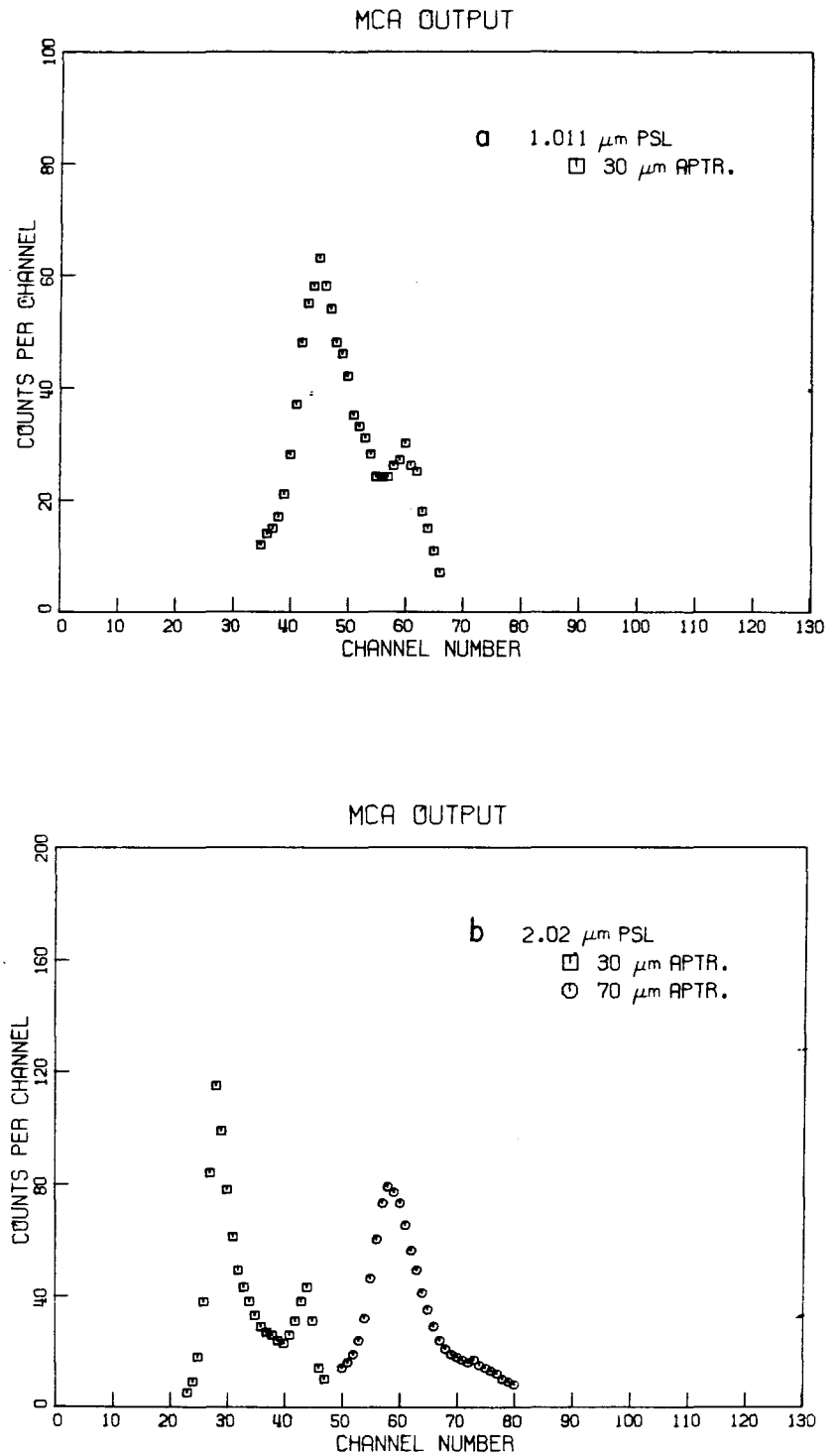

Figure B.1 Polystyrene latex microsphere normalized distributions observed with various apertures. a) 1.011 μm, b) 2.02 μm.

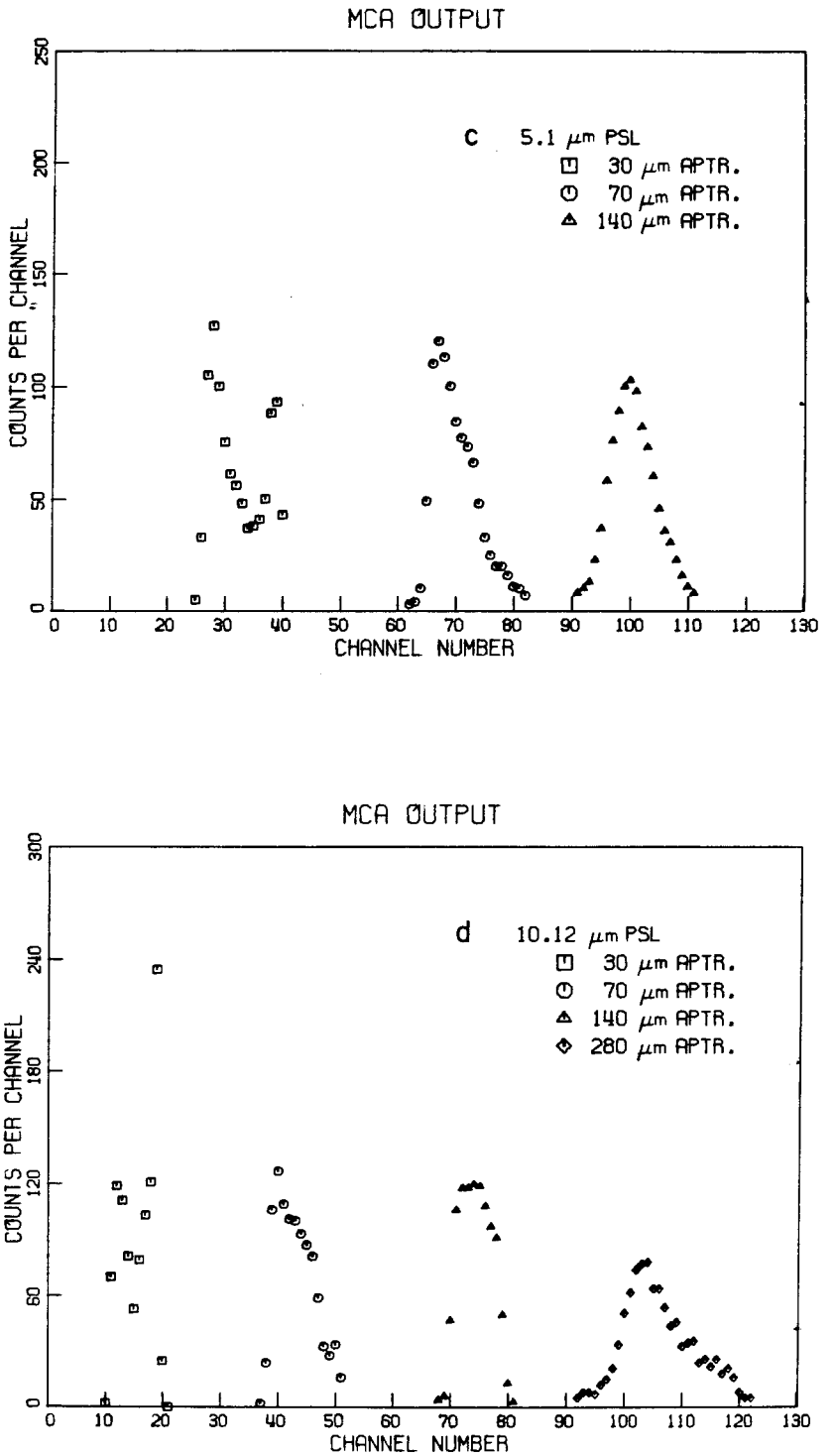

Figure B.1 Polystyrene latex microsphere normalized distributions observed with various apertures. c) 5.1 μm, d) 10.12 μm.

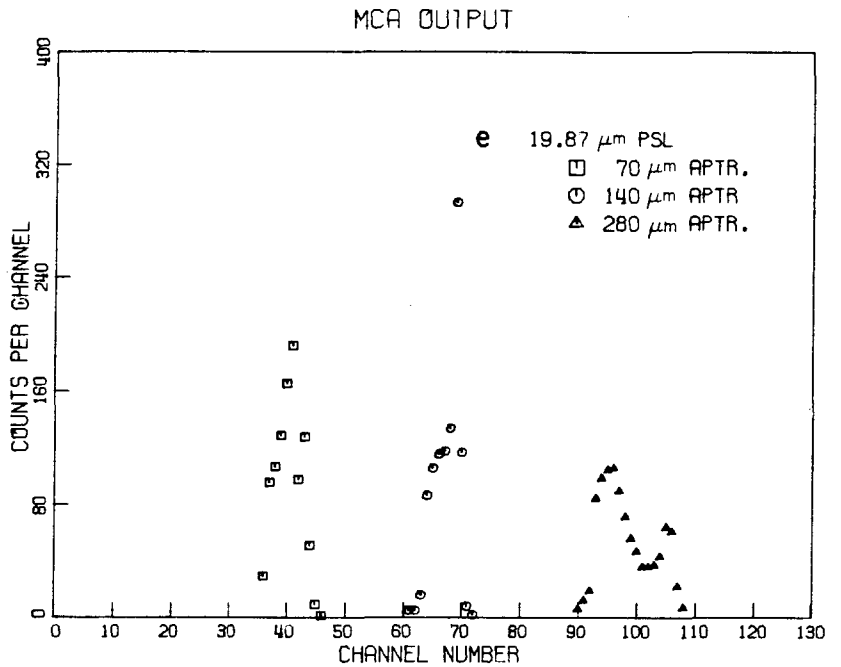

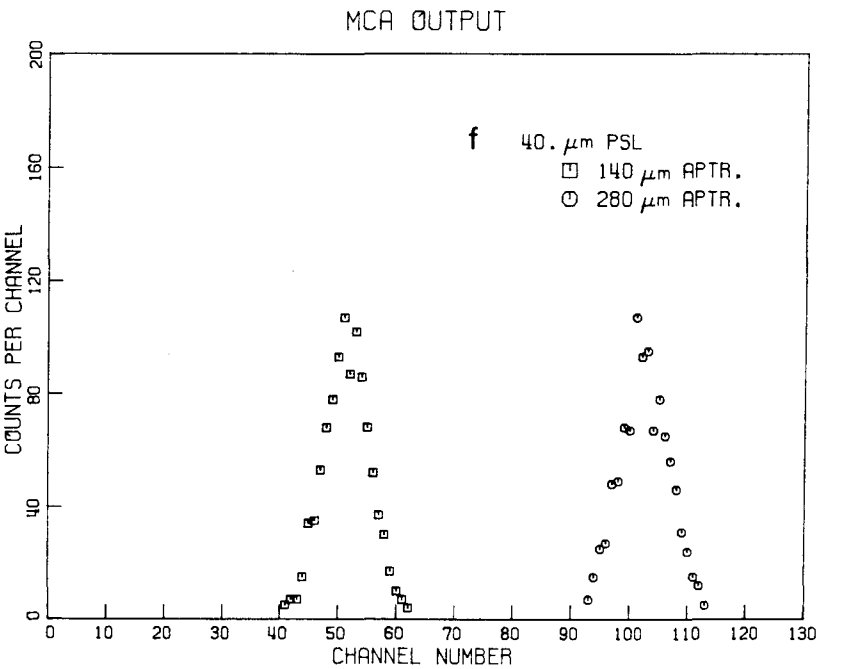

Figure B.1 Polystyrene latex microsphere normalized distributions observed with various apertures. e) 19.87 μm, f) 40. μm.

in Figures B.1a and B.1b have sharp peaks and evidence of dimers causing a skewness to the distribution. A particle of twice the singlet volume and a log base of 1.038 (see Table B.5) should appear 19 channels above the singlet peak, while the second peaks for 1.011 and 2.02 μm particles occur at 15 and 16 channels, respectively, above the maxima. For the 2.02 μm particles, a narrower distribution is obtained with the 30 μm aperture than the 70 μm aperture where the particle diameter is much smaller than the orifice diameter.

Figures B.1c through B.1f demonstrate similar features of a change in microsphere distribution with different apertures. The 5.1 μm particles measured with a 30 μm aperture have a bimodal distribution with the second peak eleven channels above the first, too close for a dimer. With the 70 μm aperture, the distribution becomes narrower, skewed, and unimodal, while the distribution obtained with the 140 μm aperture is broader, symmetrical, and unimodal. Results for 10.12, 19.87 and 40 μm particles show similar patterns of detailed distributions when the particle diameter is greater than five to ten per cent of the orifice diameter, and the distributions broaden as the particle diameters approach the lower limit of detection for the aperture.

Using the above procedure for assigning a diameter to a channel, log bases are calculated for various particle pairs as summarized in Table B.5. While there is considerable scatter in the log bases, the values obtained for each pair of particles for the different apertures are close, indicating possible inaccuracies in the reported mean diameters of the microspheres. The mean of the log bases was 1.038.

Table B.5 Log bases of ZBI-PSA-MCA system.

Particle Pair	Aperture			
	30	70	140	280
1.011-2.02	1.0392			
2.02-5.17	1.0367	1.0377		
5.17-10.12	1.0384	1.0388	1.0374	
10.12-19.87		1.0375	1.0375	1.0397
19.87-40.			1.0366	1.0365
mean log base = 1.0378		standard deviation = 0.0011		

The final step of calibration is to select settings of 1/CURRENT and 1/AMPLIFICATION and use a calibration particle to obtain a reference channel of known diameter. From Equation (B.3) for a known log base, a calibration particle of diameter d_c appearing in channel c allows evaluation of the constant in the equation and calculation of the diameter d_i in any channel i

$$d_i = d_c b^{(i-c)/3} \quad . \tag{B.5}$$

Calibration of the particle sizing system consists of two steps, first, calculation of the log base of the electronic system using pairs of latex microspheres, and second, use of a calibration particle to fix the diameter at one channel at the appropriate Coulter Counter settings. The calibration process results in knowledge of the particle diameter at each channel of the MCA, as represented in Equation (B.5).

B.4 Calculation of Particle Size Distributions

The modified Coulter Counter is used to rapidly obtain the number of particles in multiple size intervals. The purpose of this section is to present the mechanics of converting particle counts in the channels of the MCA into size distributions. The discussion includes calculation of size distributions, noise, and multiple aperture sizing techniques.

The particle size distribution, $n(d_p)$, is defined in the expression

$$n(d_p) = \frac{\Delta N}{\Delta d_p} \qquad [\#/mL - \mu m] \qquad (B.6)$$

where ΔN is the number of particles counted per milliliter of fluid in the narrow range of particle diameters from d_p to $d_p + \Delta d_p$. The particle size distribution can be used to obtain a number of important suspension properties. The total number of particles in suspension is given by integration of the particle size distribution

$$N = \int_0^\infty n(d_p)d(d_p) \qquad [\#/mL] \quad . \qquad (B.7)$$

Similarly, total area and total volume can be computed if the complete size distribution is available. Another distribution useful for data presentation is the differential volume distribution

$$\frac{dV}{d(\log d_p)} = \frac{\ell n\ 10}{6}\ \pi\ d_p^{\ 4} n(d_p) \qquad [\mu m^3/mL] \qquad (B.8)$$

which is the particle volume in a small logarithmic interval of particle size. Friedlander (1977) discusses the derivation of this distribution.

For each aperture and each series of Coulter Counter settings, 128 channels of data are included in the MCA output from which size distributions are obtained. The first eight channels are eliminated by the lower level discriminator (LLD). With the average log base of 1.038 indicated in Table B.5 the range in diameters from channel 9 to channel 128 is given by

$$\frac{d_{128}}{d_9} = b^{(128-9)/3} = 4.39 \qquad \text{(B.9)}$$

This is a small range and size distributions are not computed for each channel of MCA data. The diameter range between channels is only $(1.038)^{1/3} = 1.013$ which is greater resolution in size distributions than desired and such resolution is not achievable with the Coulter Counter. By grouping eight channels of MCA data to compute one point of the size distribution, a diameter range of 1.105 between points is obtained which is reasonable considering the spread observed in the microsphere distributions. In Equation (B.6) ΔN is the sum of the counts in the eight channels and Δd_p is the difference between the diameter of first channel of the next grouping of eight channels and the diameter of the first channel. The diameter for the size distribution is taken as the geometric mean of the eight diameters. For a group of eight channels starting at channel i with n_i counts, have

$$\Delta N = \sum_{j=i}^{i+7} n_j \qquad \text{(B.10)}$$

$$\Delta d_p = d_{i+8} - d_i \tag{B.11}$$

$$d_p = \left[\prod_{j=i}^{i+7} d_j \right]^{1/8} . \tag{B.12}$$

The accuracy of the calculated particle size distributions was checked by integrating the distribution over the range of diameters to obtain the total number of counts. Total counts obtained by integration never differed more than 0.1 per cent from the total counts recorded by the MCA indicating the choice of channel groupings did not distort the size distribution function.

Size distributions were not always obtained down to channel nine because some electronic noise was usually present at the lowest channels. Settings of 1/AMPLIFICATION and 1/CURRENT were chosen to measure the smallest particles possible, which meant including some electronic noise in the first few channels of the MCA. Blanks of filtered artificial seawater were counted to determine the magnitude of electronic noise signals and background particles. For size distribution calculations the beginning channel was chosen such that the particle counts were at least ten times greater than the counts in that channel of the blank solution. Because the electronic noise fell off very rapidly, the eight channels that compose the first point of the size distribution would have a noise component less than ten per cent.

With an effective diameter range of only 4.39, the measurement of broader distributions requires either multiple settings at one aperture or use of multiple apertures. Multiple apertures are usually preferred

because 1) flow rates through the smallest apertures are very slow and only suitable for counting the smallest particles, 2) the number of larger particles is usually low and larger volumes must be sampled which is not practical for the smaller apertures, 3) small apertures break up some aggregates at smaller diameters than larger apertures, and 4) because number concentration falls off rapidly with increasing diameter and flow rates through the orifices increase with increasing aperture size, coincidence corrections can be avoided when multiple apertures are used with only one dilution of the sample. Thus, there are a number of advantages in using multiple apertures in obtaining broad size distributions. In the next section examples of solid and aggregate sizing demonstrate the procedures discussed above and point out some difficulties.

B.5 Solid and Aggregate Sizing Examples

This section presents examples of size distributions obtained with the modified Coulter Counter. The solid suspension is composed of iron oxide crystals (γ-FeOOH) prepared by Sung (in preparation) and the aggregate suspensions are from the particle coagulation experiments. Examples of emulsion size distribution measurements using multiple apertures are included in Appendix A.

Volume distributions for the iron oxide suspension are shown in Figure B.2 with units of particle volume per gram of solid. The distribution has a very steep peak near 2 μm and only the 30 and 70 μm apertures were used for sizing. Two different settings for the 30 μm aperture gave very good agreement in the region of overlap. Data for the 70 μm aperture do not agree as well, being 30 per cent above the

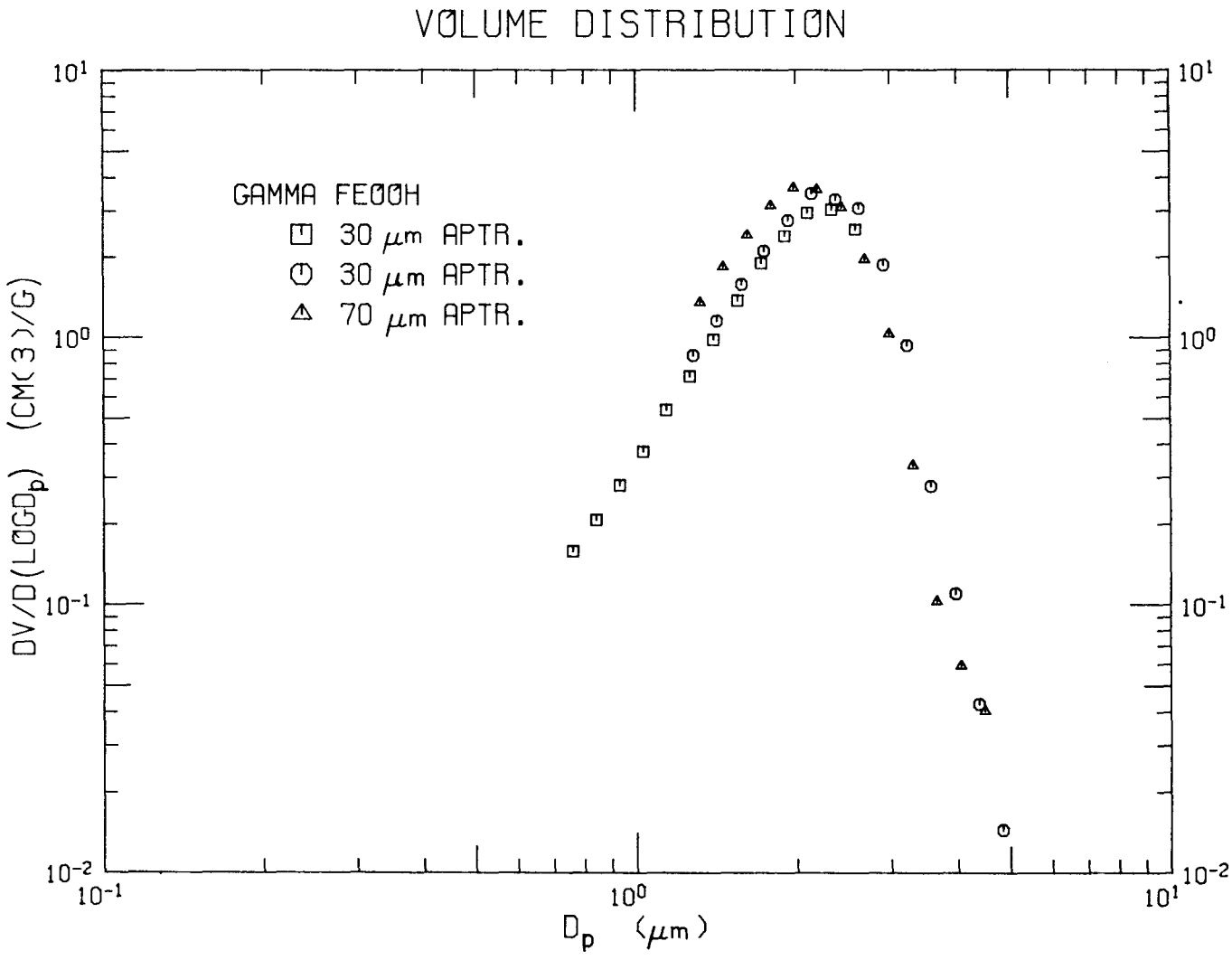

Figure B.2 Volume distribution of γ-FeOOH measured with 30 and 70 μm apertures.

volume distribution measured by the 30 μm aperture for diameters less than the peak.

Figure B.3 contains a plot of volume distributions for one sample from a kaolinite coagulation experiment at G = 4 sec^{-1} using 30, 70 and 140 μm apertures. The important feature in these distributions is the lack of agreement between apertures in regions of overlap. The reason for the misalignment is the breakup of larger aggregates in the high fluid shear near the orifice. The oscilloscope on the Model ZBI Coulter Counter displays signal pulses of particles passing through the orifice. When a large aggregate passes through the orifice, a burst of small signals is displayed on the oscilloscope indicating the aggregate has broken up before entering the sensing volume in the orifice. The burst of smaller signals are not all recorded by the MCA because the signals in the burst exceed the data collection rate of the MCA. So, for larger aggregates the counting system records only some of the aggregate volume as smaller particles. These aggregate pieces influence the measured size distributions in the regions where aggregates are not breaking up as indicated in Chapter 4.

Multiple aperture volume distributions obtained for illite at G = 1 and 8 sec^{-1} are shown in Figure B.4. At both shear rates there is no agreement between the different apertures and only the distributions measured with the 30 μm aperture below about one micrometer are considered representative of the actual aggregate distribution. There is no indication of an increase in aggregate strength with an increase in shear rate as encountered with montmorillonite and silica.

For the coagulating montmorillonite volume distributions shown in

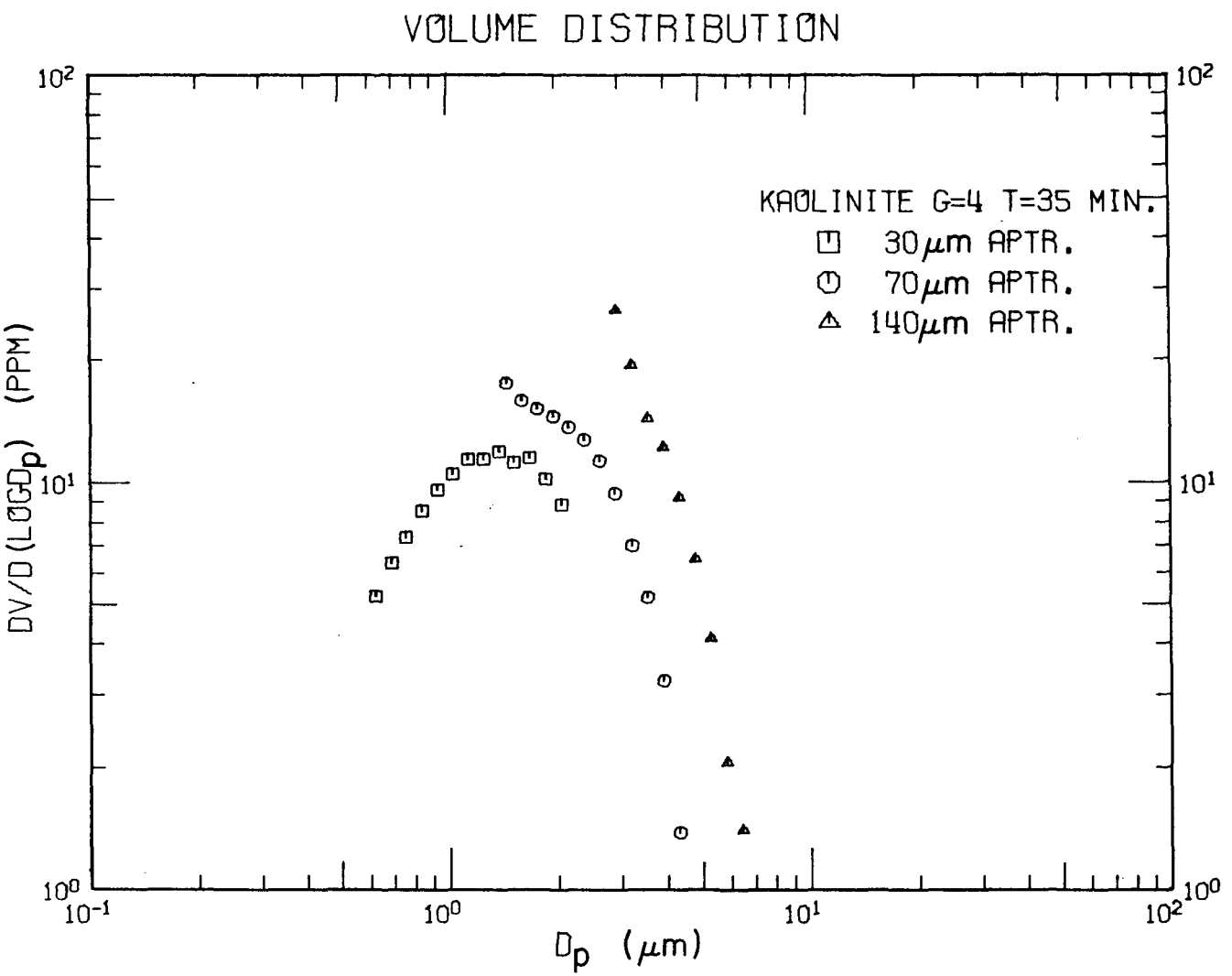

Figure B.3 Volume distribution of kaolinite in seawater 35 minutes after initial mixing observed by 30, 70, and 140 μm apertures.

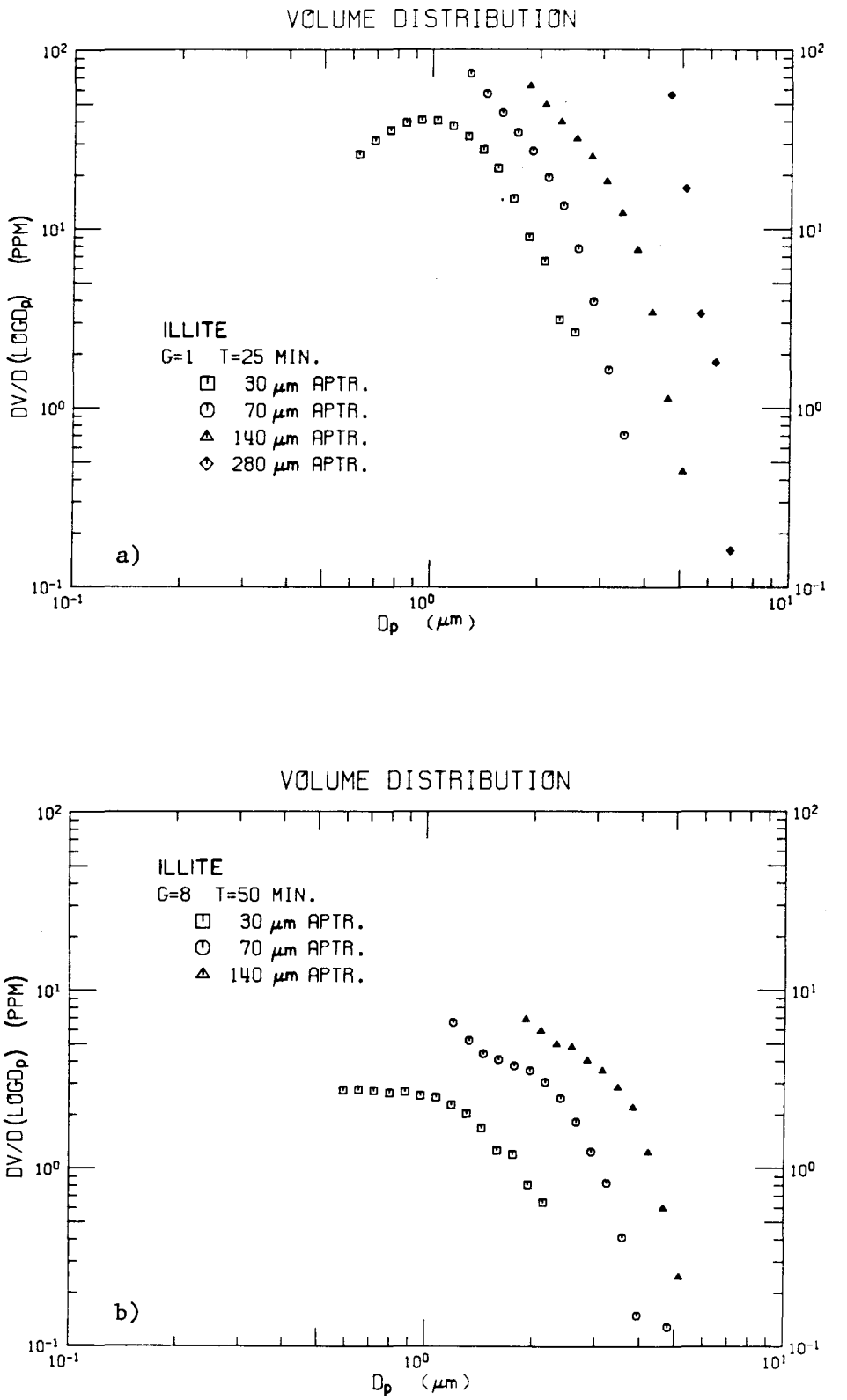

Figure B.4 Multiple aperture volume distributions for illite at a) $G = 1\ sec^{-1}$ and b) $G = 8\ sec^{-1}$.

Figure B.5 there is a noticeable difference between aperture alignment at $G = 1/2$ sec^{-1} and at $G = 16$ sec^{-1}. At $G = 1/2$ sec^{-1} only the 30 μm aperture data below about 1.3 μm measure the aggregate distribution while larger diameters and the other two apertures are strongly influenced by aggregate breakup during counting. The measured distributions at $G = 16$ sec^{-1} have regions of agreement between pairs of apertures and demonstrate the size dependence of breakup during counting with different apertures; small apertures breakup particles during counting at smaller aggregate diameters than larger apertures. The difference in alignment between low and high shear rates indicates there is an increase in aggregate strength with an increase in shear rate. This qualitative observation supports the explanation that higher shear rates in the montmorillonite experiments produced a distribution where shear-induced aggregate breakup in the rotating cylinder apparatus dominated the volume distribution rather than particle coagulation (see Section 4.5).

Multiple aperture volume distributions of silica at $G = 1$ and 16 sec^{-1} are shown in Figure B.6. At both shear rates there are intervals where the 30 and 70 μm aperture data overlap; a greater interval of alignment was achieved at the higher shear rate. No alignment occurred between the 70 and 140 μm apertures, although the data at $G = 16$ sec^{-1} show closer agreement than at the lower shear rate. Silica aggregate volume distributions, like montmorillonite, showed an increase in aggregate strength with an increase in shear rate due to a shear breakup dominated volume distributions.

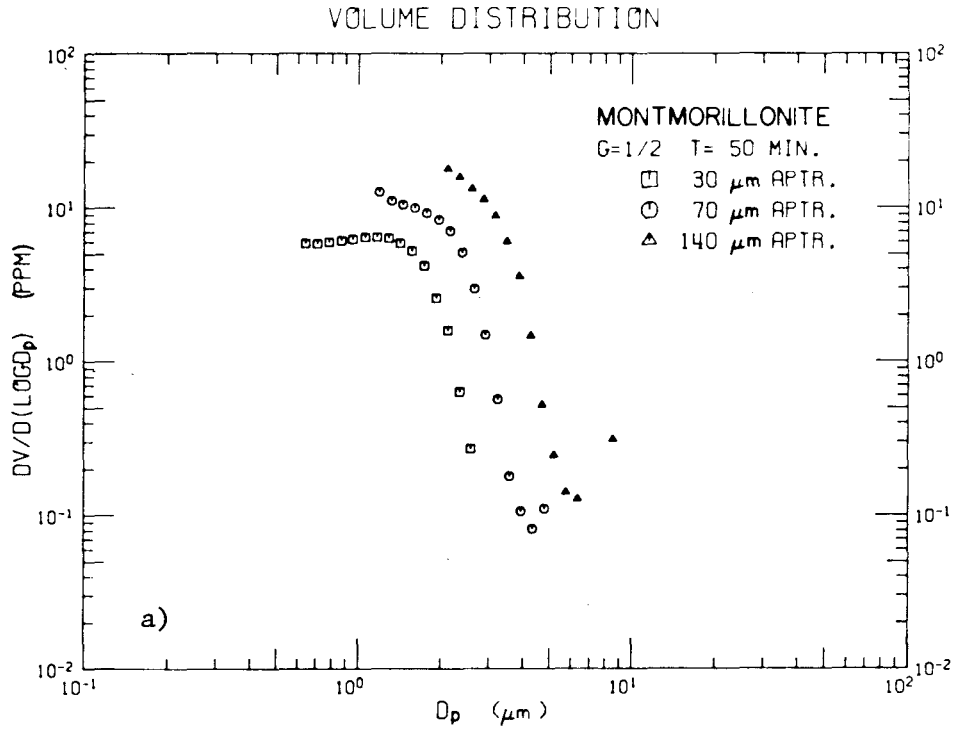

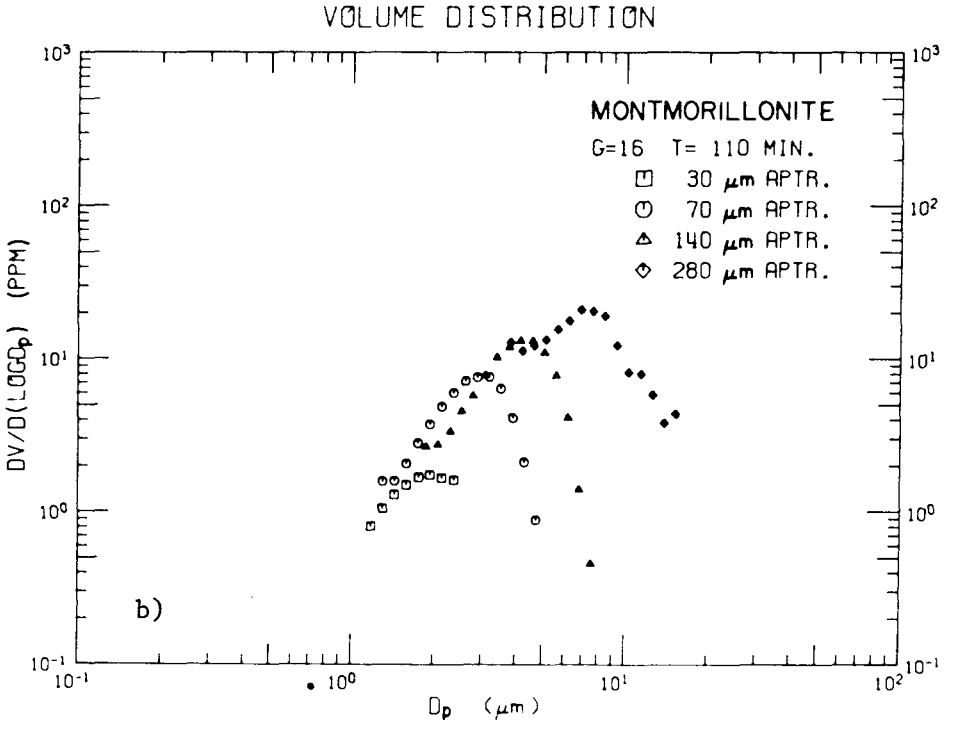

Figure B.5 Multiple aperture volume distributions for montmorillonite at a) $G = 1/2\ sec^{-1}$ and b) $G = 16\ sec^{-1}$.

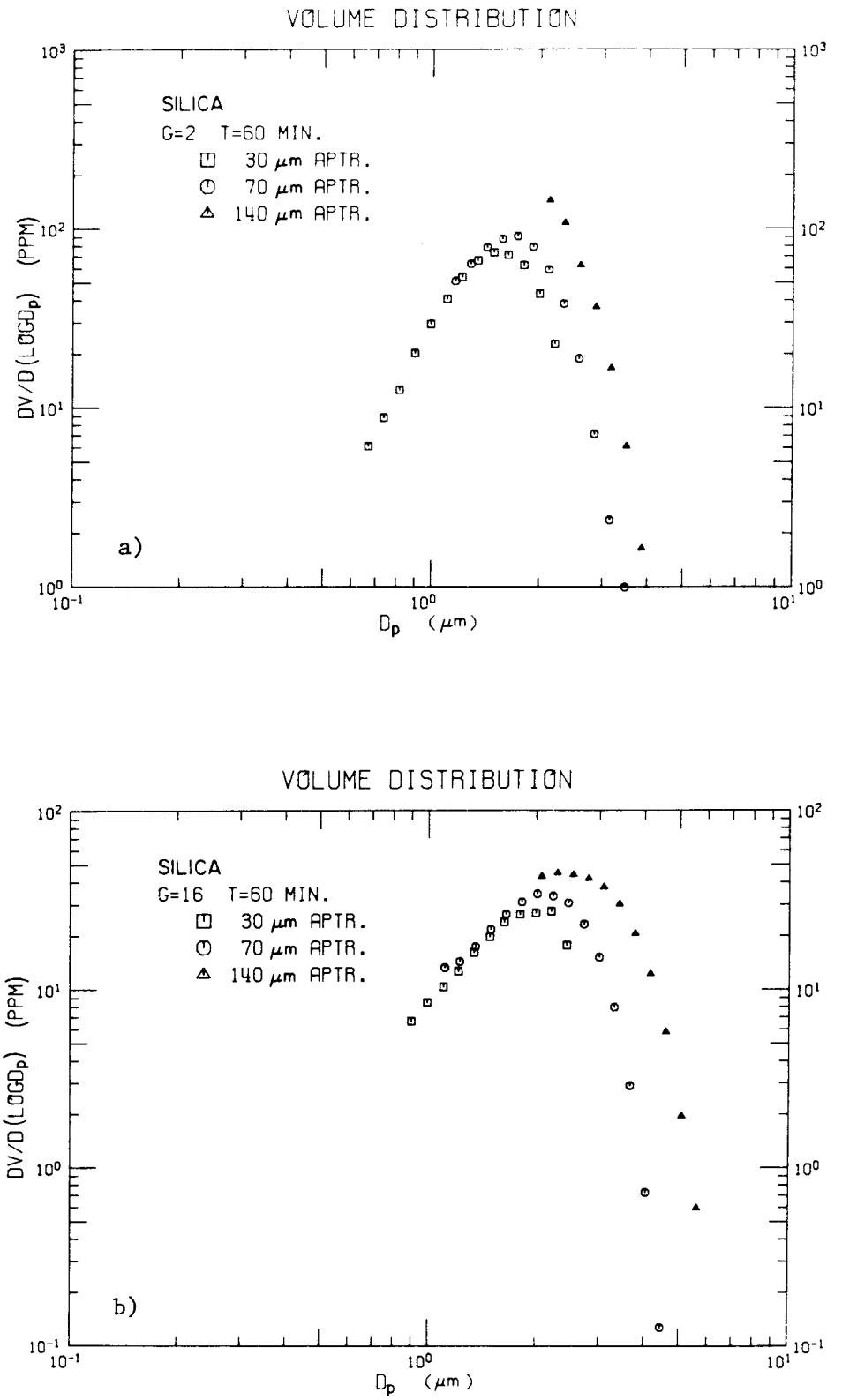

Figure B.6 Multiple aperture volume distributions for silica at a) $G = 2\ sec^{-1}$ and b) $G = 16\ sec^{-1}$.

B.6 Summary

Measurement of particle size distributions was a critical element in the verification of the theoretical predictions for particle coagulation. This appendix has reviewed the modified Coulter Counting technique used in this research and has presented the procedures developed for calibration and calculation of size distributions. Examples of measured volume distributions were included for solid and coagulating suspensions. Complete size distributions of coagulating suspensions were not obtained because of breakup of larger aggregates during counting.

APPENDIX C

FLUID FLOW IN THE ROTATING CYLINDER APPARATUS

This appendix discusses fluid flow in the gap between two concentric cylinders as used in the coagulation experiments. The local and mean shear rate, the distribution of shear rates in the gap, and fluid stability are briefly summarized.

van Duuren (1968) solved the Navier-Stokes equation for the tangential velocity in the gap for a fixed inner cylinder and a constant rotation of the outer cylinder. The local velocity gradient, G', was obtained as

$$G'(r) = \frac{N\pi}{15} \frac{R_1^2 R_2^2}{R_2^2 - R_1^2} \frac{1}{r^2} \qquad (C.1)$$

where R_1 is the radius of the inner cylinder, R_2 is the radius of the outer cylinder and N is the outer cylinder rotation rate in revolutions per minute. The mean shear rate over the annular gap is

$$G = \frac{1}{\pi(R_2^2 - R_1^2)} \int_{R_1}^{R_2} G'(r)\ 2\pi r dr \qquad (C.2)$$

which after integration using Equation (C.1) for G'(r) gives

$$G = \frac{2\pi N}{15} \frac{R_1^2 R_2^2}{(R_2^2 - R_1^2)^2} \ln\left(\frac{R_2}{R_1}\right) . \qquad (C.3)$$

In van Duuren's (1968) analysis, a linear average was taken over the gap which is only correct for a very small gap width, that is $(R_2 - R_1)/R_2 \ll 1$.

The maximum variation in shear is calculated as the difference between the maximum and the minimum shear rates normalized by the mean shear rate,

$$\frac{\Delta G}{G} = \frac{G'(R_1) - G'(R_2)}{G}$$

$$= \frac{1}{2} \frac{R_2^2 - R_1^2}{R_1^2 R_2^2} \frac{1}{\ell n(R_2/R_1)} \quad . \tag{C.4}$$

In the analysis of fluid stability between rotating cylinders, Taylor (1936) presented experimental results on transition of the flow from laminar to turbulence. While the outer cylinder radius used in Taylor's experiments was 4.05 cm compared with 4.42 cm in this work, an order of magnitude estimate of rotation speeds for onset of turbulence can be obtained. Using Taylor's Figure 8 which was for a gap distance of $(R_2 - R_1)/R_1 = 0.17$ as was used in experimental apparatus described in Chapter 3, the fluid became turbulent when the outer cylinder was rotating at approximately 380 revolutions per minute. Rotation rates used in the experiments were at most 48 revolutions per minute and should avoid turbulent flows. Strict similarity between Taylor's apparatus and the one used for coagulation experiments was not obtained and turbulence may occur sooner than Taylor's estimate because of surface roughness from the epoxy paint used in the present apparatus.

APPENDIX D

TOTAL SUSPENDED VOLUME OVER TIME FOR A COAGULATING AND SETTLING PARTICLE SIZE DISTRIBUTION

In this appendix the predicted particle size distributions for Brownian, shear, and differential sedimentation coagulation and gravitational settling are used to obtain expressions for the variation of total suspended volume with time.

Using Equation (3.3) for the volume flux through the distribution

$$E(t) = - \frac{dV(t)}{dt} \tag{D.1}$$

and noting that V(t) is given by

$$V(t) = \int_0^\infty \frac{\pi}{6} d_p^3 n(d_p,t)\ d(d_p) \tag{D.2}$$

a solution for V(t) is possible using predictions for the size distribution. This equation notes explicitly the time dependence of the size distribution. Predictions of particle size distributions are substituted into Equation (D.2) for Brownian, shear, and differential sedimentation coagulation. The limits of integration defining the region of dominance of each mechanism are obtained by assuming continuity between predictions and solving for the diameter which separates the regions of dominance. The predicted size distributions and regions of dominance are

Brownian
$$n(d_p,t) = A_b\left(\frac{E(t)}{K_b}\right)^{1/2} d_p^{-2.5}, \quad 0 < d_p \leq \left(\frac{K_b A_{sh}^2}{G A_b^2}\right)^{1/3} \tag{D.3}$$

shear
$$n(d_p,t) = A_{sh}\left(\frac{E(t)}{G}\right)^{1/2} d_p^{-4}, \quad \left(\frac{K_b A_{sh}^2}{G A_b^2}\right)^{1/3} < d_p \leq \frac{G A_{ds}^2}{K_{ds} A_{sh}^2} \tag{D.4}$$

differential sedimentation
$$n(d_p,t) = A_{ds}\left(\frac{E(t)}{K_{ds}}\right)^{1/2} d_p^{-4.5}, \quad \frac{G A_{ds}^2}{K_{ds} A_{sh}^2} < d_p < \infty \tag{D.5}$$

The assumption of a quasi-dynamic steady state size distribution makes only the volume flux a function of time. The fluid shear is assumed to be large enough for a shear-dominated subrange to exist, that is, $G > K_b^{1/4} K_{ds}^{3/4} A_{sh}^2 / A_b^{1/2} A_{ds}^{3/2}$.

Substituting Equations (D.3), (D.4), and (D.5) into Equation (D.2) gives

$$V(t) = \int_o^{\left(\frac{K_b A_{sh}^2}{G A_b^2}\right)^{1/3}} A_b \frac{\pi}{6}\left(\frac{E(t)}{K_b}\right)^{1/2} d_p^{1/2}\, d(d_p) + \int_{\left(\frac{K_b A_{sh}^2}{G A_b^2}\right)^{1/3}}^{\frac{G A_{ds}^2}{K_{ds} A_{sh}^2}} A_{sh} \frac{\pi}{6}\left(\frac{E(t)}{G}\right)^{1/2} d_p^{-1} d(d_p)$$

$$+ \int_{\frac{G A_{ds}^2}{K_{ds} A_{sh}^2}}^{\infty} A_{ds} \frac{\pi}{6}\left(\frac{E(t)}{K_{ds}}\right)^{1/2} d_p^{-3/2}\, d(d_p) \tag{D.6}$$

which becomes on evaluation of the three integrals

$$V(t) = \left(\frac{E(t)}{G}\right)^{1/2} \pi A_{sh} \left[\frac{4}{9} + \frac{1}{6} \ell n \frac{G^{4/3} A_b^{2/3} A_{ds}^2}{K_b^{1/3} K_{ds} A_{sh}^{8/3}}\right] \tag{D.7}$$

Defining a constant

$$\alpha = \pi A_{sh} \left[\frac{4}{9} + \frac{1}{6} \ell n \frac{G^{4/3} A_b^{2/3} A_{ds}^2}{K_b^{1/3} K_{ds} A_{sh}^{8/3}} \right] \tag{D.8}$$

and solving for E(t) in Equation (D.7), obtain

$$E(t) = \frac{GV^2(t)}{\alpha^2} \quad . \tag{D.9}$$

Substituting Equation (D.9) for E(t) into Equation (D.1) gives a differential equation in V(t)

$$\frac{dV(t)}{dt} = - \frac{G}{\alpha^2} V^2(t) \quad , \tag{D.10}$$

or the rate of change in suspended volume is second order in volume and linearly dependent on the shear rate. With an initial volume V_o, Equation (D.10) has the normalized solution

$$\frac{V(t)}{V_o} = \frac{1}{1 + \frac{GV_o}{\alpha^2} t} \quad . \tag{D.11}$$

Equation (D.11) indicates a characteristic half time for suspended particle volume removal by coagulation of α^2/GV_o, showing the dependence on the shear rate and initial volume. The dependence of α on G is through a logarithmic term and α is likely to be insensitive to changes in G. The parameter α is dependent upon particle and fluid properties through the coagulation parameters and dimensionless constants.

The derivation of Equation (D.11) assumed the volume distribution

was composed of regions dominated by Brownian, shear, and differential sedimentation coagulation and neglected gravitational settling. A similar result can be derived for a volume distribution dominated by Brownian and shear coagulation and settling, noting that the characteristic diameter separating shear coagulation and settling is $G^{2/3}S^{-1}E^{1/3}(A_s/A_{sh})^{3/4}$ and the analysis as above gives

$$V(t) = \left(\frac{E(t)}{G}\right)^{1/2} \pi A_{sh} \left[\frac{1}{3} + \frac{1}{6} \ell n \frac{G E^{1/3} A_b^{2/3} A_s^{1/3}}{S K_b^{1/3} A_{sh}^2}\right] \tag{D.12}$$

assuming that the $\ell n\ E^{1/3}$ term in the bracket has small variation over time, define a parameter, α', which is approximately constant over time

$$\alpha' = \pi A_{sh} \left[\frac{1}{3} + \frac{1}{6} \ell n \frac{G E^{1/3} A_b^{2/3} A_s^{4/3}}{S K_b^{1/3} A_{sh}^2}\right] . \tag{D.13}$$

Solution for the change in suspended volume with time follows as above noting the result is only an approximation

$$\frac{V(t)}{V_o} \simeq \frac{1}{1 + \frac{GV_o}{\alpha'^2} t} . \tag{D.14}$$

The coagulation and settling predicted size distributions are seen to allow calculation of total suspended volume over time. The grouping of $V_o Gt$ in the results of Equations (D.11) and (D.14) agrees with empirical results found by Camp and others in the analysis of coagulation and settling units in water and wastewater treatment operations.

O'Melia (1972) has suggested that $\eta V_o Gt$ be used for design of coagulation processes and for analysis of coagulation in natural aquatic environments. Here, η is the experimental collision efficiency for monodisperse particle suspensions which is dependent mainly on the particle stability. As particles become destabilized, η approaches one. The analysis is only qualitative since collision efficiency is not defined in a polydisperse suspension and a value of $\eta V_o Gt$ does not correspond to a given removal efficiency. Equations (D.11) and (D.14), on the other hand, are quantitative expressions for suspended volume over time for a polydisperse system. The dimensionless groups $V_o Gt/\alpha^2$ and $V_o Gt/\alpha'^2$ include α and α' which are determined from coagulation and sedimentation parameters and dimensionless constants. Thus, this analysis of coagulating and settling particle size distributions is able to arrive at expressions that incorporate a dimensionless grouping of terms which has been empirically observed to guide in the design and analysis of particle removal by coagulation.

APPENDIX E

DIMENSIONAL ANALYSIS USING A PARTICLE MASS UNIT

In Chapter 2 the dimensional analysis was based on a particle length unit (ℓ) and a fluid length unit (L). This appendix shows that a particle mass unit can be used instead of a particle length unit and the same predicted particle size distributions are obtained. This analysis avoids multiple length units in the dimensional analysis.

The particle size distribution as a function of particle mass is represented as n(m), which is the number of particles of mass between m and m+dm. The units of n(m) are $[L^{-3}M^{-1}]$ where [M] is a particle mass unit. The relationship between $n(d_p)$ and n(m) is

$$n(d_p) = n(m) \frac{dm}{d(d_p)}$$

$$= \rho_p \frac{\pi}{2} d_p^2 n(m) \quad . \tag{E.1}$$

Following the notation and procedures of Chapter 2, the sedimentation flux and the coagulation collision functions are expressed in terms of particle mass instead of particle diameter. From the sedimentation flux and the collision functions, new characteristic parameters are identified for use in the dimensional analysis. In Chapter 2 the steady state distribution was characterized in terms of the particle volume flux, E with units $[\ell^3 L^{-3} T^{-1}]$. For consideration of coagulation and sedimentation in terms of mass, the mass flux through the size distribution is represented by $\rho_p E$ with units $[ML^{-3}T^{-1}]$.

Transformation of Equation (2.2) for the sedimentation flux, noting $m = \frac{\pi}{6} \rho_p d_p^3$, gives

$$\text{sedimentation flux} = \left(\frac{6}{\pi}\right)^{2/3} \frac{g}{18\nu} \left(\frac{\rho_p - \rho_f}{\rho_f}\right) \rho_p^{-2/3} m^{2/3} n(m)dm \qquad (E.2)$$

The resulting characteristic parameter for gravitational settling and associated units are

$$S\rho_p^{-2/3} \equiv \frac{g}{\nu} \left(\frac{\rho_p - \rho_f}{\rho_f}\right) \rho_p^{-2/3} \qquad [LM^{-2/3}T^{-1}] \qquad (E.3)$$

using the previous definition of S.

For the three coagulation mechanisms, the collisions functions for particles of mass m_i and m_j are

Brownian
$$\beta_b(m_i,m_j) = \frac{2kT}{3\mu} \frac{(m_i^{1/3} + m_j^{1/3})^2}{m_i^{1/3} m_j^{1/3}} \qquad (E.4)$$

shear
$$\beta_{sh}(m_i,m_j) = \frac{G}{\pi\rho_p} (m_i^{1/3} + m_j^{1/3})^3 \qquad (E.5)$$

differential sedimentation
$$\beta_{ds}(m_i,m_j) = \left(\frac{6}{\pi}\right)^{4/3} \frac{\pi g}{72\nu} \left(\frac{\rho_p - \rho_f}{\rho_f}\right) \rho_p^{-4/3} \left(m_i^{1/3} + m_j^{1/3}\right)^2 \left| m_i^{2/3} - m_j^{2/3} \right| \qquad (E.6)$$

From these collision functions the following parameters and units are obtained:

Brownian $$K_b = \frac{kT}{\mu} \qquad [L^3T^{-1}] \qquad (E.7)$$

shear $$G\rho_p^{-1} \qquad [L^3M^{-1}T^{-1}] \qquad (E.8)$$

differential sedimentation $$K_{ds}\rho_p^{-4/3} = \frac{g}{\nu}\left(\frac{\rho_p-\rho_f}{\rho_f}\right)\rho_p^{-4/3} \qquad [L^3M^{-4/3}T^{-1}] \; . \qquad (E.9)$$

Consideration of particle mass gives different characteristic parameters for differential sedimentation coagulation and gravitational settling unlike the particle length analysis in Chapter 2.

With the conversion to particle mass units, the size distribution has the following functional form

$$n = n(m, \rho_p E, K_b, G\rho_p^{-1}, K_{ds}\rho_p^{-4/3}, S\rho_p^{-2/3}) \; . \qquad (E.10)$$

Selecting intervals of particle mass where only one coagulation mechanism or settling is dominant, the following particle size distributions are obtained dimensionally

Brownian $$n(m) = A_b'\left(\frac{\rho_p E}{K_b}\right)^{1/2} m^{-3/2} \qquad (E.11)$$

shear $$n(m) = A_{sh}'\left(\frac{\rho_p E}{G\rho_p^{-1}}\right)^{1/2} m^{-2} \qquad (E.12)$$

differential sedimentation

$$n(m) = A'_{ds}\left(\frac{\rho_p E}{K_{ds}\rho_p^{-4/3}}\right)^{1/2} m^{-13/6} \qquad \text{(E.13)}$$

settling

$$n(m) = A'_{s}\left(\frac{\rho_p E}{S\rho_p^{-2/3}}\right)^{3/4} m^{-9/4} \qquad \text{(E.14)}$$

where A'_b, A'_{sh}, A'_{ds}, and A'_s are dimensionless constants different from those appearing in Chapter 2. When these predictions of n(m) are transformed into $n(d_p)$ using Equation (E.1) the size distributions are in agreement with those obtained in Chapter 2.

This appendix has shown that the dimensional analysis in Chapter 2, based on fluid and particle length units, can be reproduced when a fluid length unit and a particle mass unit are used.

REFERENCES

Argaman, Y., and W. J. Kaufman. 1968. Turbulence in Orthokinetic Flocculation. Sanitary Engineering Research Laboratory, College of Engineering and School of Public Health, University of California, Berkeley, SERL Report No. 68-5, Berkeley, California.

Bernstein, D. F., W. I. Higuchi, and N.F.H. Ho. 1971. Kinetics of flocculation and/or coalescence of dilute oil-in-water emulsions. J. Pharm. Sci. 60(5), 690-694.

Birkner, F. B., and J. J. Morgan. 1968. Polymer flocculation kinetics of dilute colloidal suspensions. J. Amer. Water Works Assoc. 60(2), 175-191.

Bradley, R. A., and R. B. Krone. 1971. Shearing effects on settling of activated sludge. ASCE J. Sanit. Engr. Div. 97(SA1), 59-79.

Brooks, N. H. 1956. Report to Hyperion Engineers on Predictions of Sedimentation and Dilution of Digested Sludge in Santa Monica Bay. August 7, 1956, 18 pp. Pasadena, California.

Carrol, B. J. 1976. The stability of emulsions and mechanisms of emulsion breakdown. E. Matijević, editor, Surface and Colloid Science 9, 1-67.

Cassatt, W. A., Y. T. Yap, W. P. Reed, and S. A. Mills. 1976. Results of measurements on fine particle Standard Reference Materials at NBS. Powder Technol. 13, 27-31.

Chang, D.P.Y. 1973. Particle Collection from Aqueous Suspensions by Solid Hollow Single Fibers. Ph.D. thesis, California Institute of Technology, Pasadena, California.

Drake, D. E. 1976. Suspended sediment transport and mud deposition on continental shelves. D. J. Stanley and D.J.P. Swift, editors, Marine Sediment Transport and Environmental Management. Wiley, New York. pp. 127-158.

Edzwald, J. K., and C. R. O'Melia. 1975. Clay distributions in recent estuarine sediments. Clays Clay Minerals 23, 39-44.

Edzwald, J. K., J. B. Upchurch, and C. R. O'Melia. 1974. Coagulation in estuaries. Environ. Sci. Technol. 8(1), 58-63.

Eppler, B., U. Neis, and H. H. Hahn. 1975. Engineering aspects of the coagulation of colloidal particles in natural waters. Prog. Water Technol. 7(2), 207-216.

Fair, G. M., and R. S. Gemmell. 1964. A mathematical model of coagulation. J. Colloid Sci. 19, 360-372.

Faisst, W. K. 1976. Digested Sewage Sludge: Characterization of a Residual and Modeling for Its Disposal in the Ocean off Southern California. Ph.D. thesis, California Institute of Technology, available as Environmental Quality Laboratory Report No. 13. Pasadena, California.

Friedlander, S. K. 1960a. On the particle-size spectrum of atmospheric aerosols. J. Meteorol. 17, 373-374.

Friedlander, S. K. 1960b. Similarity considerations for the particle-size spectrum of a coagulating, sedimenting aerosol. J. Meteorol. 17, 479-483.

Friedlander, S. K. 1977. Smoke, Dust and Haze: Fundamentals of Aerosol Behavior. Wiley-Interscience, New York.

Galloway, J. N. 1972. Man's Alteration of the Natural Geochemical Cycle of Selected Trace Metals. Ph.D. thesis, University of California, San Diego. San Diego, California.

Galloway, J. N. 1979. Alteration of trace metal geochemical cycles due to the marine discharge of wastewater. Geochim. Cosmochim. Acta 43, 207-218.

Gardner, W. D. 1977. Fluxes, Dynamics, and Chemistry of Particulates in the Ocean. Ph.D. thesis, Massachusetts Institute of Technology and Woods Hole Oceanographic Institution. Cambridge, Massachusetts.

Gelbard, F. 1979. The General Dynamic Equation for Aerosols. Ph.D. thesis, California Institute of Technology. Pasadena, California.

Greene, C. S. 1976. Changes in the grain size of sediments on the Palos Verdes shelf. Southern California Coastal Water Research Project, Annual Report. El Segundo, California. pp. 91-93.

Gross, M. G., editor. 1976. Middle Atlantic Continental Shelf and the New York Bight. Amer. Limnol. Oceanog. Spec. Symp. 2. Lawrence, Kansas.

Hahn, H. H., and W. Stumm. 1968. Kinetics of coagulation with hydrolyzed Aℓ(III), the rate determining step. J. Colloid Intf. Sci. 28(1), 134-144.

Harris, H. S., W. J. Kaufman, and R. B. Krone. 1966. Orthokinetic flocculation in water purification. ASCE J. Sanit. Engr. Div. 92(SA6), 95-111.

Hendricks, T. J. and D. R. Young. 1974. Modeling the Fates of Metals in Ocean Discharged Wastewaters. Southern California Coastal Water Research Project, Technical Report 208. El Segundo, California.

Hidy, G. M. 1965. On the theory of the coagulation of noninteracting particles. J. Colloid Sci. 20, 123-145.

Honig, E. P., G. J. Roebersen, and P. H. Wiersema. 1971. Effect of hydrodynamic interaction on the coagulation rate of hydrophobic colloids. J. Colloid Intf. Sci. 36, 97-109.

Honjo, S. 1978. Sedimentation of materials in the Sargasso Sea at a 5,367 m deep station. J. Marine Res. 36(3), 469-492.

Hunt, J. R. In press. Prediction of oceanic particle size distributions from coagulation and sedimentation mechanisms. M. C. Kavanaugh and J. O. Leckie, editors, Particulates in Water: Characterization, Fate, Effects, and Removal. A.C.S. Advances in Chemistry Series.

Ives, K. J., and A. G. Bhole. 1973. Theory of flocculation for continuous flow system. ASCE J. Env. Engr. Div. 99(EE1), 17-34.

Kasper, D. R. 1971. Theoretical and experimental investigations on the flocculation of charged particles in aqueous solutions by polyelectrolytes of opposite charge. Ph.D. thesis, California Institute of Technology. Pasadena, California.

Kerr, P. F., *et al.* 1949-50. Reference Clay Minerals; American Petroleum Institute Research Project 49, Preliminary Reports No. 1-8. Columbia University, New York.

Krone, R. B. 1963. A Study of Rheological Properties of Estuarial Sediments. Tech. Bull. 7, Comm. on Tidal Hydraulics, U.S. Army Corps of Engineers.

Krone, R. B. 1972. A Field Study of Flocculation as a Factor in Estuarial Shoaling Processes. Tech. Bull. 19, Comm. on Tidal Hydraulics, U.S. Army Corps of Engineers.

Krone, R. B. 1976. Engineering interest in the benthic boundary layer. I. N. McCave, editor, The Benthic Boundary Layer. Plenum, New York. pp. 143-156.

Lawler, D. F., C. R. O'Melia, and J. E. Tobiason. In press. Integral water treatment plant design: from particle size to plant performance. M. C. Kavanaugh and J. O. Lackie, editors, Particulates in Water: Characterization, Fate, Effects and Removal. A.C.S. Advances in Chemistry Series.

Lichtenbelt, J.W.Th., C. Pathmamanoharan, and P. H. Wiersema. 1974. Rapid coagulation of polystyrene latex in a stopped-flow spectrophotometer. J. Colloid Intf. Sci. 49, 281-285.

Manley, R. St.J., and S. G. Mason. 1955. Particle motions in sheared suspensions III. Further observations on collisions of spheres. Can. J. Chem. 33, 763-773.

Marmur, A. 1979. A kinetic theory approach to primary and secondary minimum coagulations and their combination. J. Colloid Intf. Sci. 72(1), 41-48.

Mason, B. J. 1971. Physics of Clouds. Second edition, Clarendon Press, Oxford.

McIntyre, A. D., *et al.* 1976. Working group reports-F metabolism at the benthic boundary. I. N. McCave, editor, The Benthic Boundary Layer. Plenum, New York. pp. 297-310.

Mitchell, F. K. 1976. Sediment trap applications in the nearshore region (sewage sludge discharge). Rep. Calif. Coop. Ocean. Fish. Invest. 18, 159-161.

Morel, F.M.M., J. C. Westall, C. R. O'Melia, and J. J. Morgan. 1975. Fate of trace metals in Los Angeles County wastewater discharge. Environ. Sci. Technol. 9, 756-761.

Myers, E. P. 1974. The Concentration and Isotopic Composition of Carbon in Marine Sediments. Ph.D. thesis, California Institute of Technology. Pasadena, California.

O'Melia, C. R. 1972. Coagulation and flocculation. W. J. Weber, editor, Physicochemical Processes for Water Quality Control. Wiley-Interscience, New York. pp. 61-109.

O'Melia, C. R., and W. Stumm. 1967. Aggregation of silica dispersions by iron (III). J. Colloid Intf. Sci. 23, 437-447.

Overbeek, J.Th.G. 1977. Recent developments in understanding of colloid stability. J. Colloid Intf. Sci. 58(2), 408-422.

Pavlou, S. P., and R. N. Dexter. 1979. Distribution of polychlorinated biphenyls (PCB) in estuarine ecosystems. Testing the concept of equilibrium partitioning in the marine environment. Environ. Sci. Technol. 13(1), 65-71.

Peterson, L. L. 1974. The Propagation of Sunlight and the Size Distribution of Suspended Particles in a Municipally Polluted Ocean Water. Ph.D. thesis, California Institute of Technology. Pasadena, California.

Prieve, D. C., and E. Ruckenstein. 1980. Role of surface chemistry in primary and secondary coagulation and heterocoagulation. J. Colloid Intf. Sci. 73(2), 539-555.

Riley, J. P., and G. Skirrow. 1965. Chemical Oceanography. Academic Press, New York. Vol. 1.

Saffman, P. G., and J. S. Turner. 1956. On the collision of drops in turbulent clouds. J. Fluid Mech. 1, 16-30.

Sholkovitz, E. R. 1978. The flocculation of dissolved Fe, Mn, Aℓ, Cu, Ni, Co, and Cd during estuarine mixing. Earth Planet. Sci. Lett. 41, 77-86.

Southern California Coastal Water Research Project. 1978. Coastal Water Research Project Annual Report for the Year 1978. El Segundo, California.

Spielman, L. A. 1970. Viscous interactions in Brownian coagulation. J. Colloid Intf. Sci. 33(4), 562-571.

Spielman, L. A., and S. L. Goren. 1972. Theory of coalescence by flow through porous media. Ind. Engr. Chem. Fund. 11(1), 66-72.

Sung, W. In preparation. The effect of the γFeOOH(lepidocrocite) surface on the oxygenation kinetics of aqueous manganous manganese and ferrous iron. Ph.D. thesis, California Institute of Technology. Pasadena, California.

Sweeney, R. E., E. K. Kalil, and I. R. Kaplan. In press. Characterization of domestic and industrial sewage in southern California coastal sediments using nitrogen, carbon, sulfur, and uranium tracers. Marine Environ. Res.

Swift, D. L., and S. K. Friedlander. 1964. The coagulation of hydrosols by Brownian motion and laminar shear flow. J. Colloid Sci. 19, 621-647.

Taylor, G. I. 1936. Fluid friction between rotating cylinders. Part I. Torque measurements. Proc. Royal Soc. A 157, 546-564.

Treweek, G. P. 1975. The Flocculation of E. Coli with Polyethyleneimine. Ph.D. thesis, California Institute of Technology. Pasadena, California.

Treweek, G. P., and J. J. Morgan. 1977. Size distributions of flocculated particles: application of electronic particle counters. Environ. Sci. Technol. 11(7), 707-714.

Turekian, K. K. 1977. The fate of metals in the oceans. Geochim. Cosmochim. Acta 41, 1139-1144.

van de Ven, T.G.M., and S. G. Mason. 1977. The microrheology of colloidal dispersions VII. Orthokinetic doublet formation of spheres. Colloid Polym. Sci. 255, 468-479.

van Duuren, F. A. 1968. Defined velocity gradient model flocculator. ASCE J. Sanit. Engr. Div. 94(SA4), 671-682.

van Olphen, H. 1977. An Introduction to Clay Colloid Chemistry. Second edition. Wiley-Interscience, New York.

Vuceta, J. 1976. Adsorption of Pb(II) and Cu(II) on α-Quartz from Aqueous Solutions: Influence of pH, Ionic Strength, and Complexing Ligands. Ph.D. thesis, California Institute of Technology. Pasadena, California.

Wang, C. S., and S. K. Friedlander. 1967. The self-preserving particle size distribution for coagulation by Brownian motion II. Small particle slip correction and simultaneous shear flow. J. Colloid Intf. Sci. 24, 170-179.

Wasan, D. T., S. M. Shah, N. Aderangi, M. S. Chan, and J. J. McNamara. 1978. Observations on the coalescence behavior of oil droplets and emulsion stability in enhanced oil-recovery. Soc. Petrol. Engr. J. 18(6), 409-417.

Whitehouse, V. G., L. M. Jeffery, and J. D. Debrecht. 1960. Differential settling tendencies of clay minerals in saline waters. Proc. 7th Nat. Conf. Clays Clay Minerals. pp. 1-79.

Zeichner, G. R., and W. R. Schowalter. 1977. Use of trajectory analysis to study stability of colloidal dispersions in flow fields. AIChE 23(3), 243-254.